

# **Empirical Membrane Lifetime Model for Heavy Duty Fuel Cell Systems**

**by**

**Natalia Macauley**

M.Sc., University of Iceland, 2011

Dissertation Submitted in Partial Fulfillment of the  
Requirements for the Degree of  
Doctor of Philosophy

in the

School of Mechatronic Systems Engineering  
Faculty of Applied Sciences

**© Natalia Macauley 2015**

**SIMON FRASER UNIVERSITY**

**Summer 2015**

All rights reserved.

However, in accordance with the *Copyright Act of Canada*, this work may be reproduced, without authorization, under the conditions for "Fair Dealing." Therefore, limited reproduction of this work for the purposes of private study, research, criticism, review and news reporting is likely to be in accordance with the law, particularly if cited appropriately.

Commercial Confidential

# Approval

**Name:** Natalia Macauley  
**Degree:** Doctor of Philosophy  
**Title:** *Empirical Membrane Lifetime Model for Heavy Duty Fuel Cell Systems*  
**Examining Committee:** Chair: Flavio Firmani  
Lecturer

**Erik Kjeang**  
Senior Supervisor  
Assistant Professor

---

**Gary Wang**  
Supervisor  
Professor

---

**Jake Devaal**  
Supervisor  
Industry Partner

---

**Farid Golnaraghi**  
Internal Examiner  
Professor

---

**Brant Peppley**  
External Examiner  
Professor  
Department of Chemical Engineering  
Queen's University

---

**Date Defended/Approved:** July 17, 2015

## Abstract

Heavy duty fuel cells used in transportation system applications such as transit buses expose the fuel cell membranes to conditions that can lead to lifetime-limiting membrane failure via combined chemical and mechanical degradation. Highly durable membranes and reliable predictive models are therefore needed in order to achieve the heavy duty fuel cell lifetime target of 18,000 h. In the present work, an empirical membrane lifetime model was developed based on laboratory data from a suite of accelerated membrane durability tests. The model considers the effects of cell voltage, temperature, oxygen concentration, humidity cycling, humidity level, and platinum in the membrane using inverse power law and exponential relationships within the framework of a general log-linear Weibull life-stress statistical distribution. The obtained model is capable of extrapolating the membrane lifetime from accelerated test conditions to use level conditions during field operation. Based on typical conditions for the Whistler, British Columbia fuel cell transit bus fleet, the model predicts a stack lifetime of 17,500 h and a membrane leak initiation time of 10,500 h. Validation performed with the aid of a field operated stack confirmed the initial goal of the model to predict membrane lifetime within 20% of the actual operating time.

**Keywords:** polymer electrolyte fuel cell; membrane durability; accelerated durability test; empirical model; lifetime prediction; degradation

## **Dedication**

I would like to dedicate this to my mother, Jana Macauley, who has always encouraged me to do my best in life.

## **Acknowledgements**

I would like to express my deepest appreciation to my supervisor and mentor, Prof. Erik Kjeang, who I highly honour and respect. His enthusiasm, encouragement and faith in me constantly inspired me to always approach all problems with a positive attitude and never give up. Without his guidance and persistent help this dissertation would not have been possible. I would also like to express my sincere gratitude to my co-supervisor and committee member, Gary Wang, who has been an example to look up to, and helped me through difficult periods in my life. I am also deeply indebted to Jake Devaal, principal safety engineer at Ballard Power Systems, and part of my committee. Jake has been very supportive of my work from the start and continues to provide valuable insight on the underlying reasons behind issues we tackle.

I would also like to thank Shanna Knights, Director of Research at Ballard Power Systems for making it possible for me to experience the fuel cell industry from the inside. Due to her welcoming and sincere interest in my research, I was able to greatly improve my hands on skills. I would also like to thank Mark Watson and Mike Lauritzen, both scientists to whom I look up to and have great respect for. Their insight and contributions were of utmost importance during my time at Ballard. I would also like to thank Joanna Kolodziej and Erin Rodgers for their ongoing support with failure analysis, and for sharing a lot of their expertise. I am also very grateful for the high level technical support I received from Brian Breiddal and Ron Mott at Ballard.

I would also like to express my gratitude to all my Co-op students for all of their hard work, namely Mark Cruickshank, Curtis Allen, Elizabeth Durward, Temir Baimukhametov and Ileana Co.

I would like to acknowledge Li Yang and Xin Zhang for their kind training and help at 4D Labs where all the TEM testing was done.

Finally, I would like to express my most cordial thanks for the funding of my project, which was generously provided by the Natural Sciences and Engineering Research Council of Canada for the Automotive Partnership Canada (APC) grant.

# Table of Contents

Approval.....	ii
Abstract.....	iii
Dedication.....	iv
Acknowledgements.....	v
Table of Contents.....	vi
List of Tables.....	viii
List of Figures.....	ix
List of Acronyms.....	x
<b>Chapter 1. Introduction .....</b>	<b>1</b>
<b>Chapter 2. Theory .....</b>	<b>9</b>
2.1. Membrane degradation.....	9
2.2. Accelerated membrane durability test (AMDT).....	13
2.3. Experimental design and empirical modeling.....	15
<b>Chapter 3. Experimental.....</b>	<b>16</b>
3.1. Membrane electrode assembly (MEA) fabrication.....	16
3.2. Stack assembly and test station .....	16
3.3. Baseline AMDT protocol.....	17
3.4. Complementary AMDT protocols.....	18
3.5. Characterization methods.....	19
<b>Chapter 4. Model description.....</b>	<b>22</b>
4.1. Stack level prediction.....	22
4.2. MEA level prediction.....	24
4.3. Prediction of bus lifetime with CeO <sub>2</sub> .....	31
4.4. H <sub>2</sub> /N <sub>2</sub> method for in-situ MEA leak testing.....	31
<b>Chapter 5. Results and validation of methodology .....</b>	<b>34</b>
5.1. Stack level approach .....	38
5.2. Membrane lifetime with CeO <sub>2</sub> .....	39
5.3. MEA level approach .....	43
5.4. Empirical model validation .....	46

<b>Chapter 6. Conclusions.....</b>	<b>51</b>
<b>References .....</b>	<b>53</b>
<b>Appendix A.....</b>	<b>64</b>
<b>Appendix B.....</b>	<b>68</b>
<b>Appendix C.....</b>	<b>79</b>
<b>Appendix D.....</b>	<b>109</b>

## List of Tables

Table 1. AMDT series designed for stack based empirical model.....	34
Table 2. Field operated membrane (FOM) and AMDT samples for TEM.....	36
Table 3. Experimental design for voltage and temperature.....	37
Table 4. Additional experiments at 21% O <sub>2</sub> . ....	37
Table 5. Stack based Whistler bus predicted initiation and failure time.....	39
Table 6. Results of stack level membrane lifetime predictions.....	43
Table 7. Parameters of GLL – Weibull distribution.....	44
Table 8. Empirical stack model results for stacks A and B.....	49

## List of Figures

Figure 1. Individual fuel cell. ....	2
Figure 2. Nafion Fluoropolymer. ....	4
Figure 3. Flowchart of stack based empirical model. ....	23
Figure 4. Decay trends of voltage and temperature at 0.9V, 45% O <sub>2</sub> , RH cycling. ....	38
Figure 5. Leak rate development in time of CeO <sub>2</sub> membrane. ....	40
Figure 6. Additive washout with driving cycle (red) and voltage hold (blue) AMDT. ....	41
Figure 7. Exponential fit of acceleration factor decay. ....	42
Figure 8. Unreliability vs. initiation and failure time. ....	45
Figure 9. Probability density function plot of initiation and failure time. ....	45
Figure 10. Cell voltages in Stack B during H <sub>2</sub> /N <sub>2</sub> test at 0.3 barg and 30 °C. ....	47
Figure 11. Comparison of predicted vs. measured leak rate of extracted MEAs. ....	48

## List of Acronyms

ADT	Accelerated Durability Test
AMDT	Accelerated Membrane Durability Test
AST	Accelerated Stress Test
APC	Automotive Partnership Canada
BOL	Beginning-of-life
CCM	Catalyst Coated Membrane
CL	Catalyst Layer
EDS	Energy-dispersive X-ray Spectroscopy
EOL	End-of-life
GDE	Gas Diffusion Electrode
GDL	Gas Diffusion Layer
HOR	Hydrogen Oxidation Reaction
MEA	Membrane Electrode Assembly
MPL	Micro-Porous Layer
NAA	Neutron Activation Analysis
NMR	Nuclear Magnetic Resonance Spectroscopy
OCV	Open Circuit Voltage
ORR	Oxygen Reduction Reaction
PEM	Polymer Electrolyte Membrane
PFSA	Perfluoro Sulfonic Acid
RH	Relative Humidity
SEM	Scanning Electron Microscopy
TEM	Transmission Electron Microscopy
STEM	Scanning Transmission Electron Microscopy
HRTEM	High Resolution Transmission Electron Microscopy

## Chapter 1. Introduction

Fuel cells are electrochemical devices that convert chemical energy in fuels into electrical energy directly, providing power generation with high efficiency and low environmental impact [1]. In a fuel cell system unit cells are stacked up next to each other creating an electrically connected stack according to the desired output capacity. The feed stream conditioning, thermal management, and electric power conditioning of the stack is provided by components that belong to the balance of plant.

The main components of a fuel cell unit are an anode (negative electrode), cathode (positive electrode) and the electrolyte. Additional components are necessary for assembly of a fuel cell stack such as bipolar plates, flow fields and balance of plant components such as blowers and compressors for fuel supply and product removal, water and temperature management devices, converters, etc. Fuel is fed to the anode, and oxidant is fed to the cathode continuously at the same time. Hydrogen oxidation and oxygen reduction are the electrochemical reactions necessary for splitting the fuel and oxidant into ions and electrons. These reactions take place at electrode triple phase boundaries, which are catalytically active regions where the electrode particles, electrolyte phase, and gas pores intersect [2]. Highly porous electrode surfaces allow efficient diffusion of reactant gases to catalyst sites, and product removal from the fuel cell. Fuel cells are classified according to their electrolyte and fuel. The electrolyte also determines the electrode reactions and the type of ions that pass through the electrolyte. The electrolyte is thin in order to avoid losses caused by ion diffusion due to electrolyte material resistance. The electrolyte also acts as a physical barrier to prevent mixing of fuel and oxidant gas streams [1]. Some common types of fuel cells are the polymer electrolyte fuel cell (PEMFC), solid oxide fuel cell (SOFC), alkaline fuel cell (AFC), phosphoric acid fuel cell (PAFC), and molten carbonate fuel cell (MCFC) [1],[3]. SOFCs offer fuel flexibility, since they are capable of fuel reforming conventional hydrocarbon

fuels directly in the anode, due to their high operating temperature (500 – 1,000 °C). However, shutting down SOFC systems can cause large losses, because of the time and energy used to heat up the system. They are therefore best suited for applications with no transient requirements such as combined heat and power for homes or industry, where it is possible to make use of both heat and electricity. On the other hand proton exchange membrane fuel cells offer high power densities at relatively low operating temperatures (55–95 °C). In contrast to SOFCs, PEMFC show great promise in the transportation industry, where their low temperature operating temperature allows fast start-up. PEMFCs are also highly viable for portable applications, such as laptop batteries. Some challenges of PEMs are thermal and water management issues, such as clogging of the cathode. PEMFCs are also very sensitive to CO, Sulfur and Halogen poisoning, meaning they need high grade hydrogen, which is expensive. In order to make fuel cell vehicles competitive on the transportation market, current barriers such as the high cost of carbon electrodes with platinum electro-catalyst need to be overcome. Furthermore, fuel cell system performance and durability also need to be enhanced, to match the requirements [4]. Lastly, the lack of a hydrogen infrastructure is slowing down commercialization of PEMFCs. The basic concept of a PEMFC is shown in Figure 1 [1].

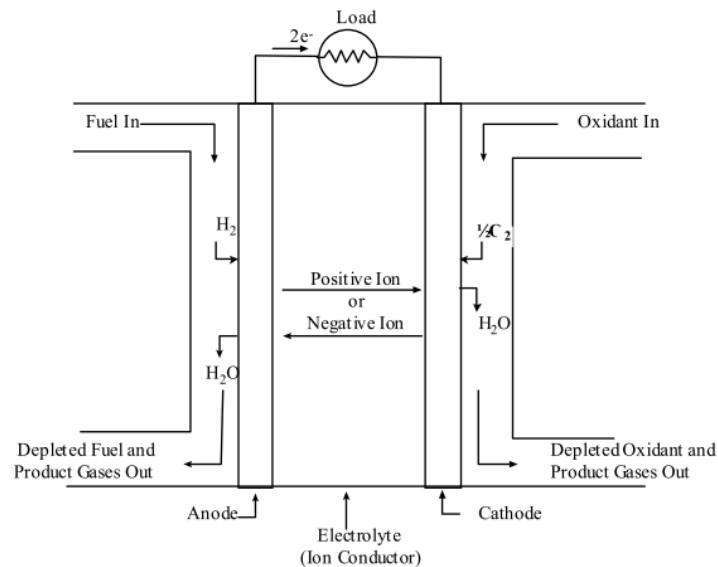


Figure 1. Individual fuel cell.

PEM fuel cells require a catalyst for the hydrogen oxidation reaction at the anode and the oxygen reduction reaction of oxygen at the cathode. The oxidation of pure hydrogen is not considered a technical hurdle, but the “oxygen reduction reaction” has slow kinetics [3]. The activation energy of a reaction is the energy needed for the reaction to take place. For reactions to take place in a PEMFC, the reactants need to overcome the activation energy of the reaction, in order to form the final products. A catalyst is defined as a substance that increases the rate of a chemical reaction by lowering the activation energy of the reaction, increasing the rate of a reaction. During a catalyzed chemical reaction, the structure and composition of catalysts does not change. Catalysts are not able to bring any changes to the nature of final product. Usually, a catalyst can be easily recovered after the reaction and reused for other reactions. The catalyst surface area needs be as high as possible because catalysis is a surface effect. The hydrogen oxidation reaction (HOR) strips the electrons off of hydrogen, generating hydrogen protons.



Hydrogen protons pass to the cathode through the electrolyte, while the electrons from the HOR pass through an external circuit where they supply electric power to a load before reaching the cathode. The result of the reaction is water formed at the cathode by the oxygen reduction reaction (ORR), by adding hydrogen electrons and protons to oxygen.



The overall reaction of hydrogen and oxygen to form water is



Platinum has been considered to be the best catalyst for both the anode and cathode although there is a significant difference between the ORR and HOR. Therefore, in many PEMFCs, the anode and the cathode use an identical catalyst:

carbon supported platinum nanoparticles, despite the fact that the use of precious metal catalysts (Pt and its alloys) makes the cost of PEM fuel cells high. The carbon-support used for platinum or platinum alloys lower component cost. The back of the electrodes is made hydrophobic by coating with an appropriate compound, such as Teflon®. This wet proof coating provides a path for gas diffusion to the catalyst layer.

The polymer electrolyte membrane is sandwiched between the two platinum electrodes. The main function of the membrane in PEM fuel cells is to transport protons from the anode to the cathode, while providing resistance to gas crossover and electrons. In a PEMFC, the electrolyte is made of a solid polymer electrolyte membrane such as Nafion, invented and patented by DuPont (Figure 2) [5]. Nafion is a polymer based on polytetrafluoroethylene (PTFE). The proton conductivity of Nafion is strongly dependent on the water content of the membrane. The membrane needs to be properly hydrated in order to effectively promote dissociation of ionic groups and provide a mechanism for proton transport. Water in the membrane is localized to the hydrophilic groups, where the protons dissociate and are transported in a vehicular manner by diffusion of hydrated protons [6] and also structurally via proton transfer between hydrated clusters [7].

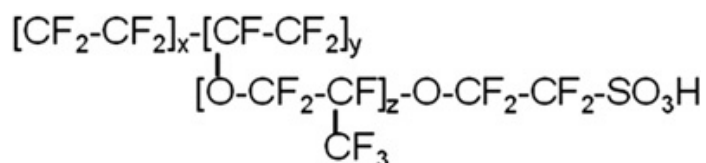


Figure 2. Nafion Fluoropolymer.

Carbon paper has good gas diffusion properties thanks to its porous structure and is therefore often used as a gas diffusion layer in fuel cell electrodes, where it serves both as mechanical and functional support. Gas Diffusion Layers (GDLs) are designed together with the flow fields and current collectors in order to achieve high

performance of the PEMFC. The main function of the GDL is to diffuse the gas. GDL material facilitates the effective diffusion of each reactant gas to the catalyst thanks to its porous nature [8]. The GDL is also an electrical connection between the carbon-supported catalyst and the bipolar plate or other current collectors, so it should have good electric conductive properties. Additionally, the GDL also helps to direct water away from the electrolyte surface and out of the fuel cell. An ideal GDL is required to effectively transport the gas reactants to the catalyst layers, have low electronic resistance, have a surface that enhances good electronic contact, and have proper hydrophobicity. Bipolar plates supply reactant gases to the gas diffusion electrodes (GDEs) via flow channels, provide electrical connections between individual cells, and effectively remove water produced at the cathode. Bipolar plates must also be relatively impermeable to gases, sufficiently strong to withstand stack assembly, and easily mass-produced. For transport applications, low weight and low volume are essential, plus the ability to accommodate high temperatures, high humidity, and an electrical potential [9].

Fuel cell hybrid vehicles offer improved fuel economy, zero emissions, and quiet operation compared to internal combustion and diesel motors. There is therefore growing interest in integration of fuel cell cars and buses in urban transit. Heavy and light duty durability targets of 18,000 and 5,000 h, respectively [4], [10], [11]. These targets are yet to be demonstrated in field operation, which makes the development of highly durable fuel cell components important. The main fuel cell stack producers are Ballard Power Systems, UTC Power, Hydrogenics, Proton Motor [12]. Fuel cell buses have been deployed in Whistler Canada, San Francisco USA, Hamburg Germany, Shanghai China, London England, São Paulo Brazil as well as several other places. Whistler buses, which use Ballard FCvelocity®-HD6 stacks successfully operated in the field for over 9,000 h. To date, one of UTC fuel cell system modules in Thousand Palms, CA has surpassed 12,000 hours of operation in revenue service, and continues to perform at rated power, with two other systems approaching this same durability milestone [13]. By showing long term stability and durability, these buses pave the way for future hydrogen and fuel cell bus deployment programs [14]. Apart from demonstration and concept cars by numerous producers, two limited commercial fuel cell car releases are already available by Hyundai ix35 FCEV (2013) and Toyota Mirai (2014) [15], [16]. Buses are

constantly operated for up to 24 hours a day every day, and therefore have much higher reliability and durability requirements compared to cars, which are yet to be met with existing FC technology. Finding solutions for fuel cell catalyst and membrane durability will play a major role in closing the gap between the current and the target fuel cells lifetime. Thus, more research and development is needed. However, testing fuel cell systems for transportation requires several thousand hours, which is not economically feasible. Instead, accelerated stress tests (ASTs) and accelerated durability tests (ADTs) are used to determine fuel cell system durability. The goal of ASTs and ADTs is to rapidly degrade a fuel cell membrane, yet induce failure modes observed in the field in a much shorter period of time. ASTs are generally used as a screening method to eliminate low performers in early stages. Good performers are then subjected to an ADT, for further evaluation. ADTs are designed to run with conditions, which are more representative of real conditions. ASTs and ADTs for fuel cells can be performed ex-situ or in a single cell/stack configuration. ADTs operate in steady state or dynamic mode [17]. Dynamic ADTs include the use of cycling potential, load, temperature, RH, start/stop cycling or apply a duty cycle that is an approximation of a realistic bus/car driving cycle [18]–[22]. Accelerated stress and durability tests are generally of qualitative character only. Quantitative analysis is done via empirical models, which estimate the lifetime at use conditions by using the appropriate degradation functions and statistical distributions. The lifetime of a fuel cell component generally decreases with increasing stressor levels. The lifetime decay rate however varies based on the stressor. Experimental design deals with the stressor choice and stressor levels to be tested, and is a crucial part of empirical modeling, as it dictates the quality of the results. Once the decay rates are known, an empirical lifetime prediction model can be used to predict lifetime by extrapolation from accelerated to use conditions.

Early life failure of the membrane is due to perforations, cracks, tears, or pinholes. Pinhole formation is the primary failure mode of fuel cell membranes that leads to catastrophic membrane failure. Furthermore, unrestricted hydrogen crossover through a pinhole poses a significant safety risk, and reduces fuel efficiency. Membrane degradation occurs mainly due to chemical, mechanical and thermal degradation. High voltages close to open circuit voltage (OCV) lead to increased chemical membrane

degradation due to enhanced gas crossover, subsequent radical formation and radical attack on the membrane [23]–[25]. Mechanical stress is a result of the membrane's response to humidity and temperature changes in a constrained fuel cell environment, which can eventually lead to polymer fatigue and creep [26], [27]. When pure chemical degradation was compared to coupled chemical and mechanical degradation in-situ, the lifetime of membranes exposed to coupled degradation was always 2 to 3.5 times shorter than those exposed to chemical degradation only [28]–[30]. Thus, coupled chemical and mechanical stress is more degrading to the membrane than pure chemical or mechanical stress. Both stressors are present during fuel cell operation, which is why such tests have successfully generated historical bus failure modes [31]. Voltage cycling causes fuel cell catalyst layer degradation, due to Pt dissolution and corrosion of carbon support during fuel cell operation [32], [33]. Chemical reduction of dissolved Pt ions by H<sub>2</sub> permeating through the membrane from the anode leads to Pt particle deposition in the membrane, and formation of a densely packed Pt band at a specific distance from the cathode [34]. In regards to the chemical stability of the membrane, both positive [35]–[38] and negative [39]–[46] effects of platinum in the membrane (PITM) have been reported. It is important to consider and include the effect of PITM when predicting fuel cell membrane lifetime. Many lifetime prediction models use a 10% fuel cell performance loss as a quantitative parameter [47], [48]. Voltage loss is primarily linked to failure modes of the catalyst, but can also be an indicator of pinhole formation, since H<sub>2</sub> presence at the cathode reduces the voltage due to its equilibrium voltage of 0 V. A Weibull-Arrhenius failure distribution was used to fit a current decay trend and predict the lifetime of a direct methanol fuel cell, previously subjected to a series of start/stop protocols at multiple temperature levels [49], [50]. Linear regression was used to fit impedance spectra during static and dynamic load ageing tests, in order to estimate fuel cell lifetime [25]. These models were only able to predict lifetime within their own experimental range of 1,000 – 1,500 h, which are very short lifetimes compared to those expected from fuel cell vehicles. Although, fuel cell membrane lifetime validation from the field is difficult to obtain, empirical models should be close or exceed the already known lifetime of operating membranes, since they have not failed yet. In other fuel cell applications, the lifetime of a stationary PEM fuel cell membrane at three temperature

levels at various RH levels [26] was fit to a Weibull – Arrhenius life stress combination based on fluoride release, RH and temperature in order to predict lifetime. Cyclic mechanical stress has also been used as a primary stressor in a fuel cell for lifetime prediction [53]. The results show an exponential decrease of membrane lifetime based on an increasing RH cycling amplitude. A fuzzy logic fuel cell diagnostic model used mechanical, chemical, and electrochemical FC subsystems to determine fuel cell system reliability [54]. As seen in the literature, various approaches can be used for lifetime prediction modeling of individual fuel cell components, entire systems in various fuel cell applications. A good fuel cell lifetime prediction model should be capable of predicting lifetime within 20% of the real lifetime, and be scalable to fit multiple applications.

The objective of this work is to design a series of accelerated membrane durability test (AMDT) protocols, and develop an empirical model for bus membrane lifetime prediction. Thus far, there has been no report on a systematic empirical lifetime prediction model for heavy duty fuel cell membranes, that includes the effect of Pt in the membrane, and has been validated by field operated fuel cell buses. In the proposed empirical model the investigated failure mode is a leak through the membrane, and membrane lifetime is the empirical model parameter. The first portion of the work deals with AMDT protocol design with regard to the main stressors, and stressor levels. The second part deals with the method of membrane lifetime extrapolation from AMDT conditions to use level conditions in the empirical model. The last section investigates the use of chemical additives for mitigation of membrane degradation under AMDT conditions, and how to include the lifetime results in the empirical lifetime model. Finally, model validation is done via observation of early membrane failures in the field. The empirical model will be used to find out if the tested membrane fulfills the internal bus membrane lifetime target of 20,000 h. This work means to serve as a benchmark for polymer electrolyte membrane fuel cell (PEMFC) durability testing, and lifetime prediction. The approach used in the empirical model is interchangeable, and can be adjusted to meet the needs of other fuel cell components and applications.

## Chapter 2. Theory

### 2.1. Membrane degradation

The main fuel cell membrane degradation mechanisms are thermal, chemical and mechanical degradation. Thermal membrane degradation is due to decomposition of side sulfonic acid groups on Nafion at high temperature; membrane blistering from the heat of reactions of crossover gases in a leaky membrane, or membrane deformation due to ice formation at subfreezing temperatures [55]. Chemical degradation is caused by radical attack of the membrane, seen as global and local membrane thinning. The dominant radical formation pathway is hydrogen peroxide decomposition in the presence of Fenton reagents such as  $\text{Fe}^{2+}$  [3], [56]. Hydrogen peroxide forms during the oxygen reduction reaction ORR at the cathode and from crossover oxygen that meets hydrogen at the anode [57]–[59].

Electrochemical formation of hydrogen peroxide ( $\text{H}_2\text{O}_2$ ) via the two-electron ORR in the catalyst layers [60] is as follows:

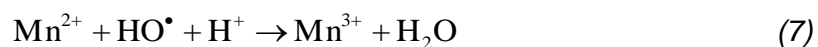


$\text{H}_2\text{O}_2$  formed at the electrodes can diffuse into the membrane and decompose into  $\text{OH}^\bullet$  via the Fenton's reaction mechanism in the presence of ferrous iron,  $\text{Fe}^{2+}$ :



Direct formation of hydroxyl radicals also occurs on Pt surfaces, without peroxide intermediates [61]. The hydroxyl ( $\text{HO}^\bullet$ ), hydroperoxyl ( $\text{HOO}^\bullet$ ), and hydrogen ( $\text{H}^\bullet$ ) radicals have been identified as potentially harmful to the membrane [62]. Radicals can form in

the catalyst layers or as a result of hydrogen peroxide decomposition in the presence of Fenton's reagents in the membrane [63]–[67]. Hydrogen peroxide forms electrochemically as a by-product of the oxygen reduction reaction (ORR), but also chemically when crossover oxygen and hydrogen meet at the cathode or anode [68]–[70]. Cell voltages close to open circuit voltage (OCV) are known to lead to high levels of chemical degradation, due to enhanced gas crossover, [23] resulting in a gradual loss of membrane material, observed as general membrane thinning and fluoride release in the effluent water [17]. The recently proposed iron redox cycle in the membrane, which has been shown to control the harmful  $\text{Fe}^{2+}$  concentration in the membrane through reaction-transport phenomena of mobile and redox active iron ions, elucidated the fundamental mechanism of increased chemical membrane degradation at high voltages [71]. Polymer side chain degradation in chemically stabilized PFSA membranes is predominantly due to  $\text{HO}^\bullet$  radical attack on the first ether bond in the  $\alpha\text{-OCF}_2\text{-}$  group [72]. Attack by  $\text{H}^\bullet$  may occur to a smaller extent at the tertiary carbon C–F bond on both the main and side chains, while attack by  $\text{HO}^\bullet$  occurs solely on the side chain, specifically at the  $\alpha\text{-O-C}$  bond [73]. Adequate humidification of the membrane is crucial for membrane durability, since fuel cell operation at dry conditions leads to increased  $\text{H}_2\text{O}_2$  formation, and thus increased membrane degradation. Membrane humidity levels influence reactant partial pressures, membrane permeability, and membrane thickness [74]–[76]. Operating a dry membrane at elevated temperatures leads to faster chemical degradation due to increased anode  $\text{H}_2\text{O}_2$  production, and subsequent radical formation [24], [68], [77], [78]. Chemical stabilization of PFSA polymer end groups [79] and use of additives, such as cerium and manganese radical scavengers are proven mitigation methods for chemical degradation [80], [81]. The main reactions for effective hydroxyl radical scavenging using Ce and Mn as additives are:



Chemical membrane degradation has a strong impact on mechanical membrane properties. Patil et al. [82] degraded Nafion® membrane samples under OCV conditions and observed a decline in fracture stress and strain of degraded samples, due to molecular weight reduction caused by chemical degradation.

Mechanical stress is a result of the membrane's response to humidity and temperature changes in a constrained fuel cell environment. A constrained membrane experiences in-plane compression upon swelling at high RH and in-plane tension upon shrinkage at low RH. The resulting mechanical stress from frequent swelling and shrinking of the membrane in response to changes in water content results in membrane creep, fatigue, [83], [84] and the formation of pinholes, cracks, and tears on the surface or in the bulk of the membrane [85]. Membrane stiffness and strength was found to decrease when exposed to humidity cycling at high temperatures [84], [86]. Different water sorption and desorption rates of the membrane and catalyst can create cracks and tears on the surface or in the bulk of the membrane [87]. Hot pressing, clamping, and bolting all cause mechanical stress experienced by the membrane. Non-uniform distribution of stresses caused by a temperature gradient in the fuel cell induces localized bending stresses, contributing to delamination between the membrane and the gas diffusion layers [88]. A dynamic mechanical analyser (DMA) can simulate mechanical membrane degradation by performing stress-strain tests [27], [89] and humidity/temperature cycling [90]. Mechanical endurance of membranes can be enhanced by physical reinforcement of the membrane using a porous polymer matrix, fibers, or inorganic reinforcement [91]. Membrane ductility decreased more significantly when exposed to chemical degradation than with mechanical degradation [92].

Coupled chemical and mechanical stressors exacerbate membrane degradation more than chemical and mechanical degradation applied separately. The impact of combined chemical and mechanical degradation on membrane durability was investigated under Ballard Power Systems' cyclic open circuit voltage (COCV) AST protocol [93]. The COCV AST consists of a steady state OCV phase and periodic wet/dry cycles. The membranes failed after 160 h, with a 48% reduction in membrane thickness, in good agreement with a 48% cumulative fluoride release. Pinholes as wide

as ~100  $\mu\text{m}$  were identified in the membrane. Results of mechanical testing showed a rapid reduction in CCM ductility and fracture strain together with a significant decrease in ultimate tensile strength (UTS) as a function of AST cycles [94]. The combination of chemical and mechanical stress was confirmed to be more degrading to the membrane than their separate application [57]. Membrane fracture, cracks, rips, tears and pinholes form faster in chemically degraded areas. On the other hand RH cycling accelerates chemical degradation via increased hydrogen peroxide formation during the dry phase and its subsequent spreading throughout the membrane during the wet phase. Coupled chemical and mechanical stress is commonly used for automotive FC membrane testing, as it is capable of generating historical bus failure modes, such as local membrane thinning, divot formation, delamination from the catalyst, crack and pinhole formation.

The fuel cell can experience voltages spikes at the cathode during start-ups and shut-downs, leading to dissolution and migration of platinum from the catalyst into the membrane [51]. At voltages above 0.9 V, a platinum oxide film (PtO) forms on the catalyst surface. As the voltage cycles below 0.9 V, removal of the PtO surface causes instability of Pt-Pt bonds in the first and second atomic layers of the catalyst, exposing them to dissolution [96]. High potentials during fuel cell start-up and shut-down also lead to corrosion of catalyst carbon support material, especially close to MEA outlets and at high temperatures [97], [98]. Carbon in the cathode catalyst layer is electrochemically oxidized at cathode potentials above 1.1 V, due to the reverse current mechanism [95], [99] allowing unsupported Pt particles to sinter, coalesce into larger particles, and/or migrate into the membrane. HD6 bus membranes from the field contain a Pt band close to the cathode catalyst layer. The location of Pt band is governed by the partial pressure of reactant gases [34], [100]–[102]. When operating with a  $\text{H}_2$  overpressure, all the  $\text{O}_2$  is first completely consumed locally and fast HOR kinetics stimulate further Pt deposition by setting the electrochemical potential of electronically isolated Pt particles near 0 V. With excess  $\text{O}_2$ , the potential of the isolated Pt particles becomes 1 V and no further Pt deposition occurs. Hence, the local position of the Pt band can be found where the molar flux of  $\text{O}_2$  is equal to half the molar flux of  $\text{H}_2$ , thus both gases are completely consumed to form water. PITM is often believed to accelerate membrane degradation [40], [41]. On the other hand, 2800 hour field operated membranes that contained a Pt band vastly

outperformed freshly manufactured membranes under AST conditions [37], [93]. Platinum particle size, shape, location and distribution in the membrane determine the effect on membrane durability [43]–[46]. The effect of platinum in the membrane (PITM) on membrane stability can be investigated by deliberately generating a Pt band in the membrane.

## **2.2. Accelerated membrane durability test (AMDT)**

The AMDT was designed based on the world's largest fuel cell bus fleet of 20 vehicles powered by Ballard's 6<sup>th</sup> generation FCvelocity®-HD6 modules to service the 2010 Vancouver Winter Olympics and beyond. The fleet successfully endured temperatures between  $-12^{\circ}\text{C}$  to  $27^{\circ}\text{C}$ , snowfall from November to May, and a very challenging terrain with frequent up and down hill driving. Evaluation of the extensive operational record and field data of the Whistler bus fleet was used to identify key stressors, their levels, and occurrence. The protocol uses constant and time dependent bus fuel cell stressors at elevated levels. Frequent acceleration and deceleration seen in the duty cycle resulted in fast, mild, repetitive humidity fluctuations. The humidity dropped mildly during acceleration and quickly returned back to a fully humidified state once the level of demanded load was reduced. This was a result of a delayed response of the humidifier to the transient. In most cases the amplitude of changes in humidity was smaller than 10% RH and short in duration. This means that the membrane may not have experienced excessive swelling or shrinking, but its repetitive nature would likely lead to mechanical degradation over a very long period of time.

The AMDT is an application targeted membrane ADT for heavy duty fuel cells. For this reason, it was designed to match specific bus operating conditions, looking at factors like the operating voltage, temperature, and RH. The proposed AMDT stressor levels are carefully chosen in order to avoid failure mode artefacts. The AMDT temperature is allowed to exceed the highest seen operating temperature during bus operation, for purposes of accelerating failure modes. However, the temperature should not exceed the design capabilities of the membrane, e.g. the glass transition

temperature of Nafion®, 110-115 °C, above which mechanical strength is lost, and there is increased gas permeability and less phase separation between ionic and non-ionic portions of the polymer [103]. The baseline AMDT in this study represents the most stressful situations for the FC membrane in the field in terms of voltage, such as idling at bus stops, stop signs, pedestrian crossings and traffic lights. Idling doesn't require much power, resulting in periods of high voltage, causing faster rates of chemical membrane degradation, due to increased gas crossover [23]. Therefore, elevated voltage is used as the primary stressor in the baseline AMDT. Mechanical membrane degradation is achieved by using a relatively aggressive RH cycling regime compared to the bus. Elevated temperature and oxygen concentration are used to further accelerate membrane degradation and reduce time to failure. Elevated temperature increases fuel cell reaction rates, including reactions leading to chemical degradation; increased availability oxygen concentration leads to increased peroxide and subsequent radical formation [25]. The effect of PITM is tested in-situ and the result is included in the AMDT, since Pt band was seen in field operated membranes.

Membrane degradation has two phases: the time prior to leak formation, referred to as "initiation" time, and the leak growth time. Initiation time depends on factors that influence chemical and mechanical degradation, i.e., voltage, temperature, RH levels and the gas permeation rate through the membrane. Once membrane leaks are formed, unrestricted gas crossover commences a period of gradual pinhole growth, followed by rapid pinhole growth. Leak growth rate depends on the concentration of reactant gases and the direction of gas overpressure. Anode overpressure accelerates pinhole growth due to reactant mixing at cathode potentials, which support direct combustion, [57] making hydrogen crossover more detrimental to cell operation than oxygen crossover, after pinholes form [48]. Pinhole growth is terminated once the hole-size is large enough for gases to combust outside the pinhole, which causes damage further in affected areas. A pinhole located close to the MEA outlet is likely to be sealed by water flowing out of the fuel cell, effectively reducing the pinhole growth rate, allowing normal fuel cell operation with small leaks for considerable time periods.

## 2.3. Experimental design and empirical modeling

Accelerated life testing involves the acceleration of failures with the purpose of quantifying the life characteristics of the product at use conditions. Membrane lifetime as a function of a stressor can be identified with an appropriate design of experiment (DOE). Ideally the experimental design should include at least three stress levels for each relevant stressor, in order to observe a decay trend. Some examples of commonly applied DOEs are: full factorials, fractional factorials, screening experiments, response surface analysis, evolutionary operations, and mixture experiments [105]. A full factorial includes all possible combinations of factors, looking at the main effects and all the interactions between factors. Fractional factorials are often preferred, as they look at more factors with fewer runs, assuming that higher order interactions are not significant [106]. Plackett-Burman and Taguchi designs are the two major families of screening experiments that fully or partially ignore all interaction effects. Response surface analysis uses a series of full factorial experiments to generate mathematical equations that describe how factors affect the response, i.e., map the response surface. Fuel cell membrane lifetime can be predicted via extrapolation from accelerated conditions to use conditions with an appropriate empirical lifetime prediction model. Acceleration models are usually based on the physics or chemistry underlying a particular failure mechanism. The most powerful models are: Arrhenius, Eyring, the (inverse) power rule for voltage, the exponential voltage model, two temperature/voltage models, the electro-migration model, three stress models (temperature, voltage and humidity), and the Coffin-Manson mechanical crack growth model [19]. Commonly used lifetime distribution models are: exponential, Weibull, extreme value, lognormal, gamma, Birnbaum-Saunders, and proportional hazards [19].

## **Chapter 3. Experimental**

Accelerated membrane durability tests were designed and performed at various levels of multiple stressors in order to find the acceleration factors for lifetime prediction of PFSA membranes used in FCvelocity®-HD6 modules. MEAs were fabricated for in-situ AMDT testing on a fully automated Ballard standard test station.

### **3.1. Membrane electrode assembly (MEA) fabrication**

Catalyzed gas diffusion electrodes (GDEs) were fabricated by coating a micro-porous layer made of polytetrafluoroethylene (PTFE) and carbon black on a non-woven carbon paper gas diffusion layer substrate, followed by coating a catalyst layer consisting of carbon-supported platinum catalyst and perfluorosulfonic acid ionomer [58]. MEAs were prepared by hot-pressing a standard non-reinforced PFSA ionomer membrane with anode and cathode GDEs. The CeO<sub>2</sub> MEA was prepared in the same way with CeO<sub>2</sub> coated anode and cathode GDEs. CeO<sub>2</sub> coated GDEs were fabricated by spray-coating a mixture solution consisting of a commercial cerium oxide powder (Alfa Aesar, 20–150 nm) and 5% PFSA ionomer solution (Ion Power Inc., 1100 EW) on top of the anode and cathode GDEs [108].

### **3.2. Stack assembly and test station**

MEAs were used to build a 10 cell stack with graphitic bipolar plates using co-flow parallel straight channels. A pressurized bladder ensured uniform compression between MEAs and bipolar plates. External and internal gas leak tests were done before installation of the stack on a test station. For humidification, dry reactant gases flowed through a humidification drum that contained water at the required temperature. The

stack was conditioned by holding the current at 135 A for 24 hours prior to the AMDT. Stack failure was defined as an internal leak rate of 100 sccm through the membrane. All experiments were done at Ballard Power System's testing facility.

### **3.3. Baseline AMDT protocol**

The baseline AMDT applied chemical stress by maintaining the stack voltage at 9 V. RH cycling was achieved by bypassing the cathode humidifier for 66 seconds every 10 minutes, causing the RH to gradually dip to approximately ~ 60% RH at the cathode. The level of hydration in the membrane during the dry cycle is estimated to drop to ~ 80% RH, since the anode remained fully humidified. The ratio of the membrane resistivity measured during the wet and dry cycle was used to estimate the RH during the dry cycle, based on the corresponding conductivity and water content levels known for 100% RH [109], [110]. Buses generally take oxygen from the surrounding air, which contains 21% oxygen. The AMDT temperature and oxygen partial pressure are 85 °C and 45%, respectively. Hydrogen and oxygen gas flow rates were 5 and 10 slpm, respectively. These flows were intentionally high in order to ensure ample reactant supply to the entire MEA surface. The backpressure was set to 0.1 barg, but generally fluctuated by around 0.03 barg during the test. Temperature and pressure sensors were inserted in the fixtures of the manifold at the inlet and outlet in order to provide feedback on the operating conditions. A manual hydrogen sensor was used to check the manifolds for hydrogen leaks. A second hydrogen sensor was placed in the station chamber to detect hydrogen leaking out of the stack. A voltage alarm was set to shut down the station if the voltage dropped below 0.5 V. Alarms for the coolant level and pressure; and reactant pressure were used to report odd operating conditions, helping to keep the conditions within the chosen intervals. Finally, all data was logged in a file, which allowed the operator to investigate problems related to shut down events, or other problematic behavior during test operation.

### 3.4. Complementary AMDT protocols

Complementary tests with certain adjustments to the baseline AMDT protocol were designed to investigate the state of membrane degradation at leak initiation, the effects of RH cycling and platinum in the membrane (PITM) on membrane durability. The temperature and oxidant levels were kept at 85 °C and 45% O<sub>2</sub>, respectively, in all complementary testing. The early stages of membrane degradation were investigated in the initiation test, which applied baseline AMDT conditions until signs of initial hydrogen leak formation across the membrane were detected, such as increased voltage fluctuations. Tests at 90% and 100% constant RH were performed to capture the lifetime difference between tests at constant RH and with RH cycling, i.e., the baseline AMDT. The lifetime differences helped to better understand the effect of RH cycling. Tests with PITM are considered to be more realistic, since a Pt band was observed in field membranes after 2800 h of bus operating conditions. These bus membranes displayed superior durability compared to fresh membranes when exposed to AST conditions, observed as extended lifetime, and lower fluoride release rates. More details on the lifetime extension observed in the 2,800 h field membrane can be found in Appendix A [37]. Due to the interesting findings the effect of PITM was further studied, this time under AMDT conditions, using membranes with an artificially in-situ deposited Pt band. A proprietary Ballard protocol was used to generate a Pt band in the membrane either prior to or during the baseline AMDT operation. In the first approach 1,000 PITM generating cycles were used prior to baseline AMDT exposure in an AMDT. In a second approach PITM concentration was controlled by integrating a single PITM generating cycle after every 6<sup>th</sup> RH cycle of the AMDT. More information on the findings on initiation, the effect of RH, and PITM can be found in Appendix B. A sensitivity analysis was done in order to further study the effect of various PITM concentrations on membrane durability. PITM concentration was controlled by integrating a single PITM generating cycle after every 12<sup>th</sup> and 24<sup>th</sup> RH cycle of the baseline AMDT. The PITM-AMDT after every 12<sup>th</sup> AMDT RH cycle with PITM was performed at air conditions. Field operated samples under investigation were extracted from Whistler bus stacks at 2,800 h, 4,400 h and 8,200 h. The structure of Pt particles in field and PITM-AMDT membranes was

compared with TEM. The acceleration factor used for PITM in the empirical model is based on the results of the PITM sensitivity study and the TEM study, which are described in more detail in Appendix C.

Two additional voltage and temperature levels were tested in order to find the membrane life behavior with increasing and decreasing voltage and temperature, in a full factorial experimental design. The additional voltage levels were 0.75 V and 0.82 V. The additional temperature levels were 75 °C and 90 °C. The results provided the acceleration factors used for extrapolation to bus weighted voltage average and average temperature. Finally, cerium oxide additive was tested in modified MEAs under baseline AMDT conditions and the observed lifetime extension was used for prediction purposes.

### **3.5. Characterization methods**

External and internal gas leak tests were performed every 48 hours to assess membrane health. The fluoride concentration was measured from effluent water and the total fluoride loss was calculated using a method described in [93]. The stack was considered failed at an internal leak rate of 100 sccm, corresponding to the limiting leak rate through the membrane of 10 sccm per cell. After failure, the stack was disassembled, and individual MEA leak tests were performed. Analysis by Infra-Red camera (Kaiser RTI T620 FLIR) was done to identify the location of leaks. In the IR camera test, hydrogen is supplied under a firmly fixed MEA in a custom fixture and reacts with oxygen from air when allowed to leak through holes in the membrane. The location and size of pinholes can be determined by the location and magnitude of regions of increased temperature. The least and most damaged MEAs were further inspected by a Philips XL30 scanning electron microscope (SEM). Samples were prepared by casting MEAs in epoxy pucks, which were polished in a Struers TegraPol-11 polisher with 120–1200 grit silicon carbide paper, and then carbon coated with an Edwards Scancoat Six Sputter Coater. Micrographs were taken using a backscatter detector at 20 kV. The membrane thickness was measured in 12 different spots and the morphology of transfers was found in cross-sectional and surface images. Membrane

thinning was considered to be present when the EOL membrane thickness was below three standard deviations of the initial thickness. Energy-dispersive X-ray spectroscopy (EDS) was used to measure the Pt concentration in the Pt band.

Transmission electron microscopy (TEM) is a microscopy technique in which a beam of electrons is transmitted through an ultra-thin specimen. As the electrons pass through the specimen, their interaction with the specimen forms an image, which is magnified and focused onto a fluorescent screen, layer of photographic film, or detected by a CCD camera. TEM was used to compare the structure of Pt particles in field operated membranes to in situ membranes with artificially grown Pt bands. The goal was to identify the type of Pt particles that lead to enhanced membrane durability, and propose an underlying mechanism for the phenomenon. The other reason for TEM analysis was to identify the in-situ generated Pt particles that most resembled the field Pt particles in the membrane. The lifetime effect of those Pt particles was then meant to be used as the acceleration factor for the effect of PITM in the empirical model. MEAs were left to dry at ambient conditions for 2 hours prior to cutting out 1 cm<sup>2</sup> pieces from the outlet for TEM sample preparation. TEM sample preparation was done by removing the GDLs and embedding triangular shaped CCMs in Araldite 502 epoxy. The epoxy was cured in an oven at 70 °C for 12 hours. A LEICA EM UC 6 ultra-microtome was used to prepare 80 - 100 nm slices of the embedded CCM samples in epoxy, using a freshly prepared glass knife. The slices were collected in a water bath and placed on formvar coated copper grids with a 200 μm mesh, model FF200-Cu. Two transmission electron microscopes were used for nano-imaging at 200 kV: STEM HITACHI-8100 and STEM FEI TECNAI Osiris. All TEM imaging was done at 4D Labs. Image processing was done with the ImageJ software package.

In the case of additive use, neutron activation analysis was used to determine the concentration of CeO<sub>2</sub> in the MEA before and after the AMDT. The amount of CeO<sub>2</sub> was measured in the CCM, cathode and anode catalyst layer and in the membrane. Samples were first dried in an oven and then grinded into powder, which was analyzed with NAA.

A non-invasive H<sub>2</sub>/N<sub>2</sub> method was used to measure the individual leak rate of MEAs in bus stacks. The H<sub>2</sub>/N<sub>2</sub> method injects hydrogen at the anode and nitrogen at the cathode at 30 °C and/or 60 °C at an anode overpressure of 0.13 or 0.3 barg. The amount of hydrogen leaking through the membrane to the cathode is measured as voltage, which is then correlated to a specific leak rate.

## Chapter 4. Model description

Two computational methods were used in the lifetime prediction model: stack level and MEA level prediction. Stack level prediction was based on the assumption of no significant effect of interactions between stressors. On the other hand, the MEA level prediction takes interactions, individual MEA lifetimes, and suspended cells into account.

### 4.1. Stack level prediction

The general approach used in the stack level prediction approach is explained in the flowchart in Figure 3.

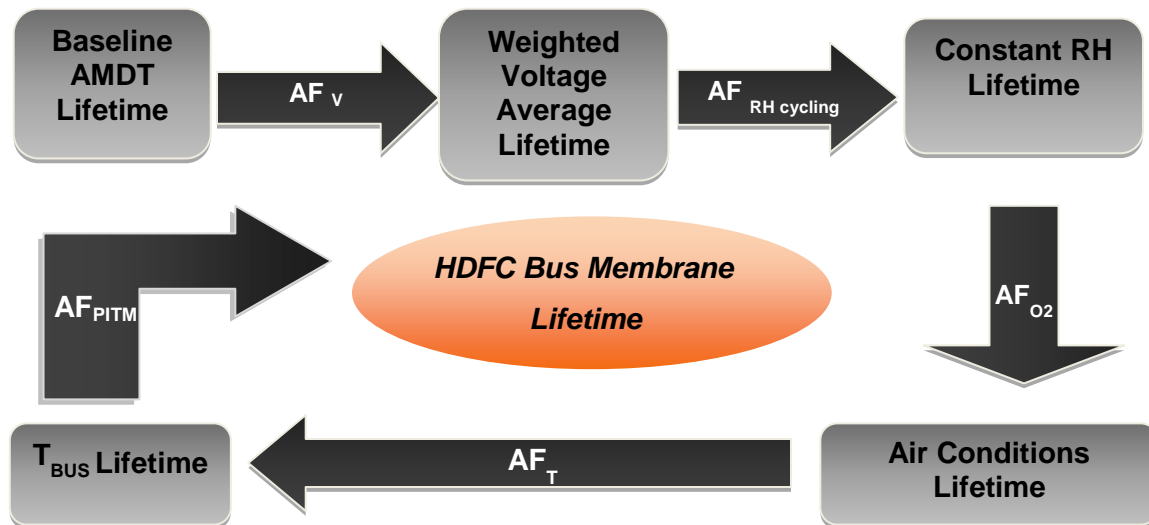


Figure 3. Flowchart of stack based empirical model.

The model starts with the average stack lifetime of four baseline AMDT runs. The first AF represents the effect of cell voltage, which was deemed the most influential stressor in this work, considering its dominant role in the iron ion redox cycle that controls the rate of chemical degradation during fuel cell operation [71]. AMDT lifetime at bus average voltage was calculated from the equation found by least square approximation of the AMDT lifetime at three voltage levels. The AF for voltage was found as the ratio of the AMDT lifetime at bus average voltage and the baseline. Voltage is a relatively strong factor compared to the other parameters and was therefore prioritized by considering a relatively wide range in the critical region of cell voltages. The second AF represents the combined effects of relative humidity (RH), which is of relevance for both chemical and mechanical degradation through the effective membrane hydration level and humidity cycling, respectively. The average use RH level was therefore used for the chemical portion of the AF while the amplitude of RH cycling was used for the mechanical portion, relative to the corresponding AMDT stressor levels. The third AF, representing O<sub>2</sub> concentration, was obtained by the ratio of the AMDT stack lifetimes at 21% and 45% O<sub>2</sub>. This AF was used as a fixed accelerator to increase chemical degradation (via hydrogen peroxide formation from oxygen) during the AMDT experiments, considering that most use level applications would operate at 21% O<sub>2</sub> (air conditions). Next, membrane lifetime was found at the average use level temperature with the help of the least square equation found from AMDT membrane lifetime data at three temperature levels. This stressor is expected to accelerate both chemical and mechanical degradation. The AF for temperature was then calculated as the ratio of AMDT lifetime at the average use level and the baseline. Finally, the AF for PITM was found as the ratio of AMDT lifetime with artificially generated PITM at use level and baseline AMDT lifetime without PITM. PITM has a reverse acceleration factor, due to the mitigating effect of the Pt band in the membrane [37], [111]. The final outcome of the

empirical model is the predicted stack lifetime at use level conditions, which is obtained by multiplying the AMDT baseline stack lifetime by all five AFs. The entire calculation is summarized by Eq. 8, where the respective positions of the factors are irrelevant.

$$BusLifetime(V, RH, Ox, T, PITM) = \sum_{i=1}^n (L_i * F_i) * AF_{RH} * AF_{O_2} * AF_T * AF_{PITM} \quad (8)$$

where  $L_i$  is the lifetime at voltage  $i$ , and  $F_i$  is the frequency of voltage  $i$ .

## 4.2. MEA level prediction

In the MEA level prediction, the individual MEA lifetimes and interactions between stressors are considered for the calculation of AFs. Since the individual cell leak rates are only revealed at the end of the AMDT, their initiation times were numerically calculated with the help of Genetic Algorithm (GA), which is an optimization method available in MATLAB's optimization toolbox, OptimTool. The main assumption is that the sum of the leak rates of the individual cells is equal to the total measured stack leak rate. In reality the sum of individual cell leak rates can be higher than the stack leak rate, due to growth of pinholes during the leak test. In order to calculate the theoretical initiation times of each cell in the stack, the second assumption is that all cells follow an identical leak growth rate, i.e., slope, since they are all exposed to the same conditions in the stack. The cell initiation times correspond to the time at which the value of the line of the leak growth slope is equal to zero. The previous stack leak rate and the time at which it was measured are known parameters. The process can be modeled with the slope of a line that corresponds to the leak rate growth in time. The previous leak rate, multiplied by the slope of leak growth is equal to the next leak rate, where the stack leak rate is broken into the sum of the leak rates of the 10 individual MEAs at both points in time. Genetic Algorithm (GA) was used to minimize the error of the equation and determine the initiation time of each MEA as well as the slope of leak growth. The theoretically calculated initiation times were then used to calculate the failure time at

which each cell would reach a leak rate of 10 sccm, based on the slope of leak growth. The following equation was formulated:

$$\sum_{i=1}^{10} CLR_i(T_{EOL}) = a.SLR(T_{EOL-1}) \quad (9)$$

where  $CLR(T_{EOL})$  is the cell leak rate at end of life for cell  $i$ ,  $SLR(T_{EOL-1})$  is the stack leak rate tested one time step before the end of life, and  $a$  is the slope.  $(T_{EOL})$ , the time at end of life;  $(T_{EOL-1})$ , time at the point of the previous leak test; and the individual cell leak rates at EOL are the known parameters. The parameters provided to OptimTool were the source equation (Eq.9), the number of unknown variables (10 initiation times + slope = 11), and their boundary conditions. The time at a leak rate of 10 sccm for each cell was then be calculated using the equation of a line and the slope.

The sum of all individual cell leak rates can then be written as:

$$\begin{aligned} y = & ((L_1 - x_{11} * (T_2 - x_1) * Heaviside(T_2 - x_1))^2 + (L_2 - x_{11} * (T_2 - x_2) * Heaviside(T_2 - x_2))^2 + \\ & (L_3 - x_{11} * (T_2 - x_3) * Heaviside(T_2 - x_3))^2 + (L_4 - x_{11} * (T_2 - x_4) * Heaviside(T_2 - x_4))^2 + (L_5 - \\ & x_{11} * (T_2 - x_5) * Heaviside(T_2 - x_5))^2 + (L_6 - x_{11} * (T_2 - x_6) * Heaviside(T_2 - x_6))^2 + (L_7 - x_{11} * \\ & (T_2 - x_7) * Heaviside(T_2 - x_7))^2 + (L_8 - x_{11} * (T_2 - x_8) * Heaviside(T_2 - x_8))^2 + (L_9 - x_{11} * (T_2 - \\ & x_9) * Heaviside(T_2 - x_9))^2 + (L_{10} - x_{11} * (T_2 - x_{10}) * Heaviside(T_2 - x_{10}))^2 + (PL - (x_{11} * (T_1 - \\ & x_1) * Heaviside(T_1 - x_1) + x_{11} * (T_1 - x_2) * Heaviside(T_1 - x_2) + x_{11} * (T_1 - x_3) * Heaviside(T_1 - \\ & x_3) + x_{11} * (T_1 - x_4) * Heaviside(T_1 - x_4) + x_{11} * (T_1 - x_5) * Heaviside(T_1 - x_5) + x_{11} * (T_1 - x_6) * \\ & Heaviside(T_1 - x_6) + x_{11} * (T_1 - x_7) * Heaviside(T_1 - x_7) + x_{11} * (T_1 - x_8) * Heaviside(T_1 - x_8) \\ & + x_{11} * (T_1 - x_9) * Heaviside(T_1 - x_9) + x_{11} * (T_1 - x_{10}) * Heaviside(T_1 - x_{10})))^2) \end{aligned} \quad (10)$$

where  $y$  is the measured stack leak rate at EOL;  $x_1, x_2, \dots, x_{10}$  are the cell initiation times;  $L_1, L_2, \dots, L_{10}$  are the measured cell leak rates at EOL;  $x_{11}$  is the cell leak growth rate, which is identical for all cells;  $PL$  is the previous stack leak rate measured before failure at time  $T_1$ , and  $T_2$  is the time at which the EOL leak rate was measured. The GA was used to minimize the error of Eq. 4 and numerically determine the leak initiation time

of each MEA as well as the cell leak growth rate. The equation was squared to avoid negative numbers while the Heaviside step function was used to eliminate any leak contributions before initiation. The resulting initiation times were then used as inputs for calculating the failure time at which each cell would reach a leak rate of 10 sccm, based on the acquired leak growth rate.

The probability density function (*pdf*) and cumulative distribution function (*cdf*) are important statistical functions used to describe a life distribution. Once known, almost any other reliability measure of interest can be derived or obtained. The probability density function (*pdf*) is calculated as the slope between each point in the *cdf*, so the *pdf* is the derivative, or rate of change, of the *cdf*. Therefore, if  $P(x)$  is the *cdf* and  $p(t)$  is the *pdf*, then:

$$P(x) = \int_{-\infty}^x p(t) dt \quad (11)$$

$$P'(x) = p(x) \quad (12)$$

The Weibull life distribution is used in all stressor life distributions, which accounts for the characteristic distribution of failure in the stack. In its most general case, the 3-parameter Weibull *pdf* is defined by:

$$f(t) = \frac{\beta}{\eta} \left( \frac{t-\gamma}{\eta} \right)^{\beta-1} e^{-\left( \frac{t-\gamma}{\eta} \right)^\beta} \quad (13)$$

where  $\beta$  is the shape parameter,  $\eta$  is the scale parameter and  $\gamma$  is the location parameter. The 3-parameter Weibull *cdf*,  $F(t)$  is equal to the unreliability,  $Q(t)$ :

$$Q(t) = F(t) = 1 - e^{-\left( \frac{t-\gamma}{\eta} \right)^\beta} \quad (14)$$

The reliability function for the 3-parameter Weibull,  $R(t)$  distribution is then given by:

$$R(t) = e^{-\left(\frac{t-\gamma}{\eta}\right)^\beta} \quad (15)$$

The Weibull failure rate function,  $\lambda(t)$  is given by:

$$\lambda(t) = \frac{f(t)}{R(t)} = \frac{\beta}{\eta} \left(\frac{t-\gamma}{\eta}\right)^{\beta-1} \quad (16)$$

Populations with  $\beta < 1$  exhibit a failure rate that decreases with time, populations with  $\beta = 1$  have a constant failure rate and populations with  $\beta > 1$  have a failure rate that increases with time.

When using multiple stressors the General Log Linear (GLL) – Weibull life-stress relationship can be used where each stressor has a specific underlying relationship, and all stressors share an underlying life distribution [20]. The GLL allows the user to choose individual transformation functions for each stressor, and can be derived by setting  $\eta = L(X)$ , where

$$L(\underline{X}) = e^{\alpha_0 + \sum_{j=1}^n \alpha_j X_j} \quad (17)$$

The result is the following GLL-Weibull pdf:

$$f(t, \underline{X}) = \beta \cdot t^{\beta-1} e^{-\beta \left( \alpha_0 + \sum_{j=1}^n \alpha_j X_j \right)} e^{-t^\beta e^{-\beta \left( \alpha_0 + \sum_{j=1}^n \alpha_j X_j \right)}} \quad (18)$$

where the total number of unknowns to solve for is  $n + 2$  (i.e.,  $\beta, \alpha_0, \alpha_1, \dots, \alpha_n$ ).

Separate functions were assigned to each individual stressor for the empirical model. Voltage used the inverse power law, and temperature used the Arrhenius relationship. The exponential function was used as for oxygen concentration. RH cycling and PITM were assigned indicator values, 0 and 1, where 0 indicated the presence of RH cycling and no PITM; and 1 indicated 100% RH and the presence of PITM, respectively. The exponential function was assigned to the indicator values as well.

The Arrhenius reaction rate equation is given by:

$$R(t) = Ae^{-\frac{E_A}{KT}} \quad (19)$$

where  $R$  is the speed of reaction;  $A$  is an unknown non-thermal constant;  $E$  is the activation energy (  $eV$  );  $K$  is the Boltzman's constant ( $8.617385 \times 10^{-5} eVK^{-1}$ );  $T$  is the absolute temperature (Kelvin). The activation energy is the energy that a molecule must have to participate in the reaction. In other words, the activation energy is a measure of the effect that temperature has on the rate of reaction. The Arrhenius life-stress model is formulated by assuming that life is proportional to the inverse reaction rate of the process, thus the Arrhenius life-stress relationship is given by:

$$L(V) = Ce^{\frac{B}{V}} \quad (20)$$

where  $L$  represents a quantifiable life measure, such as mean life, characteristic life, median life, or  $B(x)$  life, etc;  $V$  represents the stress level (formulated for temperature and temperature values in absolute units, degrees Kelvin or degrees Rankine );  $C$  is one of the model parameters to be determined, ( $C > 0$ );  $B$  is another model parameter to be determined.

The inverse power law (IPL) model (or relationship) is commonly used for non-thermal accelerated stresses and is given by:

$$L(V) = \frac{1}{KV^n} \quad (21)$$

where  $L$  represents a quantifiable life measure, such as mean life, characteristic life, median life,  $B(x)$  life, etc;  $V$  represents the stress level;  $K$  is one of the model parameters to be determined, ( $K > 0$ );  $n$  is another model parameter to be determined.

The GLL relationship then becomes:

$$\eta = e^{\alpha_0 + \alpha_1 \frac{1}{V_1} + \alpha_2 \ln(V_2) + \alpha_3 V_3 + \alpha_4 V_4 + \alpha_5 V_5} \quad (22)$$

The resulting relationship after performing the transformations is

$$\eta = e^{\alpha_0} e^{\alpha_1 \frac{1}{V_1}} e^{\alpha_2 \ln(V_2)} e^{\alpha_3 V_3} e^{\alpha_4 V_4} e^{\alpha_5 V_5} = e^{\alpha_0} e^{\alpha_1 \frac{1}{V_1}} V_2^{\alpha_2} e^{\alpha_3 V_3} e^{\alpha_4 V_4} e^{\alpha_5 V_5} \quad (23)$$

Therefore, the parameter  $B$  of the Arrhenius relationship is equal to the log-linear coefficient  $\alpha_1$ , and the parameter  $n$  of the inverse power relationship is equal to  $(-\alpha_2)$ . Coefficients  $\alpha_3, \alpha_4, \alpha_5$  are log-linear coefficients for the exponential distribution of  $O_2$  concentration, RH cycling, and PITM. Therefore  $\eta$  can also be written as:

$$\eta = e^{\alpha_0} e^{\frac{B}{V_1}} V_2^n e^{\alpha_3 V_3} e^{\alpha_4 V_4} e^{\alpha_5 V_5} \quad (24)$$

The activation energy of the Arrhenius relationship can be calculated by multiplying  $B$  with Boltzmann's constant.

Maximum Likelihood Estimation (MLE) was used to calculate the parameters of the GLL-Weibull distribution and the AFs. This method takes into account suspended cells, i.e., those that did not fail at the end of the experiment. The expression used is

$$\ln(l) = \Lambda = \sum_{i=1}^{F_e} N_i \ln \left[ \beta \cdot T_i^{\beta-1} e^{-T_i^\beta \cdot e^{-\beta(\alpha_0 + \sum_{j=1}^n \alpha_j x_{i,j})}} \right]$$

$$- \sum_{i=1}^S N'_i (T'_i)^\beta e^{-\beta(\alpha_0 + \sum_{j=1}^n \alpha_j x_{i,j})} + \sum_{i=1}^{FI} N''_i \ln [R''_{L_i} - R''_{R_i}] \quad (25)$$

where

$$R''_{L_i} = e^{-\left( T''_{L_i} e^{-\beta(\alpha_0 + \sum_{j=1}^n \alpha_j x_j)} \right)^\beta} \quad (26)$$

$$R''_{R_i} = e^{-\left( T''_{R_i} e^{-\beta(\alpha_0 + \sum_{j=1}^n \alpha_j x_j)} \right)^\beta} \quad (27)$$

and  $F_e$  is the number of groups of exact times-to-failure data points,  $N_i$  is the number of times-to-failure in the  $i^{th}$  time-to-failure data group,  $\lambda$  is the failure rate parameter (unknown),  $T_i$  is the exact failure time of the  $i^{th}$  group,  $S$  is the number of groups of suspension data points.  $N'_i$  is the number of suspensions in the  $i^{th}$  group of suspension data points,  $T'_i$  is the running time of the  $i^{th}$  suspension data group,  $FI$  is the number

of interval data groups,  $N_i''$  is the number of intervals in the  $i^{th}$  group of data intervals,  $T_{L_i}''$  is the beginning of the  $i^{th}$  interval,  $T_{R_i}''$  is the ending of the  $i^{th}$  interval.

The result is a failure distribution at all stressor levels. Here, the weighted bus voltage average is between 0.6 – 0.99 V, is ~ 0.8 V. The bus use level at which the lifetime predictions were calculated was 0.8 V, 58 °C, air conditions, 100% RH and with PITM.

### **4.3. Prediction of bus lifetime with CeO<sub>2</sub>**

The membrane lifetime with the use of CeO<sub>2</sub> as an additive was found under baseline AMDT conditions. The bus membrane lifetime with the use of CeO<sub>2</sub> is predicted based on

- The lifetime extension seen in the AMDT with CeO<sub>2</sub> coated membranes
- The predicted bus lifetime without CeO<sub>2</sub>
- CeO<sub>2</sub> washout rates, measured from two historical Ballard AMDTs
- Acceleration factor decay based on CeO<sub>2</sub> washout

### **4.4. H<sub>2</sub>/N<sub>2</sub> method for in-situ MEA leak testing**

The H<sub>2</sub>/N<sub>2</sub> in-situ leak testing method is a newly developed method which was tested on the AMDT stacks. This is a test is non-invasive and can be used to regularly monitor the leak rate of individual cells in a stack during AMDTs without disturbing testing. It can be used to measure the initiation times of MEAs in a stack during the AMDT, instead of generating theoretical initiation times. However, at the time, the H<sub>2</sub>/N<sub>2</sub> was still in development stages, thus for consistency all AMDT initiation times were calculated by GA. However, the method was successfully used on bus stacks. The H<sub>2</sub>/N<sub>2</sub> method injects hydrogen at the anode and nitrogen at the cathode at 30 or 60 °C. Thus, no potentially harmful reactions to the membrane or other MEA components take place.

The overpressure used was 0.13 and 0.3 barg. The amount of hydrogen that leaksthrough the membrane at a given dP to the cathode was measured as voltage, which was correlated to a specific leak rate. The relationship between the leak rate from anode to cathode and the flow rates and pressures is described below [113].

$$P_{H,cathode} = \frac{L}{Q_N + Q_w + L} \quad (28)$$

$$Q_w = \frac{P_w}{P_c} (Q_N + Q_w) = \frac{\frac{P_w}{P_c} Q_N}{1 - \frac{P_w}{P_c}} \quad (29)$$

$$P_{H,c} = \frac{L}{L + Q_N + \left( 1 + \frac{\frac{P_w}{P_c}}{1 - \frac{P_w}{P_c}} \right)} \quad (30)$$

$$V = \frac{RT}{2F} \ln \left( \frac{P_{H,c}}{P_{H,a}} \right) = \frac{RT}{2F} \ln \left( \frac{P_{H,c}}{P_a - P_c} \right) \quad (31)$$

where  $L$  is the leak rate ( $\text{cm}^3\text{-H}_2 \text{ min}^{-1}$ ),  $P_c$  is the pressure at cathode,  $P_a$  is the pressure at anode,  $Q_N$  is the nitrogen flow rate at cathode,  $Q_w$  is the water flow rate at the cathode,  $Q_H$  is the hydrogen flow rate at cathode exit,  $P_w$  is the saturation vapor pressure of water,  $Q_H = L$  is the steady state mass balance on  $\text{H}_2$ .

The following linear relationship between leak rates and pressure is assumed:

$$L_1 = L_2 * (P_1/P_2) \quad (32)$$

where  $L_1$  and  $L_2$  are the leak rates; and  $P_1$  and  $P_2$  are the pressures. To convert  $H_2$  flow rates to air flow rates, the  $H_2$  flow rate is divided by 2, as air has  $\sim 2.1$  x higher viscosity.

## Chapter 5. Results and validation of methodology

The AMDT complementary conditions are summarized in Table 1. Significant lifetime differences were observed at constant RH compared to the baseline AMDT, emphasizing the effect of RH cycling. The failure mechanisms with RH cycling were notably different, with more cracks and tears, larger holes, and more localized thinning. The constant RH membranes experienced more chemical degradation resulting in global thinning, and less crack formation, with smaller and fewer pinholes. Pinholes were observed in all regions of the MEA, i.e., inlet, middle and outlet.

**Table 1. AMDT series designed for stack based empirical model.**

Name	Voltage (V)	Temperature (T)	RH (%)	O <sub>2</sub> (%)	PITM Gen. Cycles	Lifetime (h)
Baseline Avg.	0.9	85	RH cycling	45	-	270
Const. RH 1	0.9	85	100 %	45	-	600
Const. RH 2	0.9	85	90%	45	-	470
Air Conditions	0.9	85	RH cycling	21	-	420
PITM-1	0.9	85	RH cycling	45	1,000 Prior To AMDT	400
PITM-2	0.9	85	RH cycling	45	Every 6 <sup>th</sup> RH Cy	660
Modified V	0.82	85	RH cycling	21	-	830
Modified T	0.9	75	RH Cycling	45	-	480
Cerium Oxide	0.9	85	RH cycling	45	-	1,690

2,800 h field operated MEAs exhibited superior durability compared to freshly manufactured MEAs under AST conditions. Further information on enhanced field membrane durability is provided in Appendix A. This prompted further testing of MEAs with artificially generated Pt bands under AMDT conditions, PITM-1 and PITM-2. PITM-1 applied 1,000 PITM generating cycles before exposure to AMDT conditions. PITM-2 integrated a single PITM generating cycling into the AMDT protocol after every 6<sup>th</sup> RH cycle. Both PITM-MEAs exhibited longer lifetime than the baseline AMDT, confirming the initial result of the 2,800 h field membrane. PITM-2 achieved 2x the baseline lifetime with very high Pt concentrations in the membrane, i.e., 60x more PITM than in the bus at the outlet. Furthermore, at EOL the membranes had no significant membrane thinning, in good agreement with extremely low fluoride loss, accompanied by high mechanical strength, close to that of fresh membranes. Thus, it was concluded that PITM enhanced membrane stability and durability in the case of the tested MEAs. More details on the findings on membrane lifetime and material property changes due to RH cycling and PITM are provided in Appendix B.

PITM-1 was chosen for empirical modeling purposes based on the results of a sensitivity analysis. The sensitivity analysis was done based on EDS and TEM characterization. The effect of PITM concentration, Pt particle shape, size and distribution in the membrane were investigated. EDS was used to measure the concentration of Pt in the Pt band. TEM was used to image the structure and distribution of Pt particles in the membrane. Curly dendritic Pt particles seen in the PITM-1 membrane closely resembled those seen in bus membranes. Another reason for choosing PITM-1 was that the Pt particles were planted in the membrane prior to exposure to AMDT degradation, which is assumed to better represent the situation in bus membranes the most, where the Pt band forms very early during operation, as well. The level of chemical and mechanical degradation during bus operation is much lower than in the AMDT. Thus, the protective Pt band forms early enough during bus operation, to have a significant impact on membrane stability, even at low PITM concentrations. Experiments used in the PITM sensitivity analysis are shown in Table 2, along with the average PITM concentration at MEA outlets, which had the highest Pt concentration. The study showed that curly dendritic (PITM-1), tree-like (PITM-2, PITM-

3) and star shaped Pt particles contributed to membrane stability. These particles contained higher amounts of Pt(111) which is the most catalytically active Pt facet. Thus, potential participation of such Pt particles in H<sub>2</sub>O<sub>2</sub> quenching and consumption of crossover gasses is expected to result in increased membrane stability. The level of H<sub>2</sub>O<sub>2</sub> quenching due to PITM was estimated to be up to 84% and 97% for PITM-1 and PITM-2, respectively. On the other hand cubic Pt particles (PITM-4) had a negligible effect on membrane stability, and did not result in visible lifetime extension. More details on the results of the PITM sensitivity study can be found in Appendix C.

**Table 2. Field operated membrane (FOM) and AMDT samples for TEM.**

Sample	Conditions	Lifetime (h)	PITM Concentration (ppm)
PITM-1	100 Pt cycles prior to Baseline	405	18,000
PITM-2	Baseline with Pt cycles every 6 <sup>th</sup> RH cycle	660	40,000-60,000
PITM-3	Baseline @ 21% Ox with Pt cycles every 12 <sup>th</sup> RH cycle	564	22,000
PITM-4	Baseline with Pt cycles every 24 <sup>th</sup> RH cycle	243	17,600
FOM 2800	Bus field return after 2,800 hours	N/A	3,600
FOM 4400	Bus field return after 4,400 hours	N/A	5,400
FOM 8200	Bus field return after 8,200 hours	N/A	7,000

ANOVA analysis was performed on the data available in Table 1 to evaluate the main and interaction effects of voltage, temperature, O<sub>2</sub> concentration and RH on membrane life. Temperature and voltage were found to have the most significant effect on membrane lifetime. Therefore, a full factorial Design of Experiment (DOE) at 3 levels was proposed in order to expand on the previous 2 data points. Thus, the investigated voltage levels were now to 0.75, 0.82 and 0.9 V. And the three temperature levels were

now 75, 85 and 90 °C. The AMDTs used 45% O<sub>2</sub> concentration and RH cycling. Table 3 presents the DOE for voltage and temperature, expanding the stressor levels from two to three, for increasing the confidence in the model parameters. The fitted function equations were then used extrapolate from AMDT voltage and temperature stress levels to use levels. It was possible to predict the rate of decrease in lifetime using a power law function for voltage, and an exponential function for temperature, shown in Figure 4. The results of the ANOVA analysis can be found in Appendix D.

**Table 3. Experimental design for voltage and temperature.**

Voltage (V)	Temperature (°C)	Lifetime (h)
0.9	90	180
0.82	85	340
0.75	75	1510
0.9	75	480
0.82	75	690
0.75	85	520
0.9	85	270

Additional tests at 21% O<sub>2</sub> were done at 0.9 V and 90 °C; and 0.82 V and 85 °C to increase model accuracy by adding O<sub>2</sub> - T and O<sub>2</sub> -V interactions. Both tests used RH cycling.

**Table 4. Additional experiments at 21% O<sub>2</sub>.**

O <sub>2</sub> (%)	Voltage (V)	Temperature (°C)	Lifetime (h)
21	0.82	85	840
21	0.9	90	340

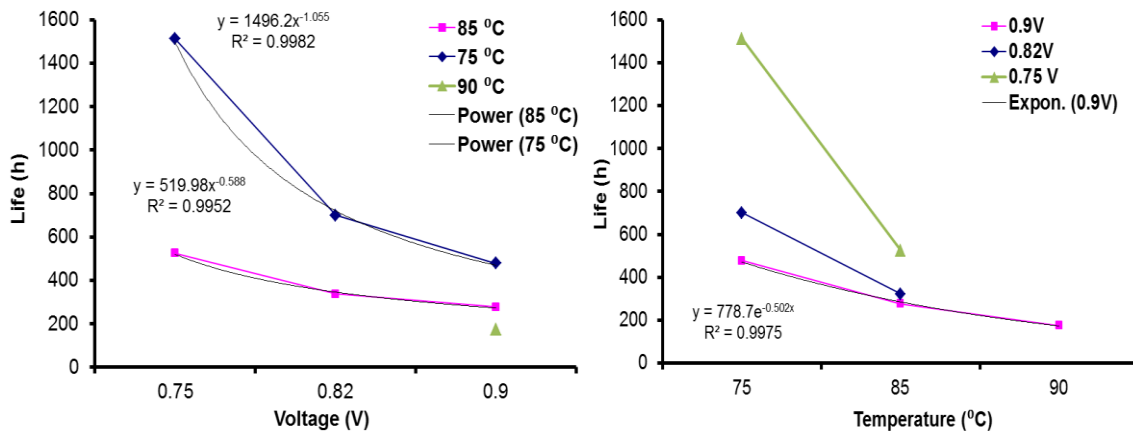


Figure 4. Decay trends of voltage and temperature at 0.9V, 45% O<sub>2</sub>, RH cycling.

The collected lifetime data was used for empirical modeling in the stack and MEA level approach, described in Chapters 4.1 and 4.2. The results of both approaches are presented in the next section.

## 5.1. Stack level approach

The trend line equations for voltage and temperature data was used to calculate membrane lifetime at bus use levels. The acceleration factor for O<sub>2</sub> was calculated by dividing the membrane lifetimes at the 2 different levels available. Similarly, in the case of RH cycling and PITM, acceleration factors were found as the ratio of AMDT life with and without RH cycling or PITM, respectively. First, the lifetime is calculated at each voltage the weighted average lifetime at ~ 0.8 V is then multiplied by the AF for RH cycling, temperature, O<sub>2</sub> and PITM. Stack initiation time was also used as a model input instead of the failure time at 100 sccm, to predict bus membrane initiation time. The initiation time and membrane lifetime at 100 sccm were calculated based on the power law for voltage and the exponential function for temperature, and the results are shown in Table 5 along with the  $\pm 25\%$  error. Thus, for the 'typical Whistler bus' leak initiation should occur around 10,500 hours and a stack failure is expected at 17,500 hours. The

worst case scenario predicts a 7,800 h initiation time, and 13,100 h failure time. The best case scenario predicts a 13,000 h initiation time, and failure at 21,900 h.

**Table 5. Stack based Whistler bus predicted initiation and failure time.**

	<b>Initiation (h)</b>	<b>Life (h)</b>
Prediction	10,500	17,500

The empirical model calculations are embedded in an Excel Macro file, which calculates the initiation time and the lifetime of all the Whistler and Oslo buses, as well as all the stacks in Whistler buses, based on their operating conditions. The model also provides prediction of membrane lifetime with the use of CeO<sub>2</sub> as a radical scavenging agent for mitigation of chemical membrane degradation. The calculation for the lifetime prediction with CeO<sub>2</sub> is shown in the next chapter.

## **5.2. Membrane lifetime with CeO<sub>2</sub>**

The membrane lifetime with CeO<sub>2</sub> coated membranes was evaluated under AMDT conditions. There was a very significant lifetime enhancing effect of CeO<sub>2</sub> and the MEAs did not develop leaks even after 1368 hours, when the test was first stopped. This lifetime is 5 times longer than the baseline average lifetime of 277 hours. MEAs were tested in order to determine the remaining amount of CeO<sub>2</sub> with neutron activation analysis (NAA). It was found that 14% of the CeO<sub>2</sub> was lost from the membrane (BOL conditioned). The remaining MEAs were stored in the stack, and the test was later continued until 1690 hours, with occasional signs of an increasing leak rate, that dropped back to a 1 – 2 sccm, shown in Figure 5. At this point the lifetime is 6.25 times longer than the baseline average. The stack could have operated longer but was taken off the station in order to run other tests.

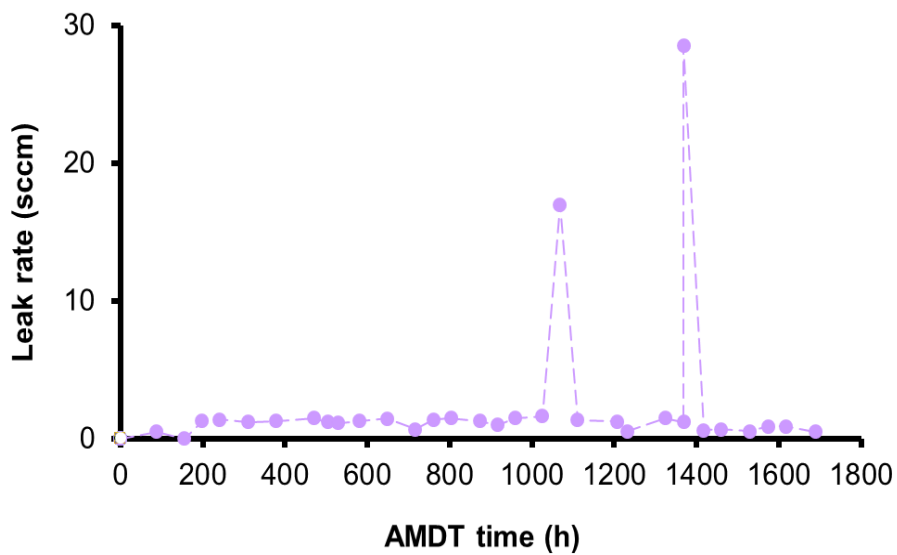


Figure 5. Leak rate development in time of CeO<sub>2</sub> membrane.

Historical CeO<sub>2</sub> washout rates from two Ballard AMDTs were used for lifetime prediction purposes. One AMDT applied load cycling and the other one used a constant voltage hold. The AMDT with load cycling had a higher washout rate than the AMDT with a constant voltage hold. This indicates that the additive would have a lower impact on membrane lifetime when exposed to the dynamic load cycle of the bus, compared to stationary applications for example. The washout rates were fit to exponential decay curves, shown in Figure 6.

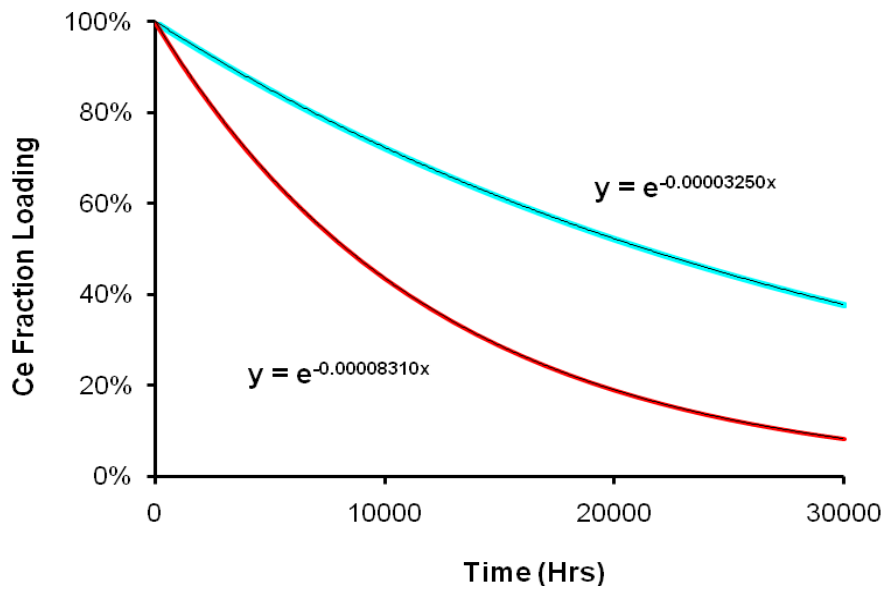


Figure 6. Additive washout with driving cycle (red) and voltage hold (blue) AMDT.

An acceleration factor was defined as the lifetime extension expected at a certain amount of remaining additive. Therefore, an acceleration factor of 6.25 was assigned to an 86 % residual CeO<sub>2</sub> content, based on the assumption that there was no significant change in washout between 1388 h and 1688 h of the AMDT. An acceleration factor of 0 was assigned to 0% residual CeO<sub>2</sub>. An exponential decay curve of the acceleration factor (AF) connected the two points to obtain the theoretical acceleration factors corresponding to the residual CeO<sub>2</sub> content at levels between 0 – 86 % based on the curve equations. The exponential decay of the AF is shown in Figure 7.

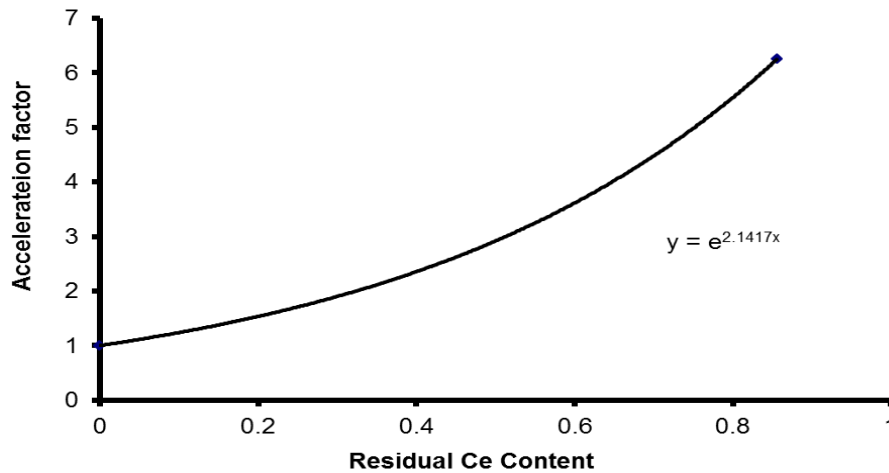


Figure 7. Exponential fit of acceleration factor decay.

The initially predicted stack based bus failure time, without the use of  $\text{CeO}_2$  was used to predict membrane lifetime with  $\text{CeO}_2$ , by matching the point in time when the level of damage seen in membranes is the same without and with the additive. This time is found by calculation the ‘bus life consumed’ for 1,000 hour blocks of bus lifetime, represented by Eq. 31.

$$\text{BusLifeConsumed} = \frac{T_2 - T_1}{AF_{T_2 - T_1}} \quad (31)$$

where  $T_2 - T_1$  corresponds to each 1,000 hour block of bus lifetime with the additive;  $AF_{T_2 - T_1}$  is the AF assigned to a specific residual  $\text{CeO}_2$  content, and 1,000 hour block. The AF normally extends the lifetime, so dividing that specific 1,000 hours by the corresponding AF, results in the lifetime that the membrane would have reached without the additive. The calculated ‘life consumed’ in each time block is consecutively added to the previous ‘life consumed’ until it is equal to the predicted bus life without  $\text{CeO}_2$ . This calculation effectively strips the experimental  $\text{CeO}_2$  lifetime, of the effect of the additive. Stack level bus lifetime and initiation time predictions along with the corresponding lifetime prediction with  $\text{CeO}_2$  are shown in Table 6, where the voltage and temperature

functions used for fitting were the power law and exponential function, respectively. The lifetime predictions based on a CeO<sub>2</sub> washout rate with load cycling, WR<sub>1</sub> and for with a voltage hold, WR<sub>2</sub>, are 32,400 and 46,700 h respectively.

**Table 6. Results of stack level membrane lifetime predictions.**

V	T	Initiation (h)	Lifetime (h)	CeO <sub>2</sub> - WR <sub>1</sub> (h)	CeO <sub>2</sub> - WR <sub>2</sub> (h)
Power	Exponential	10,500	17,500	32,400	46,700

### 5.3. MEA level approach

Significant interactions between factors was found to be present in the case of voltage and temperature. Less significant interactions were found for voltage and oxygen; and temperature and oxygen. The interactions with RH were not found to be significant. Therefore, a comprehensive model that takes these interactions into account is needed for better prediction capabilities. The GLL – Weibull life – stress distribution was used to fit the GA generated initiation and failure times. The EOL time of the stack was used in the case of suspended cells. Maximum likelihood method was used to calculate the parameters of the distribution. The bus lifetime was calculated at a use level of 0.8 V, 58 °C, 21% O<sub>2</sub>, 100% RH, with PITM. 2-sided 95% confidence intervals indicate that the data is within the shown bounds 95% of the time. 5% of the time, the results can be outside the confidence bounds, i.e., outliers. Plots for initiation time results are presented first. GLL - Weibull parameters for initiation time and time at 100 sccm are shown in Table 7.  $\beta$  is the shape parameter,  $\eta$  is the scale parameter,  $\alpha_1$  is parameter B of the Arrhenius relationship used for temperature.  $(-\alpha_2)$  is the inverse power law parameter  $n$  used for voltage, and  $\alpha_3, \alpha_4, \alpha_5$  are the log-linear coefficients for the exponential distribution used for RH, PITM and O<sub>2</sub> concentration. The values of  $\beta$  for

initiation and failure, respectively were, 5.56 and 5.13, indicative of the presence of product wear out, or an increase in failure rate in time.

**Table 7. Parameters of GLL – Weibull distribution.**

	Leak initiation time	Failure time
$\beta$	5.56	5.39
$\alpha(0)$ (h)	36.50	38.17
$\alpha(1)$	-0.07	-0.07
$\alpha(2)$	-5.54	-5.50
$\alpha(3)$	0.79	0.97
$\alpha(4)$	-0.02	-0.02
$\alpha(5)$	0.44	0.50
$\eta$ (h)	19004.340	28703.67
LK Value	-863.52	-687.60

The probability of failure describes the relative likelihood for a random variable, in this case the fuel cell stack lifetime to take on a given value, i.e., to initiate leaks or ‘fail’ at a certain time. The probability of the stack’s predicted lifetime falling within a particular range of values is given by the integral of the stack’s density over that range — that is, it is given by the area under the probability density function but above the horizontal axis and between the lowest and greatest values of the range. The probability density function is nonnegative everywhere, and its integral over the entire space is equal to one. The graphs of the cumulative distribution functions for leak initiation and failure time are shown in Figure 8. The plots of the probability density functions for leak initiation and failure time are shown in Figure 9. The red lines correspond to 95% confidence levels. Using the MEA model B10 is 12,700 h, and 18,900 h for for initiation and failure time, respectively. The mean initiation and failure time is 17,500 h and 26,400, respectively.

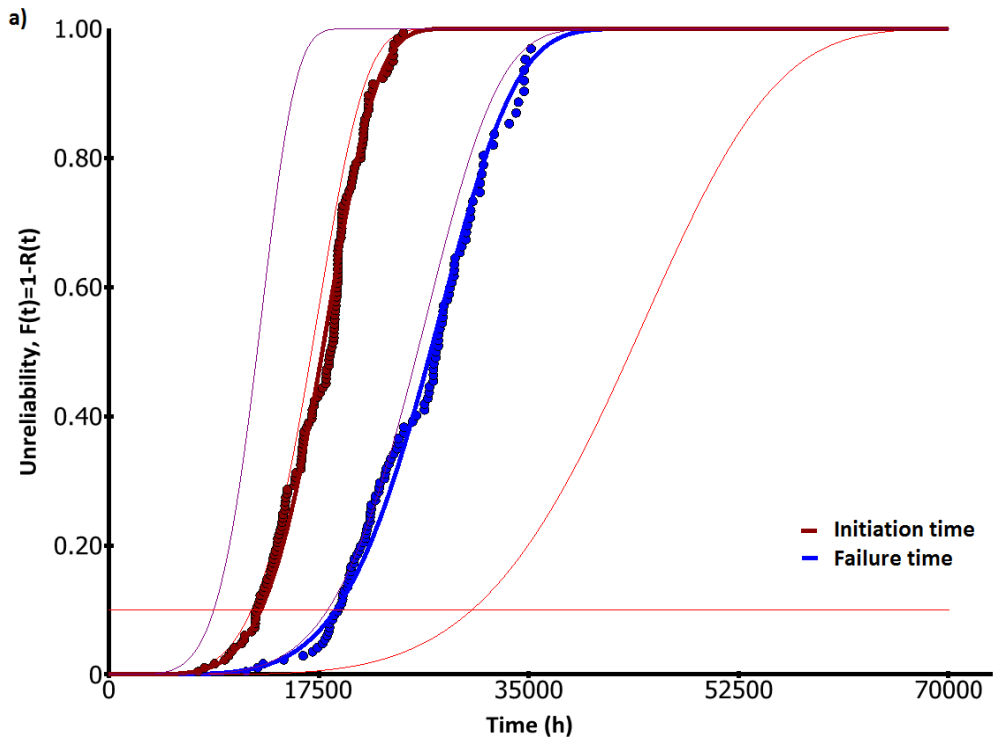


Figure 8. Unreliability vs. initiation and failure time.

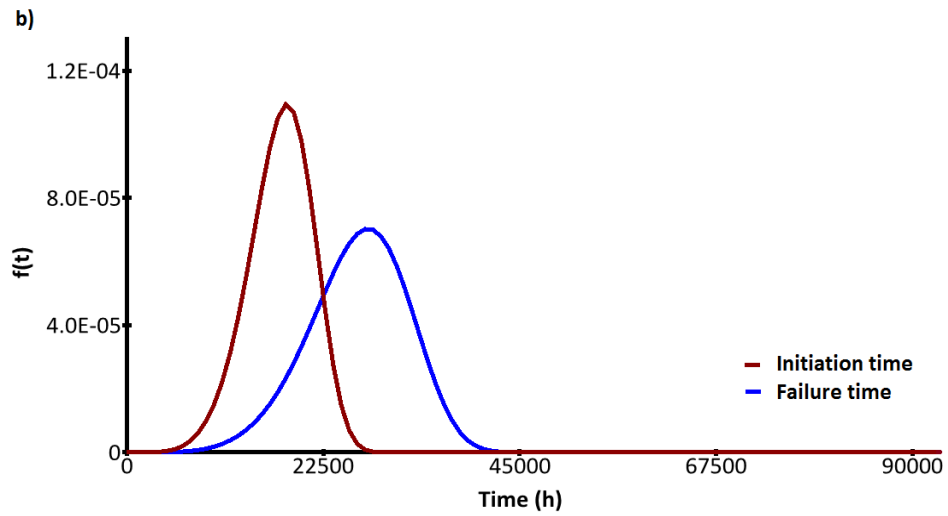


Figure 9. Probability density function plot of initiation and failure time.

## 5.4. Empirical model validation

The Whistler fuel cell bus fleet stopped operation in March 2014 after over three years of operation. Two stacks, Stack A and Stack B were used for validation of the empirical model. Stack A had operated for 9,800 hours, and Stack 6958 had operated for 9,060 hours. The stacks were leak tested using a mechanical air leak test with a dead ended stack at 0.5 barg air pressure. The air based leak was converted to hydrogen by a factor of 1.2, which accounts for a 2x faster H<sub>2</sub> flow, due to viscosity and the overpressure ratio of 0.3/0.5. The air leak rate was compared to the result of the H<sub>2</sub>/N<sub>2</sub> method. The H<sub>2</sub>/N<sub>2</sub> is non-destructive, and provides information on all cells in a closed stack. Hydrogen flows at the anode and nitrogen flows at the cathode. The voltage measured at the cathode corresponds to the amount of hydrogen crossing over to the membrane from the anode through pinholes. Hence the lowest measured voltage at the cathode indicates the presence of the highest amount of hydrogen. An example of the cell voltages measured from the H<sub>2</sub>/N<sub>2</sub> method, which were used to calculate cell flow rate in Stack B is shown in Figure 10. The cells with the lowest voltage are those which have the highest leak rate, due to H<sub>2</sub> leaking through pinholes in the membrane.

The H<sub>2</sub>/N<sub>2</sub> measurement was done at 30 and 60 °C. An overall reduction in the number of leaking cells was observed based on H<sub>2</sub>/N<sub>2</sub> and the sum of leak rates at 30 °C was 2.5 times higher than at 60 °C. This behavior is unexpected as the gas permeation rate through PFSA membranes increases with temperature and saturation. The drop in the measured H<sub>2</sub> flow rate was likely due the membrane swelling at higher temperature, possibly resulting in the sealing of small holes. This is valuable information about the mechanism of membrane hole behaviour during operation in the field, stacks can therefore operate normally with very small pinholes.

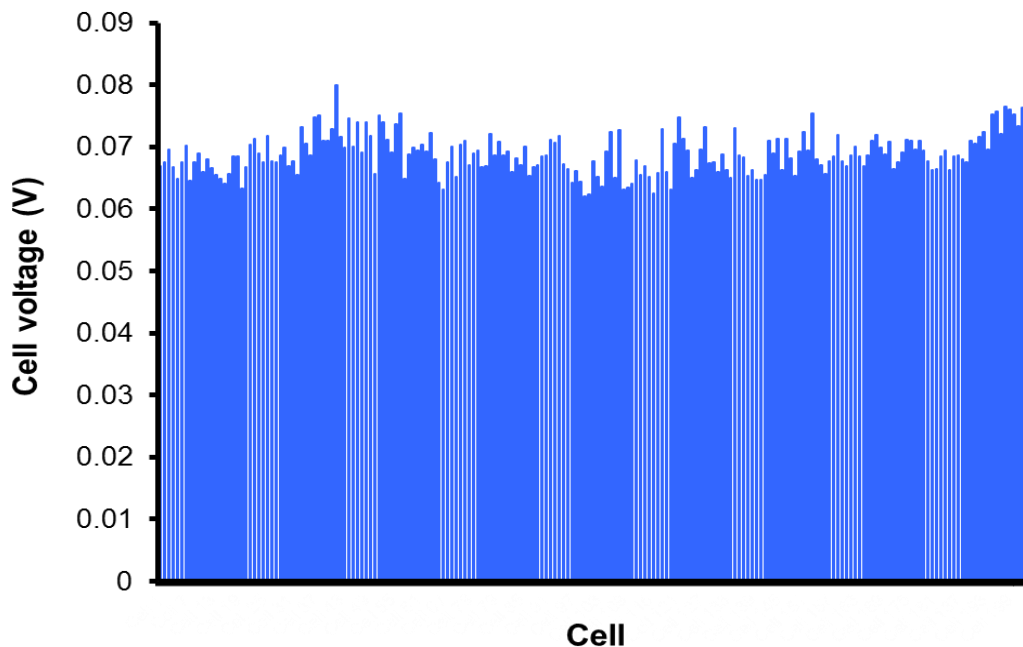


Figure 10. Cell voltages in Stack B during H<sub>2</sub>/N<sub>2</sub> test at 0.3 barg and 30 °C.

The sum of the leak rates of individual cells measured by the H<sub>2</sub>/N<sub>2</sub> at test 30 °C was compared to the result of the mechanical leak test, and the significant discrepancies were identified. The mechanical air leak test on Stack A showed a stack leak rate of 446 sccm, (535 sccm of H<sub>2</sub>), but the sum of the calculated leak rates of individual cells measured by the H<sub>2</sub>/N<sub>2</sub> test was 3,735 sccm of H<sub>2</sub> (1,868 sccm of air). The mechanical air leak test result of Stack B showed a leak of 152 sccm of air (182 sccm of H<sub>2</sub>), but the calculated hydrogen leak rate based on the H<sub>2</sub>/N<sub>2</sub> test was 5,240 sccm of H<sub>2</sub> (2,620 sccm of air). There was clearly an offset that needed to be understood. Further investigation was needed to obtain better results. The hydrogen permeation rate in Nafion membranes is about one order of magnitude higher than that of oxygen. Hence, if the values only represent permeation, then this could possibly explain the discrepancy.

Mechanical leak testing on the bus with air at room temperature results at 30°C were used for validation of the empirical model, since the AMDT stacks were tested at

room temperature. Due to unclear results, 6 MEAs with the highest leak rate calculated based on the  $H_2/N_2$  were extracted from Stack A, and leak tested with a mechanical air leak test at 0.5 barg. The air leak rates were  $3.5 \pm 0.71$  times lower than the calculated amount of  $H_2$  flow based on  $H_2/N_2$ . This is a much higher factor than the factor of 1.2 used to convert air to  $H_2$  meaning that the  $H_2/N_2$  calculation highly overestimates the true amount of the leak rate, which could be a result of the higher permeation rate of  $H_2$  through the membrane compared to  $O_2$ . Nonetheless, it was confirmed that all 6 MEAs were indeed leaking, but with very low leak rates. Only 2 MEAs had leak rates higher than 10 sccm. Furthermore, once the air leak rates were converted from 0.5 barg to 0.3 barg, at which the AMDT stacks are leak tested, the calculated leak rate was  $\sim 7$  times higher, and all MEAs had leak rates under 10 sccm. Only 1 MEA had a leak rate between 9 – 10 sccm. A comparison of the results of the mechanical air leak test at 0.3 and 0.5 barg vs. the  $H_2/N_2$  calculated leak rate is shown in Figure 11.

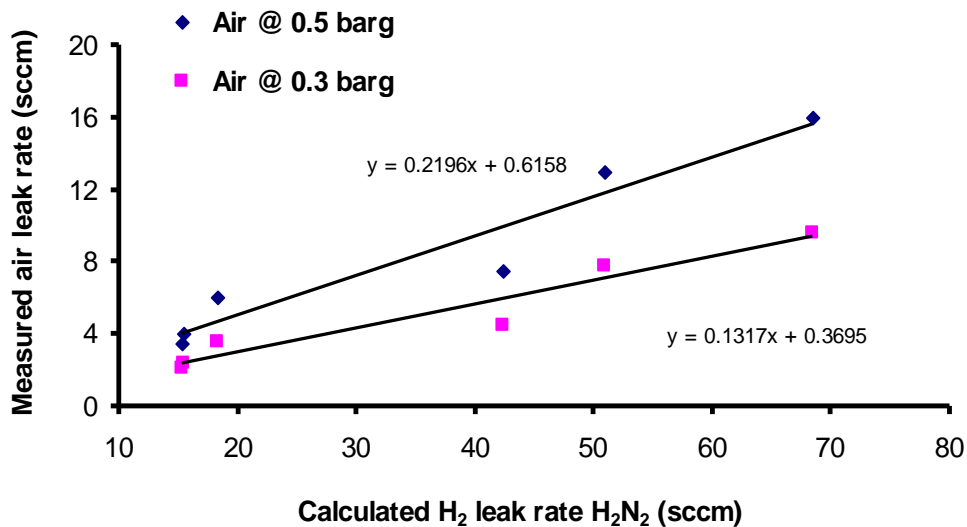


Figure 11. Comparison of predicted vs. measured leak rate of extracted MEAs.

The operating conditions of Stacks A and B were used to predict their lifetime using the stack and MEA empirical models, shown in Table 8. It was concluded that after

9,800 h of operation, 1.5% of the total number of MEAs in Stack A had initiated leak rates smaller than 10 sccm. Thus this can be compared to the B1.5 of the MEA level prediction, which is 8,900 h, where the prediction error is 13%. The stack level prediction for initiation time is 11,100 h, with a 15% prediction error as well. Due to 1 MEA having a leak rate close to 10 sccm, it can be said that 0.25% of the total number of MEAs in Stack A has a leak of 10 sccm. Thus, B0.25 of the MEA level prediction using the lifetime at 10 sccm as the model input predicts that 0.25% of the MEAs will leak with 10 sccm or more after 9,500 h. The error prediction error in this case is 3%.

**Table 8. Empirical stack model results for stacks A and B.**

	Real operating time (h)	Stack level prediction		MEA Level Prediction	
		Initiation time (h)	Lifetime (h)	Initiation time B1.5 (h)	Lifetime B0.25 (h)
Stack A	9,800	11,100	16,080	8,900	9,500
Stack B	9,060	11,250	15,900	8,050	-

Based on these findings, the cells with a calculated leak rate lower than 15 sccm of H<sub>2</sub> were considered to display permeation only. Thus, 13 MEAs in Stack 6198 had leak rates between 1 – 3 sccm, meaning that at 9,600 h, the stack had not yet initiated with leaks that can be used for comparison to the predicted values. These cells have low enough leak rates that this could possibly still be considered permeation, or very early stages of initiation. This could be the reason why the stack level initiation time of 11,250 h predicted for Stack B, based on its operating conditions, has an error of 24%. The MEA level prediction for initiation time is 8,050 h, which has an 11% error.

Membrane degradation is not easily traceable in bus stacks. Stacks can be returned for maintenance due to many reasons. Performance loss is detectable, and is generally attributed to catalyst degradation, but can also indicate membrane degradation. The open circuit voltage drops when H<sub>2</sub> is allowed to leak to the cathode,

and also indicates the presence of pinhole(s). Low performing MEAs, with the largest voltage drops are generally replaced with new MEAs. Pinholes close to the MEA outlet can be sealed with water, and successfully mask their existence for long periods of time. In the case of a pinhole, with the high number of MEAs, reactant recombination and flow sharing complicates precise identification of a faulty MEA. Membrane degradation due to pinhole formation can be confirmed once the MEA is removed from the stack, and leak tested. Thus, membrane degradation is often identified as an additional failure mode. The leaks are generally small and the number of faulty MEAs low. This poses a challenge for detection of leaky cells and in this case model validation. The result shows that based on the failure criteria of the AMDT stack, all investigated bus MEAs, which have operated for over 9,000 h have not yet failed with a leak rate above 10 sccm. Thus at this stage, comparison to the model for membrane initiation time is more appropriate for prediction purposes. The goal was to predict membrane lifetime within 20% of the real lifetime. In this case stack A operated for 9,800 h in the field and 1.5 % of the MEAs are confirmed to have minor leaks under 10 sccm. The stack level prediction of initiation time, and the B1.5 of the MEA level initiation time prediction satisfy this requirement.

## Chapter 6. Conclusions

A comprehensive AMDT experimental design was created and used to support the development of empirical models for heavy duty bus membrane lifetime prediction. The stressors used to accelerate membrane failure due to leak formation through the membrane were elevated voltage, temperature, oxygen concentration and RH cycling. Two promising avenues to extend membrane lifetime were investigated based on Pt in the membrane and CeO<sub>2</sub>. The effect of PITM was studied in detail under AMDT conditions with a sensitivity analysis and TEM imaging of particle structure. Comparisons were made between Pt in field membranes vs. in-situ generated PITM. The significant membrane lifetime extensions observed in the presence of Pt in the membrane were attributed to curly dendritic, tree-like and star shaped Pt particles. AMDT degraded membranes with Pt displayed no global thinning, had low fluoride release, and high mechanical strength. Membrane lifetime with CeO<sub>2</sub> as a radical scavenger was tested under AMDT conditions. CeO<sub>2</sub> coated membranes displayed a 6 fold lifetime extension, after which the membranes were still in a good state of health.

Two empirical model approaches were used to extrapolate membrane lifetime from AMDT conditions to bus conditions. The use level was determined based on observation of Whistler bus operating conditions. The effect of PITM was included in the empirical model, based on similarities of the in-situ generated PITM to Pt in field membranes. The stack based approach predicted an initiation time of 10,500 h and a 17,500 h lifetime for a typical Whistler bus, using the power law for voltage and the exponential function for temperature. A prediction method was proposed for the lifetime of the membrane with CeO<sub>2</sub> based on the Ce washout rate. The Whistler bus membrane lifetime with CeO<sub>2</sub> was predicted to be between 32,100 and 43,600 h, by far exceeding the target lifetime of 20,000 h. The lifetime of individual MEAs was numerically calculated with the help of genetic algorithm. In the MEA approach a failure distribution

was generated for membrane initiation and failure lifetime based on the GLL – Weibull life – stress distribution. The MEA based approach used the individual MEA lifetime, and accounted for suspended MEAs. Model validation was done based on the H<sub>2</sub>/N<sub>2</sub> method, which uses H<sub>2</sub> at the anode and N<sub>2</sub> at the cathode, and measures the H<sub>2</sub> voltage at the cathode. Leak rates of all cells in the stack are calculated based on their H<sub>2</sub> voltage. 6 MEAs were identified with the H<sub>2</sub>/N<sub>2</sub> method to have the highest leak rate, and were extracted from a spare Whistler stack. The cells were confirmed to be leaking, but with much lower leak rates than anticipated, all of which were below 10 sccm, i.e., the MEAs had initiated with minor leaks. It was concluded that after 9,800 h of operation in the field, none of the MEAs had failed with a leak rate above 10 sccm. The corresponding MEA level prediction of 8,900 h, was comparable to the real stack lifetime. The stack based model predicted an initiation time of 11,100 h for the stack, based on its operating conditions in the field. The second stack, which operated for 9,060 h, had not yet developed large enough leaks for proper validation of the prediction method, since there were only a few MEAs with leaks between 1-3 sccm.

In conclusion the proposed lifetime prediction methods were able to predict bus membrane lifetime within  $\pm 20\%$  of the real lifetime based on the proposed empirical models. Both prediction approaches provided results that were very close to the real stack lifetime, with similar precision. However, the individual MEA approach offers a more comprehensive result in the form of a failure distribution.

The empirical model can be improved by adding dynamic stressor effects for RH cycling, or by including the effect of increased degradation over time using cumulative damage or proportional hazard methods. The lifetime prediction with CeO<sub>2</sub> can be made more accurate by including the effect of voltage on the ability of Ce to perform as a radical scavenger. Testing CeO<sub>2</sub> coated MEAs at e.g. 0.8 V, would offer a second dimension to the prediction capabilities of the approach. Future work may also include further optimization of the H<sub>2</sub>/N<sub>2</sub> method in order to achieve more precise results. Thus far, it has proven to be a highly useful technique yielding mainly qualitative results.

## References

- [1] I. EG&G Technical Services, *Fuel Cell Handbook*, Seventh Ed. Morgantown, West Virginia, 2004.
- [2] R. O'Hayre, D. M. Barnett, and F. B. Prinz, "The triple phase boundary - A mathematical model and experimental investigations for fuel cells," *J. Electrochem. Soc.*, vol. 152, pp. A439–A444, 2005.
- [3] W. Vielstich, A. Lamm, and H. A. Gaseiger, "Handbook of Fuel Cells—Fundamentals, Technology and Applications," *Handb. Fuel Cells—Fundamentals, Technol. Appl.*, vol. 3, p. 190, 2003.
- [4] U.S. DOE National Renewable Energy Laboratory, "Fuel Cell Buses in U.S. Transit Fleets: Current Status 2012," 2012. [Online]. Available: [http://www.energy.gov/sites/prod/files/2014/03/f12/fceb\\_status\\_2012.pdf](http://www.energy.gov/sites/prod/files/2014/03/f12/fceb_status_2012.pdf). [Accessed: 08-May-2014].
- [5] M. M. Mench, E. C. Kumbur, T. N. Veziroglu, C. S. Gittleman, F. D. Coms, and Y.-H. Lai, *Polymer Electrolyte Fuel Cell Degradation*. Elsevier, 2012.
- [6] K.-D. Kreuer, A. Rabenau, and W. Weppner, "Vehicle Mechanism, A New Model for the Interpretation of the Conductivity of Fast Proton Conductors," *Angew. Chemie Int. Ed. English*, vol. 21, no. 3, pp. 208–209, Mar. 1982.
- [7] G. A. Ludueña, T. D. Kühne, and D. Sebastiani, "Mixed Grotthuss and Vehicle Transport Mechanism in Proton Conducting Polymers from Ab initio Molecular Dynamics Simulations," *Chem. Mater.*, vol. 23, no. 6, pp. 1424–1429, Mar. 2011.
- [8] J. Larminie and A. Dicks, *Fuel Cell Systems Explained*, vol. 93. 2001.
- [9] E. Planes, L. Flandin, and N. Alberola, "Polymer Composites Bipolar Plates for PEMFCs," *Energy Procedia*, vol. 20, pp. 311–323, 2012.
- [10] U.S. DRIVE Partnership, "Fuel Cell Technical Team Roadmap," 2013.
- [11] U.S.DOE, "Fuel Cell Technologies Program Record:Fuel Cell Bus Targets," 2012.

- [12] T. Hua, R. Ahluwalia, L. Eudy, G. Singer, B. Jermer, N. Asselin-Miller, S. Wessel, T. Patterson, and J. Marcinkoski, "Status of hydrogen fuel cell electric buses worldwide," *J. Power Sources*, vol. 269, pp. 975–993, Dec. 2014.
- [13] "Fuel Cell Bus Demonstration | International Fuel Cell Bus Collaborative." [Online]. Available: <http://www.gofuelcellbus.com/index.php/the-collaborative/all-active-demonstrations/>. [Accessed: 08-May-2015].
- [14] S. Santyapal, "Fuel Cell Technologies Program Overview Fuel Cells," Bethesda, Maryland, 2012.
- [15] "2016 Hyundai Tucson Fuel Cell | Hydrogen-Powered Vehicle | Hyundai." [Online]. Available: <https://www.hyundaiusa.com/tucsonfuelcell/>. [Accessed: 08-May-2015].
- [16] "Toyota Global Site | Fuel Cell Vehicle." [Online]. Available: [http://www.toyota-global.com/innovation/environmental\\_technology/fuelcell\\_vehicle/](http://www.toyota-global.com/innovation/environmental_technology/fuelcell_vehicle/). [Accessed: 08-May-2015].
- [17] X.-Z. Yuan, S. Zhang, H. Wang, J. Wu, J. C. Sun, R. Hiesgen, K. A. Friedrich, M. Schulze, and A. Haug, "Degradation of a polymer exchange membrane fuel cell stack with Nafion® membranes of different thicknesses: Part I. In situ diagnosis," *J. Power Sources*, vol. 195, no. 22, pp. 7594–7599, Nov. 2010.
- [18] D. Liu and S. Case, "Durability study of proton exchange membrane fuel cells under dynamic testing conditions with cyclic current profile | Department of Engineering Science and Mechanics | Virginia Tech," *J. Power Sources*, vol. 162, no. 1, pp. 521–531, 2006.
- [19] M. Miller and A. Bazylak, "A review of polymer electrolyte membrane fuel cell stack testing," *J. Power Sources*, vol. 196, no. 2, pp. 601–613, Jan. 2011.
- [20] R. Borup, J. Meyers, B. Pivovar, Y. S. Kim, R. Mukundan, N. Garland, D. Myers, M. Wilson, F. Garzon, D. Wood, P. Zelenay, K. More, K. Stroh, T. Zawodzinski, J. Boncella, J. E. McGrath, M. Inaba, K. Miyatake, M. Hori, K. Ota, Z. Ogumi, S. Miyata, A. Nishikata, Z. Siroma, Y. Uchimoto, K. Yasuda, K.-I. Kimijima, and N. Iwashita, "Scientific aspects of polymer electrolyte fuel cell durability and degradation.," *Chem. Rev.*, vol. 107, no. 10, pp. 3904–51, Oct. 2007.
- [21] J. Wu, X. Z. Yuan, J. J. Martin, H. Wang, J. Zhang, J. Shen, S. Wu, and W. Merida, "A review of PEM fuel cell durability: Degradation mechanisms and mitigation strategies," *J. Power Sources*, vol. 184, no. 1, pp. 104–119, Sep. 2008.

- [22] Q. Yan, H. Toghiani, Y. W. Lee, K. Liang, and H. Causey, "Effect of sub-freezing temperatures on a PEM fuel cell performance, startup and fuel cell components," *J. Power Sources*, vol. 160, pp. 1242–1250, 2006.
- [23] M. Inaba, T. Kinumoto, M. Kiriake, R. Umabayashi, A. Tasaka, and Z. Ogumi, "Gas crossover and membrane degradation in polymer electrolyte fuel cells," *Electrochim. Acta*, vol. 51, no. 26, pp. 5746–5753, Aug. 2006.
- [24] S. Kundu, M. W. Fowler, L. C. Simon, R. Abouatallah, and N. Beydokhti, "Open circuit voltage durability study and model of catalyst coated membranes at different humidification levels," *J. Power Sources*, vol. 195, no. 21, pp. 7323–7331, Nov. 2010.
- [25] V. A. Sethuraman, J. W. Weidner, A. T. Haug, S. Motupally, and L. V. Protsailo, "Hydrogen Peroxide Formation Rates in a PEMFC Anode and Cathode," *J. Electrochem. Soc.*, vol. 155, no. 1, p. B50, 2008.
- [26] R. M.H. Khorasany, A. Sadeghi Alavijeh, E. Kjeang, G. G. Wang, and R. K. N. D. Rajapakse, "Mechanical degradation of fuel cell membranes under fatigue fracture tests," *J. Power Sources*, vol. 274, pp. 1208–1216, Jan. 2015.
- [27] M. B. Satterfield and J. B. Benziger, "Viscoelastic Properties of Nafion at Elevated Temperature and Humidity," *J. Polym. Sci. Part B Polym. Phys.*, no. October, pp. 11–24, 2008.
- [28] K. Panha, M. Fowler, X.-Z. Yuan, and H. Wang, "Accelerated durability testing via reactants relative humidity cycling on PEM fuel cells," *Appl. Energy*, vol. 93, pp. 90–97, May 2012.
- [29] S. Vengatesan, M. W. Fowler, X.-Z. Yuan, and H. Wang, "Diagnosis of MEA degradation under accelerated relative humidity cycling," *Journal of Power Sources*, vol. 196, no. 11, pp. 5045–5052, Jun-2011.
- [30] F. Barbir, B. Wahdame, D. Candusso, X. François, F. Harel, M.-C. Péra, D. Hissel, and J.-M. Kauffmann, "Comparison between two PEM fuel cell durability tests performed at constant current and under solicitations linked to transport mission profile," *Int. J. Hydrogen Energy*, vol. 32, no. 17, pp. 4523–4536, 2007.
- [31] C. Lim, L. Ghassemzadeh, F. V. Hove, M. Lauritzen, J. Kolodziej, G. Wang, and E. K. S. Holdcroft, "Evolving Membrane Property AST." Vancouver, BC, p. Manuscript, 2013.
- [32] K. Sasaki, M. Shao, and R. Adzic, *Polymer Electrolyte Fuel Cell Durability*. New York, NY: Springer New York, 2009.

- [33] R. M. Darling and J. P. Meyers, "Kinetic Model of Platinum Dissolution in PEMFCs," *J. Electrochem. Soc.*, vol. 150, no. 11, p. A1523, Nov. 2003.
- [34] J. Zhang, B. Litteer, W. Gu, H. Liu, and H. Gasteiger, "Effect of Hydrogen and Oxygen Partial Pressure on Pt Precipitation within the Membrane of PEMFCs," *J. Electrochem. Soc.*, vol. 154, no. 10, p. B1006, 2007.
- [35] D. Zhao, B. L. Yi, H. M. Zhang, and M. Liu, "The effect of platinum in a Nafion membrane on the durability of the membrane under fuel cell conditions," *J. Power Sources*, vol. 195, no. 15, pp. 4606–4612, Aug. 2010.
- [36] M. Aoki, H. Uchida, and M. Watanabe, "Decomposition mechanism of perfluorosulfonic acid electrolyte in polymer electrolyte fuel cells," *Electrochem. commun.*, vol. 8, no. 9, pp. 1509–1513, Sep. 2006.
- [37] N. Macauley, L. Ghassemzadeh, C. Lim, M. Watson, J. Kolodziej, M. Lauritzen, S. Holdcroft, and E. Kjeang, "Pt Band Formation Enhances the Stability of Fuel Cell Membranes," *ECS Electrochem. Lett.*, vol. 2, no. 4, pp. F33–F35, Feb. 2013.
- [38] N. Macauley, A. Sadeghi Alavijeh, M. Watson, J. Kolodziej, M. Lauritzen, S. Knights, G. Wang, and E. Kjeang, "Accelerated Membrane Durability Testing of Heavy Duty Fuel Cells," *J. Electrochem. Soc.*, vol. 162, no. 1, pp. F98–F107, Nov. 2015.
- [39] J. Peron, D. J. Jones, and J. Rozière, "Migration of Platinum under Open Cell Voltage: Effect of the Type of Ionomer Membrane," *ECS Trans.*, vol. 11, no. 1, pp. 1313–1319, 2007.
- [40] Z. Liu, Y. Yang, W. Lü, C. Wang, M. Chen, and Z. Mao, "Durability test of PEMFC with Pt-PFSA composite membrane," *Int. J. Hydrogen Energy*, vol. 37, no. 1, pp. 956–960, Jan. 2012.
- [41] M. P. Rodgers, B. P. Pearman, L. J. Bonville, D. Cullen, N. Mohajeri, and D. K. Slattery, "Evaluation of the Effect of Impregnated Platinum on PFSA Degradation for PEM Fuel Cells," *J. Electrochem. Soc.*, vol. 160, no. 10, pp. F1123–F1128, Aug. 2013.
- [42] M. P. Rodgers, D. A. Cullen, J. Leonard, D. K. Slattery, and J. M. Fenton, "Evaluation of Platinum Band Formation in PEM Fuel Cells," in *Carisma 2012 – 3rd Carisma International Conference*, 2012, pp. 1–19.
- [43] S. Helmlly, R. Hiesgen, T. Morawietz, X.-Z. Yuan, H. Wang, and K. Andreas Friedrich, "Microscopic Investigation of Platinum Deposition in PEMFC Cross-Sections Using AFM and SEM," *J. Electrochem. Soc.*, vol. 160, no. 6, pp. F687–F697, Apr. 2013.

- [44] M. P. Rodgers, L. J. Bonville, and D. K. Slattery, "Evaluation of the durability of polymer electrolyte membranes in fuel cells containing pt/c and pt-co/c catalysts under accelerated testing," *ECS Trans.*, vol. 41, no. 1, pp. 1461–1469, 2011.
- [45] S. Helmly, B. Ohnmacht, R. Hiesgen, E. Gülzow, and K. A. Friedrich, "Influence of Platinum Precipitation on Properties and Degradation of Nafion® Membranes S. Helmly," *ECS Trans.*, vol. 58, no. 1, pp. 969–990, 2013.
- [46] M. Gummalla, V. V. Atrazhev, D. Condit, N. Cipollini, T. Madden, N. Y. Kuzminyh, D. Weiss, and S. F. Burlatsky, "Degradation of Polymer-Electrolyte Membranes in Fuel Cells," *J. Electrochem. Soc.*, vol. 157, no. 11, p. B1542, 2010.
- [47] P. Pei, Q. Chang, and T. Tang, "A quick evaluating method for automotive fuel cell lifetime," *Int. J. Hydrogen Energy*, vol. 33, pp. 3829–3836, 2008.
- [48] P. Pei, "Lifetime Evaluating and the Effects of Operation Conditions on Automotive Fuel Cells," *Chinese Journal of Mechanical Engineering*, vol. 23. p. 66, 2010.
- [49] S. J. Bae, S. J. Kim, J. I. Park, C. W. Park, J. H. Lee, I. Song, N. Lee, K. B. Kim, and J. Y. Park, "Lifetime prediction of a polymer electrolyte membrane fuel cell via an accelerated startup-shutdown cycle test," *Int. J. Hydrogen Energy*, vol. 37, pp. 9775–9781, 2012.
- [50] S. J. Bae, S.-J. Kim, J. I. Park, J.-H. Lee, H. Cho, and J.-Y. Park, "Lifetime prediction through accelerated degradation testing of membrane electrode assemblies in direct methanol fuel cells," *Int. J. Hydrogen Energy*, vol. 35, no. 17, pp. 9166–9176, Sep. 2010.
- [51] R. Onanena, L. Oukhellou, D. Candusso, A. Same, D. Hissel, and P. Aknin, "Estimation of fuel cell operating time for predictive maintenance strategies," *Int. J. Hydrogen Energy*, vol. 35, pp. 8022–8029, 2010.
- [52] US Department of Energy Hydrogen Program, "MEA and Stack Durability for PEM Fuel Cells, Technical Targets," 2007.
- [53] S. F. Burlatsky, M. Gummalla, J. O'Neill, V. V. Atrazhev, A. N. Varyukhin, D. V. Dmitriev, and N. S. Erihman, "A mathematical model for predicting the life of polymer electrolyte fuel cell membranes subjected to hydration cycling," *J. Power Sources*, vol. 215, pp. 135–144, Oct. 2012.
- [54] V. Anghel, "PREDICTION FAILURE FOR PEM FUEL CELLS," *Int. J. Adv. Eng. Technol.*, vol. 4, no. 2, pp. 1–14, 2012.

- [55] "Fuel Cell Perfluorinated Sulfonic Acid Membrane Degradation Correlating Accelerated Stress Testing and Lifetime." [Online]. Available: <http://pubs.acs.org/doi/pdf/10.1021/cr200424d>. [Accessed: 11-Mar-2015].
- [56] Y. Chikashige, Y. Chikyu, K. Miyatake, and M. Watanabe, "Poly(arylene ether) Ionomers Containing Sulfofluorenyl Groups for Fuel Cell Applications," *Macromolecules*, vol. 38, pp. 7121–7126, 2005.
- [57] S. Kreitmeier, P. Lerch, A. Wokaun, and F. N. Buchi, "Local Degradation at Membrane Defects in Polymer Electrolyte Fuel Cells," *J. Electrochem. Soc.*, vol. 160, no. 4, pp. F456–F463, Mar. 2013.
- [58] A. P. Young, J. Stumper, S. Knights, and E. Gyenge, "Ionomer Degradation in Polymer Electrolyte Membrane Fuel Cells," *Journal of The Electrochemical Society*, vol. 157, no. 3. p. B425, 2010.
- [59] T. Ishimoto and M. Koyama, "A Review of Molecular-Level Mechanism of Membrane Degradation in the Polymer Electrolyte Fuel Cell," *Membranes*, vol. 2. pp. 395–414, 2012.
- [60] H. S. Wroblowa and G. Razumney, "Electroreduction of oxygen," *J. Electroanal. Chem. Interfacial Electrochem.*, vol. 69, no. 2, pp. 195–201, Apr. 1976.
- [61] V. Atrazhev, E. Timokhina, S. F. Burlatsky, V. Sultanov, T. Madden, and M. Gummalla, "Direct Mechanism of OH Radicals Formation in PEM Fuel Cells," *ECS Trans.*, vol. 6, pp. 69–74, 2008.
- [62] M. Danilczuk, F. D. Coms, and S. Schlick, "Visualizing chemical reactions and crossover processes in a fuel cell inserted in the ESR resonator: detection by spin trapping of oxygen radicals, nafion-derived fragments, and hydrogen and deuterium atoms.," *J. Phys. Chem. B*, vol. 113, no. 23, pp. 8031–42, Jun. 2009.
- [63] L. Gubler, S. M. Dockheer, and W. H. Koppenol, "Radical (HO●, H● and HOO●) Formation and Ionomer Degradation in Polymer Electrolyte Fuel Cells," *J. Electrochem. Soc.*, vol. 158, no. 7, p. B755, 2011.
- [64] A. Bosnjakovic and S. Schlick, "Nafion Perfluorinated Membranes Treated in Fenton Media: Radical Species Detected by ESR Spectroscopy," *J. Phys. Chem. B*, vol. 108, no. 14, pp. 4332–4337, Apr. 2004.
- [65] L. Ghassemzadeh, K. D. Kreuer, J. Maier, and K. Muller, "Evaluating chemical degradation of proton conducting perfluorosulfonic acid ionomers in a Fenton test by solid-state <sup>19</sup>F NMR spectroscopy," *J. Power Sources*, vol. 196, no. 5, pp. 2490–2497, Mar. 2011.

- [66] T. Ishimoto, R. Nagumo, T. Ogura, T. Ishihara, B. Kim, A. Miyamoto, and M. Koyama, "Chemical Degradation Mechanism of Model Compound,  $\text{CF}_3(\text{CF}_2)_3\text{O}(\text{CF}_2)_2\text{OCF}_2\text{SO}_3\text{H}$ , of PFSA Polymer by Attack of Hydroxyl Radical in PEMFCs," *J. Electrochem. Soc.*, vol. 157, no. 9, p. B1305, 2010.
- [67] A. Pozio, R. F. Silva, M. De Francesco, and L. Giorgi, "Nafion degradation in PEFCs from end plate iron contamination," *Electrochim. Acta*, vol. 48, no. 11, pp. 1543–1549, May 2003.
- [68] E. Endoh, S. Terazono, H. Widjaja, and Y. Takimoto, "Degradation Study of MEA for PEMFCs under Low Humidity Conditions," *Electrochem. Solid-State Lett.*, vol. 7, no. 7, p. A209, 2004.
- [69] V. O. Mittal, H. Russell Kunz, and J. M. Fenton, "Is  $\text{H}_2\text{O}_2$  Involved in the Membrane Degradation Mechanism in PEMFC?," *Electrochem. Solid-State Lett.*, vol. 9, no. 6, p. A299, 2006.
- [70] V. O. Mittal, H. R. Kunz, and J. M. Fenton, "Membrane Degradation Mechanisms in PEMFCs," *J. Electrochem. Soc.*, vol. 154, no. 7, p. B652, 2007.
- [71] K. H. Wong and E. Kjeang, "Mitigation of chemical membrane degradation in fuel cells: understanding the effect of cell voltage and iron ion redox cycle.," *ChemSusChem*, vol. 8, no. 6, pp. 1072–82, Mar. 2015.
- [72] L. Ghassemzadeh and S. Holdcroft, "Quantifying the Structural Changes of Perfluorosulfonated Acid Ionomer upon Reaction with Hydroxyl Radicals.," *J. Am. Chem. Soc.*, vol. 135, no. 22, pp. 8181–8184, 2013.
- [73] Ghassemzadeh, Lida, T. J. Peckham, T. Weissbach, X. Luo, and S. Holdcroft, "Selective Formation of Hydrogen and Hydroxyl Radicals by Electron Beam Irradiation and Their Reactivity with Perfluorosulfonated Acid Ionomer," *J. Am. Chem. Soc.*, vol. 135, no. 42, pp. 15923–15932, 2013.
- [74] H. Uchida, Y. Ueno, H. Hagihara, and M. Watanabe, "Self-humidifying electrolyte membranes for fuel cells - Preparation of highly dispersed  $\text{TiO}_2$  particles in Nafion 112," *J. Electrochem. Soc.*, vol. 150, pp. A57–A62, 2003.
- [75] M. V. Williams, H. R. Kunz, and J. M. Fenton, "Operation of Nafion®-based PEM fuel cells with no external humidification: influence of operating conditions and gas diffusion layers," *J. Power Sources*, vol. 135, no. 1–2, pp. 122–134, Sep. 2004.
- [76] J. St-Pierre, D. P. Wilkinsoin, S. Knights, and M. Bos, "Relationships between water management, contamination and lifetime degradation in PEFC," *J. New Mater. Electrochem. Syst.*, vol. 3, pp. 99–106, 2000.

- [77] S. Zhang, X. Yuan, H. Wang, W. Merida, H. Zhu, J. Shen, S. Wu, and J. Zhang, "A review of accelerated stress tests of MEA durability in PEM fuel cells," *Int. J. Hydrogen Energy*, vol. 34, no. 1, pp. 388–404, Jan. 2009.
- [78] F. N. Büchi and S. Srinivasan, "Operating Proton Exchange Membrane Fuel Cells Without External Humidification of the Reactant Gases Fundamental Aspects," *J. Electrochem. Soc.*, vol. 144, no. 8, pp. 2767–2772, 1997.
- [79] U.S. Department of Energy Hydrogen Program, *Enabling Commercial PEM Fuel Cells with Breakthrough Lifetime Improvements*. 2004.
- [80] B. P. Pearman, "Florida Solar Energy Center," in *2012 Fuel Cell Seminar & Exposition*, 2012.
- [81] L. Gubler and W. H. Koppenol, "Kinetic Simulation of the Chemical Stabilization Mechanism in Fuel Cell Membranes Using Cerium and Manganese Redox Couples," *J. Electrochem. Soc.*, vol. 159, no. 2, p. B211, 2012.
- [82] Y. P. Patil, W. L. Jarrett, and K. a. Mauritz, "Deterioration of mechanical properties: A cause for fuel cell membrane failure," *J. Memb. Sci.*, vol. 356, no. 1–2, pp. 7–13, Jul. 2010.
- [83] R. M. H. Khorasany, A. Sadeghi Alavijeh, E. Kjeang, G. G. Wang, and R. K. N. D. Rajapakse, "Mechanical degradation of fuel cell membranes under fatigue fracture tests," *J. Power Sources*, Oct. 2014.
- [84] R. M. H. Khorasany, M.-A. Goulet, A. Sadeghi Alavijeh, E. Kjeang, G. G. Wang, and R. K. N. D. Rajapakse, "On the constitutive relations for catalyst coated membrane applied to in-situ fuel cell modeling," *J. Power Sources*, vol. 252, pp. 176–188, Apr. 2014.
- [85] H. Tang, S. Peikang, S. P. Jiang, F. Wang, and M. Pan, "A degradation study of Nafion proton exchange membrane of PEM fuel cells," *J Power Sources*, vol. 170, no. 1, pp. 85–92, Jun. 2007.
- [86] M.-A. Goulet, R. M. H. Khorasany, C. De Torres, M. Lauritzen, E. Kjeang, G. G. Wang, and N. Rajapakse, "Mechanical properties of catalyst coated membranes for fuel cells," *J. Power Sources*, vol. 234, pp. 38–47, Jul. 2013.
- [87] V. Stanic and M. Hoberecht, "Mechanism of pinhole formation in membrane electrode assemblies for pem fuel cells."
- [88] M. A. R. S. Al-Baghdadi, "Modeling optimizes PEM fuel cell durability using threedimensional multi-phase computational fluid dynamics model," *Int. J. Energy Environ.*, vol. 1, no. 3, pp. 375–398, 2010.

- [89] P. Genova-Dimitrova, B. Baradie, D. Foscallo, C. Poinsignon, and J. Y. Sanchez, "Ionomeric membranes for proton exchange membrane fuel cell (PEMFC): Sulfonated polysulfone associated with phosphatoantimonic acid," *J. Memb. Sci.*, vol. 185, pp. 59–71, 2001.
- [90] X. Huang, R. Solasi, Y. Zou, M. Feshler, K. Reifsnider, D. Condit, S. Burlatsky, and T. Madden, "Mechanical Endurance of Polymer Electrolyte Membrane and PEM Fuel Cell Durability," *J. Polym. Sci. Part B Polym. Phys.*, vol. 44, no. 16, pp. 2346–2357, 2006.
- [91] S. Subianto, M. Pica, M. Casciola, P. Cojocar, L. Merlo, G. Hards, and D. J. Jones, "Physical and chemical modification routes leading to improved mechanical properties of perfluorosulfonic acid membranes for PEM fuel cells," *J. Power Sources*, vol. 233, pp. 216–230, Jul. 2013.
- [92] X. Huang, R. Solasi, Y. Zou, M. Feshler, K. Reifsnider, D. Condit, S. Burlatsky, and T. Madden, "Mechanical endurance of polymer electrolyte membrane and PEM fuel cell durability," *J. Polym. Sci. Part B Polym. Phys.*, vol. 44, no. 16, pp. 2346–2357, Aug. 2006.
- [93] C. Lim, L. Ghassemzadeh, F. Van Hove, M. Lauritzen, J. Kolodziej, G. G. Wang, S. Holdcroft, and E. Kjeang, "Membrane degradation during combined chemical and mechanical accelerated stress testing of PEM fuel cells," *J. Power Sources*, vol. 257, pp. 102–110, Feb. 2014.
- [94] A. Sadeghi Alavijeh, M. A. Goulet, R. M. H. Khorasany, J. Ghataurah, C. Lim, M. Lauritzen, E. Kjeang, G. G. Wang, and R. K. N. D. Rajapakse, "No Title," *Fuel Cells*, 2014.
- [95] W. Gu, R. N. Carter, P. T. Yu, and H. Gasteiger, "Start/Stop and Local H<sub>2</sub> Starvation Mechanisms of Carbon Corrosion: Model vs. Experiment," *ECS Trans.*, vol. 11, no. 1, pp. 963–973, 2007.
- [96] F. N. Büchi, M. Inaba, and T. J. Schmidt, *Polymer Electrolyte Fuel Cell Durability*. New York, NY: Springer New York, 2009.
- [97] S. Kreitmeier, A. Wokaun, and F. N. Büchi, "Local Catalyst Support Degradation during Polymer Electrolyte Fuel Cell Start-Up and Shutdown," *J. Electrochem. Soc.*, vol. 159, no. 11, pp. F787–F793, Sep. 2012.
- [98] W. Bi and T. F. Fuller, "Temperature Effects on PEM Fuel Cells Pt/C Catalyst Degradation," *J. Electrochem. Soc.*, vol. 155, no. 2, p. B215, 2008.

- [99] C. A. Reiser, L. Bregoli, T. W. Patterson, J. S. Yi, J. D. Yang, M. L. Perry, and T. D. Jarvi, "A Reverse-Current Decay Mechanism for Fuel Cells," *Electrochem. Solid-State Lett.*, vol. 8, no. 6, p. A273, Jun. 2005.
- [100] V. Atrazhev, S. F. Burlatsky, N. E. Cipollini, D. A. Condit, and N. Erikhman, "Aspects of PEMFC Degradation," *ECS Trans.*, vol. 1, no. 8, pp. 239–246, 2006.
- [101] S. F. Burlatsky, M. Gummalla, V. V. Atrazhev, D. V. Dmitriev, N. Y. Kuzminyh, and N. S. Erikhman, "The Dynamics of Platinum Precipitation in an Ion Exchange Membrane," *J. Electrochem. Soc.*, vol. 158, no. 3, p. B322, 2011.
- [102] S. Takaichi, H. Uchida, and M. Watanabe, "Distribution profile of hydrogen and oxygen permeating in polymer electrolyte membrane measured by mixed potential," *Electrochem. commun.*, vol. 9, no. 8, pp. 1975–1979, 2007.
- [103] J. B. Kerr, G. Liu, and X. Sun, "New Polyelectrolyte Materials for High-Temperature Fuel Cells, Membrane Electrode Assemblies and Enhanced Selectivity," *Prog. Rep. - DOE Hydrog. Progr.*, pp. 366–372, 2004.
- [104] A. Z. Weber, "Gas-Crossover and Membrane-Pinhole Effects in Polymer-Electrolyte Fuel Cells," *J. Electrochem. Soc.*, vol. 155, no. 6, p. B521, 2008.
- [105] "Computer- and Web-Based Training for Manufacturing Quality/Productivity Improvement." [Online]. Available: [http://www.qualitytrainingportal.com/resources/doe/doe\\_types.htm](http://www.qualitytrainingportal.com/resources/doe/doe_types.htm). [Accessed: 02-May-2015].
- [106] D. C. Montgomery, *Design and Analysis of Experiments: Douglas C. Montgomery*, 8 edition. Wiley, 2012.
- [107] "e-Handbook of Statistical Methods," 2003. [Online]. Available: <http://www.itl.nist.gov/div898/handbook/pri/section3/pri33a.htm>.
- [108] C. Lim, A. Sadeghi Alavijeh, M. Lauritzen, J. Kolodziej, S. Knights, and E. Kjeang, "Fuel Cell Durability Enhancement with Cerium Oxide under Combined Chemical and Mechanical Membrane Degradation," *ECS Electrochem. Lett.*, vol. 4, no. 4, pp. F29–F31, Feb. 2015.
- [109] J. Fimrite, B. Carnes, H. Struchtrup, and N. Djilaliz, "Transport Phenomena in Polymer Electrolyte Membranes II. Binary Friction Membrane Model," *J. Electrochem. Soc.*, vol. 152, no. 9, pp. A1815–A1823, 2005.
- [110] T. E. Springer, T. A. Zawodzinski, and S. Gottesfeld, "Polymer Electrolyte Fuel Cell Model," *J. Electrochem. Soc.*, vol. 138, no. 8, pp. 2334–2342, 1991.

- [111] N. Macauley, K. H. Wong, M. Watson, and E. Kjeang, "Effect of Platinum in the Membrane on Fuel Cell Membrane Durability," Vancouver, BC, 2015.
- [112] ReliaSoft Corporation, *Accelerated Life Testing Data Analysis Reference*. 2015.
- [113] A. M. Niroumand, O. Pooyanfar, N. Macauley, J. DeVaal, and F. Golnaraghi, "In-situ diagnostic tools for hydrogen transfer leak characterization in PEM fuel cell stacks part I: R&D applications," *J. Power Sources*, vol. 278, pp. 652–659, Mar. 2015.

# **Appendix A**

**Pt band formation enhances the stability of fuel cell membranes**



## Pt Band Formation Enhances the Stability of Fuel Cell Membranes

N. Macauley,<sup>a</sup> L. Ghassemzadeh,<sup>b</sup> C. Lim,<sup>a</sup> M. Watson,<sup>c</sup> J. Kolodziej,<sup>c</sup> M. Lauritzen,<sup>c,\*</sup>  
 S. Holdcroft,<sup>b</sup> and E. Kjeang<sup>a,\*,z</sup>

<sup>a</sup>School of Engineering Science, Simon Fraser University, Surrey, British Columbia V3T0A3, Canada

<sup>b</sup>Department of Chemistry, Simon Fraser University, Burnaby, British Columbia V5A1S6, Canada

<sup>c</sup>Ballard Power Systems, Burnaby, British Columbia V5J5J8, Canada

Enhancing the durability of fuel cells for the transportation sector requires a better understanding of the fundamental processes that cause degradation. Field-operated PEMFCs have been shown to develop a thin parallel band of Pt inside the membrane. Reports on the effect of the Pt band on membrane durability are contradictory. Here, we examined the influence of the Pt band by performing in situ and ex situ membrane degradation tests. We report that the Pt band significantly decreases the rate of membrane degradation, thereby enhancing its longevity.

© 2013 The Electrochemical Society. [DOI: 10.1149/2.007304eel] All rights reserved.

Manuscript submitted January 17, 2013; revised manuscript received January 28, 2013. Published February 5, 2013.

Polymer electrolyte membrane (PEM) fuel cell technology is promising for zero-emission transportation, but lowering cost and improving durability remain challenges for widespread commercialization. The membrane-electrode-assembly (MEA), which consists of a polymer electrolyte membrane, catalyst layers, and gas diffusion layers, is prone to degradation under automotive fuel cell duty cycles consisting of rapid potential cycling, changes in temperature, changes in humidity, and start-up/shut-down events. Degradation of the polymer electrolyte membrane can be attributed to both chemical attack and mechanical stressors. It is believed oxidative radicals generated during fuel cell operation are the main source of chemical degradation of the polymer, leading to changes of the membranes' polymer structure.<sup>1</sup> These radicals may form as a result of decomposition of hydrogen peroxide formed during the ORR or from crossover of the gaseous reactants and reaction at the anode and cathode. Conditions such as low humidity, high temperature, and high cell voltage have been reported to increase the concentration of H<sub>2</sub>O<sub>2</sub> in the cell, thereby accelerating chemical degradation.<sup>2-4</sup> Moreover, swelling and shrinking of the membrane through changes in water content during fuel cell operation increases internal stress on the membrane and exacerbates degradation due to fatigue, pinhole, and/or crack formation.<sup>5,6</sup> Over the last decade, different strategies have been proposed to improve the durability of PEMs. These include removing transition metal impurities, chemical stabilization of the polymer ends, use of inorganic oxides, redesigning the side chain to reduce the number of ether bonds, and mechanical reinforcement.<sup>7-10</sup> The approach is to decrease the propensity of radical attack and reduce mechanical stresses during operational cycling.

Membrane-electrode assemblies that have been extricated from long term, field-operated fuel cells have been shown to develop a thin parallel band of Pt inside the membrane. It is reported that Pt originally located in the cathode catalyst layer dissolves during voltage cycling and re-deposits inside the membrane,<sup>11-14</sup> promoted by the highly acidic fuel cell environment at voltages above 0.9 V.<sup>15,16</sup> Pt ions that migrate toward the anode are reduced by hydrogen crossing from the anode.<sup>17</sup> The precise location of the band is determined by the flux of hydrogen permeating the PEM as well as the position in the membrane where the cathode potential abruptly decreases.<sup>12,18</sup> The effect of the Pt band on membrane degradation is intensely debated in the scientific community: On one hand it is speculated that the Pt band promotes radical formation, thereby accelerating membrane degradation,<sup>18-22</sup> while others suggest that the Pt band enhances the durability of the membrane by decomposing hydrogen peroxide to water and oxygen.<sup>21,23,24</sup>

The objective of the present work is to experimentally determine whether Pt band formation has a negative or positive effect on membrane durability and lifetime during automotive fuel cell operation.

The work makes use of MEAs removed from heavy duty fuel cells deployed by Ballard Power Systems in transit buses, for which Pt band formation is present.

In order to analyze the effect of the Pt band on membrane durability, an accelerated stress test (AST) protocol, developed specifically for rapid membrane degradation, was employed to evaluate the durability of the field-operated MEAs compared to freshly manufactured MEAs, produced under similar conditions using the same components, but clearly without the Pt band present. The AST applies chemical and mechanical stress in an alternating pattern, which is repeated until membrane failure is obtained. An AST cycle features a 10 h open circuit voltage (OCV) phase at 95°C and 56% relative humidity (RH) with 40% O<sub>2</sub> at the cathode and 100% H<sub>2</sub> at the anode, followed by five consecutive blocks of 10 min wet/20 min dry cycling in N<sub>2</sub> at 75°C.<sup>25</sup> The AST stack consists of five 45 cm<sup>2</sup> MEAs.

The field-operated MEA samples utilized in this study were extracted from a Ballard heavy duty fuel cell stack subjected to transit bus operation for 2800 hours. The aged MEAs were used without modification to their components and were solely divided into several smaller units (45 cm<sup>2</sup>) to fit the lab hardware. Scanning electron microscope (SEM) images captured before and after field operation confirmed that the thickness of the membrane remained constant; with the only notable difference between fresh MEAs and field-operated MEAs being the formation of a Pt band (Figure 1).

When exposed to AST cycling, surprisingly, the field-operated MEAs lasted longer (16 AST cycles) than fresh MEAs (13 AST cycles). Periodic monitoring of the OCV and an in-situ electrochemical leak test (ELT) were used to track the overall health of the membranes after each AST cycle. The H<sub>2</sub> transfer leak rate was qualitatively diagnosed by measuring the OCV before and after applying a small H<sub>2</sub> overpressure in a pure H<sub>2</sub>/air (anode/cathode) condition. As there is no external current flow during OCV, voltage drops due to ohmic and mass transport losses are negligible. The ELT therefore quantifies the amount of H<sub>2</sub> leakage across the membrane using the OCV change

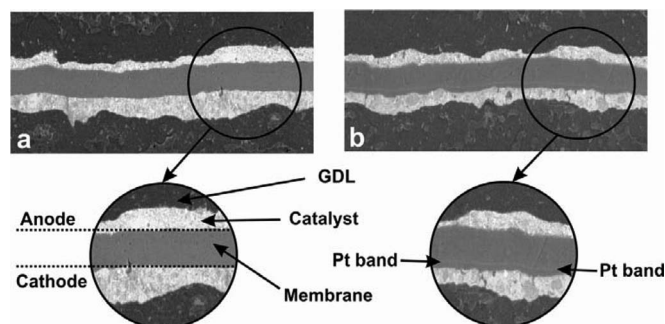
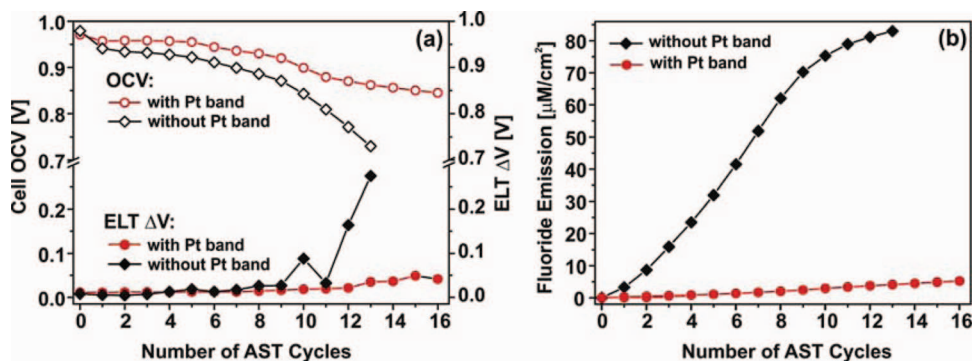


Figure 1. SEM images of (a) fresh MEA and (b) field-operated MEA.

\*Electrochemical Society Active Member.

<sup>z</sup>E-mail: ekjeang@sfu.ca



**Figure 2.** (a) OCV and electrochemical leak test (ELT), and (b) fluoride emission as a function of AST-cycles for fresh MEAs (without Pt band) and field-operated MEAs (with Pt band). ELT indicates  $\text{H}_2$  crossover.

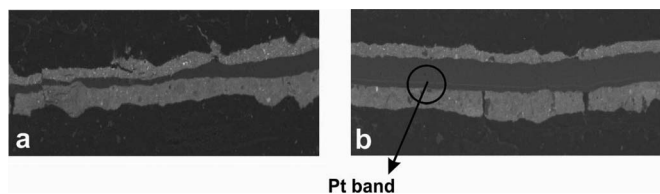


**Figure 3.** SEM images of (a) fresh MEA and (b) field-operated MEA samples after 13 and 16 AST cycles, respectively.

( $\Delta V$ ) as an indicator, whereby a higher  $\Delta V$  indicates a higher level of crossover. A  $\Delta V$  of 40 mV per cell is deemed catastrophic failure and represents facile  $\text{H}_2$  crossover through pinholes and cracks. Figure 2a shows a steep decay of OCV accompanied by a high average gas transfer leak rate indicative of membrane failure for the freshly manufactured MEAs without a Pt band. In contrast, the field-operated MEAs maintain a relatively high OCV and show a significantly lower average transfer leakage. To estimate the degree of chemical membrane degradation during the AST, the fluoride ion emission rates were measured after each AST cycle, as shown in Figure 2b. The final fluoride emission rate of the field-operated MEAs was one order of magnitude lower than the fluoride emission rate of the fresh MEAs, showing resilience to chemical degradation. Although the field-operated MEA was still in good condition after 2800 hours, it experienced some degree of electrocatalyst degradation, and it is possible that the rate of  $\text{H}_2\text{O}_2$  generation in the catalyst layer(s) was reduced due to loss of electrochemically active carbon, the presence of which is known to promote formation of  $\text{H}_2\text{O}_2$ . However, minor catalyst layer degradation cannot account for the order-of-magnitude reduction in fluoride release rate, which must be predominantly an effect of the Pt band in the membrane.

Cross-sectional SEM images of the post mortem MEAs are shown in Figure 3. The micrographs revealed severe global membrane thinning of 43% on average in the case of the fresh MEAs, due to loss of polymer material. No signs of membrane thinning were observed for the field-operated MEA, neither after 2800 hours of field operation nor after subsequent exposure to the AST conditions. The SEM images also confirmed the presence of a Pt band close to the cathode in the membrane of the field-operated MEA.

The results suggest that the presence of the Pt band helps mitigate further chemical degradation of the membrane. To examine this, ex situ degradation of a fresh PFSA membrane was initiated by its immersion into a Fenton's reagent (20 vol%  $\text{H}_2\text{O}_2$ , 10 ppm  $\text{Fe}^{2+}$ ) at  $80^\circ\text{C}$ , which provides a source of hydroxyl and hydroperoxyl radicals. The experiment lasted 48 h during which the membranes were thoroughly washed in 1 M  $\text{H}_2\text{SO}_4$  at  $80^\circ\text{C}$  and deionized water every 12 h when changing the solution. The ion exchange capacity (IEC) and proton conductivity ( $\sigma$ ) of the membrane was measured by electrochemical impedance spectroscopy at room temperature and 100% RH every 12 h. The experiment was repeated under identical conditions but with 5 ppm Pt black dispersed in the solution.

Figure 4 illustrates the decrease in IEC and  $\sigma$  during exposure to Fenton's reagent, resulting from attack of hydroxyl and hydroperoxyl radicals on the polymer structure, and loss of acidic groups. The presence of Pt black substantially reduces the rate of decrease of IEC and  $\sigma$ . It is common knowledge that Pt catalyzes the decomposition of  $\text{H}_2\text{O}_2$  directly to oxygen and water, and by inference, reduces the concentration of reactive hydroxyl and hydroperoxyl radicals. After 48 h these membranes remained physically strong and visually unchanged. In the absence of Pt the membranes became brittle, mechanically fragile, and developed pinholes. The next logical sequence of experiments would be to deposit a Pt band into fresh membranes in order to examine its role in stabilizing membranes in Fenton's reagent. We have yet to be successful in preparing materials that simulate field-operated membranes.

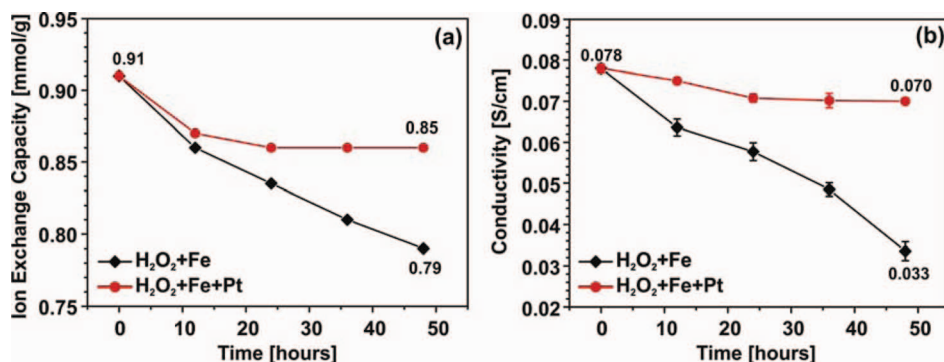


**Figure 4.** (a) IEC and (b) proton conductivity of the membrane, as a function of treatment with Fenton's reagent, with and without 5 ppm Pt black present.

### Acknowledgments

Funding for this research provided by Automotive Partnership Canada (APC), Ballard Power Systems, and Simon Fraser University is highly appreciated. We acknowledge Curtis Allen, Fred Van Hove, and Trevor Engh for experimental assistance and Ballard Power Systems for providing field-operated MEA samples.

### References

1. M. Danilczuk, F. D. Coms, and S. Schlick, *Journal of Physical Chemistry B*, **113**, 8031 (2009).
2. J. F. Wu, X. Z. Yuan, J. J. Martin, H. J. Wang, J. J. Zhang, J. Shen, S. H. Wu, and W. Merida, *Journal of Power Sources*, **184**, 104 (2008).
3. F. A. de Bruijn, V. A. T. Dam, and G. J. M. Janssen, *Fuel Cells*, **8**, 3 (2008).
4. M. P. Rodgers, L. J. Bonville, H. R. Kunz, D. K. Slattery, and J. M. Fenton, *Chemical Reviews*, **112**, 6075 (2012).
5. M. Ji and Z. Wei, *Energies*, **2**, 1057 (2009).
6. X. Huang, R. Solasi, Y. Zou, M. Feshler, K. Reifsnider, D. Condit, S. Burlatsky, and T. Madden, *Journal of Polymer Science Part B: Polymer Physics*, **44**, 2346 (2006).
7. A. K. Mishra, S. Bose, T. Kuila, N. H. Kim, and J. H. Lee, *Progress in Polymer Science*, **37**, 842 (2012).
8. D. E. Curtin, R. D. Lousenberg, T. J. Henry, P. C. Tangeman, and M. E. Tisack, *Journal of Power Sources*, **131**, 41 (2004).
9. L. Merlo, A. Ghielmi, L. Cirillo, M. Gebert, and V. Arcella, *Journal of Power Sources*, **171**, 140 (2007).
10. M. Danilczuk, A. J. Perkowski, and S. Schlick, *Macromolecules*, **43**, 3352 (2010).
11. R. M. Darling and J. P. Meyers, *Journal of the Electrochemical Society*, **152**, A242 (2005).
12. J. Xie, D. L. Wood, K. L. More, P. Atanassov, and R. L. Borup, *Journal Of The Electrochemical Society*, **152**, A1011 (2005).
13. K. Yasuda, A. Taniguchi, T. Akita, T. Ioroi, and Z. Siroma, *Physical Chemistry Chemical Physics*, **8**, 746 (2006).
14. T. Akita, A. Taniguchi, J. Maekawa, Z. Siroma, K. Tanaka, M. Kohyama, and K. Yasuda, *Journal of Power Sources*, **159**, 461 (2006).
15. X. Wang, R. Kumar, and D. J. Myers, *Electrochemical and Solid-State Letters*, **9**, A225 (2006).
16. R. L. Borup, J. R. Davey, F. H. Garzon, D. L. Wood, and M. A. Inbody, *Journal of Power Sources*, **163**, 76 (2006).
17. W. Bi, G. E. Gray, and T. F. Fuller, *Electrochemical and Solid-State Letters*, **10**, B101 (2007).
18. S. F. Burlatsky, V. Atrazhev, N. Cipollini, D. Condit, and N. Erikhman, *ECS Transactions*, **1**, 239 (2006).
19. V. V. Atrazhev, N. S. Erikhman, and S. F. Burlatsky, *Journal of Electroanalytical Chemistry*, **601**, 251 (2007).
20. D. Zhao, B. L. Yi, H. M. Zhang, and M. Liu, *Journal of Power Sources*, **195**, 4606 (2010).
21. M. Aoki, H. Uchida, and M. Watanabe, *Electrochemistry Communications*, **7**, 1434 (2005).
22. S. Stucki, G. G. Scherer, S. Schlagowski, and E. Fischer, *Journal of Applied Electrochemistry*, **28**, 1041 (1998).
23. M. Aoki, H. Uchida, and M. Watanabe, *Electrochemistry Communications*, **8**, 1509 (2006).
24. H. Hagihara, H. Uchida, and M. Watanabe, *Electrochimica Acta*, **51**, 3979 (2006).
25. E. Kjeang, C. Lim, L. Ghassemzadeh, N. Macauley, A. Tavassoli, R. Khorasany, M. A. Goulet, J. To, S. Diprose, M. Cruickshank, F. Feng, G. Wang, N. Rajapakse, S. Holdcroft, M. Lauritzen, J. Kolodziej, M. Watson, and S. Knights, presented in part at the ISE Conference, 19-24 August, 2012.

# **Appendix B**

## **Accelerated membrane durability testing of heavy duty fuel cells**



## Accelerated Membrane Durability Testing of Heavy Duty Fuel Cells

Natalia Macauley,<sup>a,\*</sup> Alireza Sadeghi Alavijeh,<sup>a</sup> Mark Watson,<sup>b</sup> Joanna Kolodziej,<sup>b</sup> Michael Lauritzen,<sup>b,\*\*</sup> Shanna Knights,<sup>b,\*\*</sup> Gary Wang,<sup>a</sup> and Erik Kjeang<sup>a,\*\*,z</sup>

<sup>a</sup>School of Mechatronic Systems Engineering, Simon Fraser University, Surrey, British Columbia V3T0A3, Canada

<sup>b</sup>Ballard Power Systems, Burnaby, British Columbia V5J5J8, Canada

Regular durability testing of heavy duty fuel cell systems for transit bus application requires several thousand hours of operation, which is costly and time consuming. Alternatively, accelerated durability tests are able to generate failure modes observed in field operation in a compressed time period, by applying enhanced levels of stress. The objective of the present work is to design and validate an accelerated membrane durability test (AMDT) for heavy duty fuel cells under bus related conditions. The proposed AMDT generates bus relevant membrane failure modes in a few hundred hours, which is more than an order of magnitude faster than for regular duty cycle testing. Elevated voltage, temperature, and oxidant levels are used to accelerate membrane chemical stress, while relative humidity (RH) cycling is used to induce mechanical stress. RH cycling is found to significantly reduce membrane life-time compared to constant RH conditions. The role of a platinum band in the membrane is investigated and membranes with Pt bands demonstrate a considerable life-time extension under AMDT conditions, with minimal membrane degradation. Overall, this research serves to establish a benchmark AMDT that can rapidly and reliably evaluate membrane stability under simulated heavy duty fuel cell conditions.

© The Author(s) 2014. Published by ECS. This is an open access article distributed under the terms of the Creative Commons Attribution Non-Commercial No Derivatives 4.0 License (CC BY-NC-ND, <http://creativecommons.org/licenses/by-nc-nd/4.0/>), which permits non-commercial reuse, distribution, and reproduction in any medium, provided the original work is not changed in any way and is properly cited. For permission for commercial reuse, please email: [oa@electrochem.org](mailto:oa@electrochem.org). [DOI: 10.1149/2.0671501jes] All rights reserved.

Manuscript submitted September 5, 2014; revised manuscript received November 5, 2014. Published November 19, 2014.

According to the World Health Organization, air pollution claimed seven million lives around the world in 2012.<sup>1</sup> A major portion of this pollution was caused by road vehicles. Due to their zero emission operation, fuel cell buses offer a solution to air pollution in urban areas. Heavy duty fuel cell powered bus fleets in London, Hamburg, Cologne, Oslo, Whistler, and California are displaying long-term stability and durability in the field. A 2016 power plant life-time target of 18,000 hours was set for transit buses by the United States Department of Energy.<sup>2</sup> Lab testing of fuel cell bus components and systems for such extensive periods of time is not feasible due to the high cost and long time involved. Therefore, major fuel cell developers turn to accelerated durability tests (ADTs) to estimate the durability of fuel cell systems and their components.

The membrane is a key component of fuel cells and is vital for fuel cell durability and performance. There are two main degradation mechanisms of perfluorosulfonic acid (PFSA) ionomer membranes under fuel cell operation:<sup>3</sup> chemical and mechanical degradation. Chemical degradation of the membrane is caused by radical attack. Hydroxyl (HO•), hydroperoxyl (HOO•), and hydrogen (H•) radicals have been identified as potentially harmful to the membrane.<sup>4</sup> Radicals can form in the catalyst layers or as a result of hydrogen peroxide decomposition in the presence of Fenton's reagents in the membrane.<sup>5-9</sup> Hydrogen peroxide forms electrochemically as a by-product of the oxygen reduction reaction (ORR) and chemically when crossover oxygen and hydrogen meet at the cathode or anode.<sup>10-12</sup> Polymer side chain degradation in chemically stabilized PFSA membranes is predominantly due to HO• radical attack on the first ether bond in the  $\alpha$ -OCF<sub>2</sub>- group.<sup>13</sup> Attack by H• may occur to a smaller extent at the tertiary carbon C-F bond on both the main and side chains, while attack by HO• occurs solely on the side chain.<sup>14</sup> Cell voltages close to the open circuit voltage (OCV) are known to lead to high levels of chemical degradation, resulting in a gradual loss of membrane material, observed as general membrane thinning and fluoride release in the effluent water.<sup>15</sup> Adequate humidification of the membrane is crucial for membrane durability, since fuel cell operation at dry conditions leads to increased membrane degradation.<sup>16,17</sup> Chemical stabilization of PFSA polymer end groups<sup>18</sup> and use of additives, such

as cerium and manganese radical scavengers are potential methods to mitigate chemical degradation.<sup>19,20</sup> Chemical membrane degradation has a strong impact on mechanical membrane properties<sup>21</sup> due to molecular weight reduction.

The resulting mechanical stress from frequent swelling and shrinking of the constrained membrane in response to changes in water content results in membrane creep, fatigue,<sup>22</sup> and the formation of pinholes, cracks, and tears on the surface or in the bulk of the membrane.<sup>23</sup> Membrane stiffness and strength was found to decrease when exposed to humidity cycling at high temperatures.<sup>22,24-28</sup> The mechanical endurance of membranes can be enhanced by physical reinforcement of the membrane using a porous polymer matrix, fibers, or inorganic reinforcement.<sup>29</sup>

Coupled chemical and mechanical stressors have however been found to exacerbate membrane degradation compared to chemical and mechanical degradation applied separately.<sup>30-33</sup> The impact of combined chemical and mechanical degradation on membrane durability was investigated in our group under Ballard Power Systems' cyclic open circuit voltage (COCV) AST protocol.<sup>34</sup> Results of mechanical testing showed a rapid reduction in CCM ductility and fracture strain together with a significant decrease in ultimate tensile strength (UTS) as a function of AST cycles.<sup>35</sup> During combined chemical and mechanical membrane degradation, mechanical stress can affect chemically weak regions of the membrane first, since they tend to be the least resistant to humidity changes and therefore more prone to damage. The failure modes of combined chemical and mechanical membrane degradation include localized membrane thinning (divots), pinholes with rough edges, tears, and microcracks.

The effect of platinum in the membrane on membrane durability is subject to debate. Platinum is known to be unstable at high voltages, and can hence dissolve, migrate out of the catalyst layer, and deposit in the membrane.<sup>36,37</sup> The partial pressure of crossover H<sub>2</sub> from the anode is relevant for Pt band formation, because H<sub>2</sub> reduces Pt ions to form metallic Pt in the membrane.<sup>38</sup> The location of the Pt band is determined by the local mixed potential distribution.<sup>39-42</sup> Many authors believe that Pt in the membrane increases membrane degradation.<sup>43-47</sup> Synthetic methods of planting Pt in the membrane have been shown to have a detrimental effect on the membrane,<sup>48,49</sup> where platinum ions can act as a Fenton's reaction promoter.<sup>50,51</sup> However, in our group, field operated MEAs with a naturally grown metallic Pt band in the membrane were tested under COCV AST conditions,

\*Electrochemical Society Student Member.

\*\*Electrochemical Society Active Member.

<sup>z</sup>E-mail: [ekjeang@sfu.ca](mailto:ekjeang@sfu.ca)

and vastly outperformed freshly manufactured membranes in terms of durability.<sup>52</sup>

The objective of the present work is to develop an Accelerated Membrane Durability Test (AMDT) protocol for heavy duty fuel cells based on the characteristic duty cycle of transit buses. In contrast to generalized screening methods such as the COCV AST, the proposed AMDT conditions are much milder, yielding more realistic application oriented results, in this case for heavy duty bus fuel cells. Due to its close resemblance to bus conditions, the AMDT will provide an accurate evaluation of membrane stability for fuel cell bus operation. Additionally, the role of humidity cycling and platinum in the membrane will be investigated under AMDT conditions. This work is expected to aid the fundamental understanding of membrane degradation under fuel cell bus conditions.

## Experimental

**Membrane electrode assembly (MEA) fabrication.**—Catalyzed gas diffusion electrodes (GDEs) were fabricated by coating a microporous layer made of polytetrafluoroethylene (PTFE) and carbon black on a non-woven carbon paper gas diffusion layer substrate, followed by coating a catalyst layer consisting of carbon-supported platinum catalyst and perfluorosulfonic acid ionomer.<sup>53</sup> MEAs were prepared by hot-pressing a standard non-reinforced PFSA ionomer membrane with anode and cathode GDEs.

**Stack assembly and test station.**—MEAs were used to build a 10 cell stack with graphitic bipolar plates having co-flow parallel straight channels. A pressurized bladder ensured uniform compression between MEAs and bipolar plates. External and internal gas leak tests were done before installation of the stack on a test station. AMDTs were run on Ballard Power Systems' fully automated standard test hardware. The stack was conditioned for 24 hours prior to the AMDT in order to equilibrate the membranes. The proposed AMDT test conditions are described in the following section.

### Accelerated Membrane Durability Test (AMDT)

**Baseline AMDT protocol.**—Since the 2010 Winter Olympics, 20 fuel cell transit buses powered by Ballard HD6 modules operated in Whistler Resort Community in British Columbia, Canada for four years. This was the largest fuel cell hybrid bus fleet in the world, which successfully endured temperatures between  $-12^{\circ}\text{C}$  to  $27^{\circ}\text{C}$ , snowfall from November to May, and a very challenging terrain with frequent up and down hill driving. The development of the AMDT for heavy duty fuel cell vehicles is based on a thorough characterization of the Whistler HD6 duty cycle for key stressors, their levels, and occurrence. The protocol uses constant and time dependent bus fuel cell stressors at elevated levels. All stressor levels were carefully chosen to avoid failure mode artifacts.

Buses often idle at traffic lights, stop signs, or bus stops, leading to extended periods at elevated voltage, which is known to chemically degrade the membrane. The baseline AMDT therefore applies chemical stress by maintaining the stack voltage at 9 V, simulating bus idling conditions. Due to regular acceleration and deceleration, transit buses have a highly dynamic duty cycle, which results in frequent humidity fluctuations. In the Whistler fleet, the humidity mildly dropped during acceleration and then quickly returned back to a fully saturated state once the level of demanded load was reduced. The amplitude of changes in humidity was smaller than 10% RH and short in duration, meaning that the membrane may not have experienced excessive swelling or shrinking, although its repetitive nature could eventually cause mechanical degradation over time. The baseline AMDT achieves RH cycling by bypassing the cathode humidifier for 66 seconds every 10 minutes, causing the RH to gradually dip to approximately 60% RH at the cathode. The total membrane RH during the dry cycle is estimated to drop to 80% RH, since the anode remains fully humidified, still generating more aggressive fluctuations in RH than in the bus. The ratio of the membrane resistivity measured

during the wet and dry cycle was used to estimate the RH during the dry cycle, based on the corresponding conductivity and water content levels known for 100% RH.<sup>54,55</sup>

Idling and changes in humidity naturally occur in close proximity during driving. Therefore the baseline AMDT uses chemical and mechanical stressors simultaneously, simulating the real bus operating conditions. Additionally, elevated temperature and oxygen concentration are known to increase the rates of both chemical and mechanical membrane degradation processes without altering the failure modes. Buses generally use oxygen from the air in the surrounding environment as oxidant, which contains 21% oxygen. Increased oxygen availability allows for increased formation of radicals. To ensure rapid membrane failure the temperature and oxygen partial pressure used in the AMDT are  $85^{\circ}\text{C}$  and 45%, respectively, which are both elevated compared to bus conditions. Hydrogen and oxygen are used as reactant gases at flow rates of 5 and 10 slpm, respectively. These flows are intentionally high, considering the low load of only  $\sim 1\text{A}$ , in order to ensure complete MEA surface coverage and avoid the formation of regions deficient of reactants. The backpressure is set to 0.1 barg, but generally fluctuates by around 0.03 barg during the test.

**Complementary AMDT protocols.**—Complementary tests with certain adjustments to the baseline AMDT protocol were designed to investigate the state of degradation at leak initiation and the effects of RH cycling and platinum in the membrane (PITM) on membrane durability. The temperature and oxidant levels were kept at  $85^{\circ}\text{C}$  and 45%  $\text{O}_2$ , respectively, in all complementary testing. The early stage of membrane degradation was investigated in the initiation test, which applied the baseline AMDT conditions until initial hydrogen leaks across the membrane were detected by means of increased voltage fluctuation. Tests at 90% and 100% constant RH were performed to better understand the effect of RH cycling. The life-time difference between the tests at constant RH and the baseline AMDT is due to RH cycling, which is included in the baseline AMDT. The effect of PITM was studied using membranes with an artificially deposited Pt band tested under baseline AMDT conditions. Tests with PITM are considered to be more realistic, since a Pt band forms in membranes under bus operating conditions. The tests with PITM used a proprietary Ballard protocol to generate a Pt band in the membrane either before or during the baseline AMDT operation. The first test denoted by PITM-1 used Pt band generation prior to exposing the modified membranes to baseline AMDT conditions. The second test denoted by PITM-2 integrated the Pt band generation into the baseline AMDT protocol by running one Pt band generating cycle after every 6<sup>th</sup> RH cycle of the baseline AMDT. The baseline and complementary AMDT conditions are summarized in Table I.

### Diagnostic Methods

External and internal gas leak tests were performed every 48 hours to assess the membrane condition. The stack was considered failed at an internal leak rate of 100 sccm, corresponding to the limiting leak rate through the membrane of 10 sccm per cell suggested by the US Department of Energy.<sup>56</sup> After failure, the stack was disassembled followed by individual MEA leak test and analysis under an Infra-Red camera (Kaiser RTI T620 FLIR) to identify the approximate location and size of leaks. In the IR camera test, hydrogen was supplied under a firmly fixed MEA in a custom fixture and reacted with oxygen from

**Table I. Summary of the AMDT runs and obtained life-times.**

AMDT Name	Condition	Pt band protocol	Life-time (h)
<b>Baseline</b>	Baseline	-	298
<b>Initiation</b>	Baseline	-	131
<b>90% RH</b>	90% RH	-	497
<b>100% RH</b>	100% RH	-	643
<b>PITM-1</b>	Baseline	Prior to AMDT	405
<b>PITM-2</b>	Baseline	Integrated in AMDT	662

air when allowed to leak through holes in the membrane. The resulting heat generation was captured by the IR camera.

The least and most damaged MEAs were further inspected by a Philips XL30 scanning electron microscope (SEM). Samples were prepared by casting MEAs in epoxy pucks, which were polished in a Struers TegraPol-11 polisher with 120–1200 grit silicon carbide paper, and then carbon coated with an Edwards Scancoat Six Sputter Coater. Micrographs were taken using a backscatter detector at 20 kV. The membrane thickness was measured in 12 different spots and the morphology of transfers was found in cross-sectional and surface images. Membrane thinning was considered present when the final membrane thickness was below three standard deviations of the initial thickness. The fluoride concentration was measured from effluent water and the total fluoride loss was calculated using a method described elsewhere.<sup>34</sup>

**Ex-situ mechanical testing.**— Ex-situ mechanical testing was done on the beginning-of-life (BOL) and AMDT degraded membranes. Tensile tests were used to compare the mechanical properties of samples degraded by combined chemical and mechanical degradation (baseline AMDT), isolated chemical degradation (constant RH), and in the presence of PITM. To ensure consistency, MEAs were cut into rectangular shapes (25 × 2 mm) along the transverse direction using a plotter cutter machine. The gas diffusion layers (GDLs) were removed from the MEA and the remaining CCM was stored between glass slides at ambient conditions to keep the samples straight before testing. Tensile tests were conducted using a dynamic mechanical analyzer (TA Instruments Q800 DMA) equipped with an environmental chamber (TA Instruments DMA-RH accessory). Tensile test samples were loaded with a 5:1 gauge length to width aspect ratio to prevent introduction of edge stress concentration.<sup>24</sup> The rest of the sample length was gripped by lower and upper clamps. The average membrane width and thickness was measured using an optical microscope for all samples and SEM for representative samples, respectively. The exact sample gauge length was measured by the DMA prior to the tensile test initiation. After equilibration at the desired conditions, tensile tests were conducted at room conditions (23°C and 50% RH) and fuel cell conditions (70°C and 90% RH) at a low strain rate (0.01 min<sup>-1</sup>) on BOL and AMDT degraded samples. The tensile test was continued until it either reached mechanical failure or the DMA maximum clamp travel length of around 26 mm (160% total elongation). The elastic modulus, ultimate tensile strength (UTS), and final strain were calculated from the stress – strain curves. The elastic modulus was determined from the maximum slope of a 5<sup>th</sup> order polynomial fit to the initial section between 0 and 0.5% strain.<sup>24</sup> The UTS and final strain were calculated as the maximum tensile stress and total strain (elastic and plastic) tolerated by the CCM during the tensile test, respectively. Under each environmental condition and AMDT type, the average and standard deviation of three repetitive tests were calculated. The error bars on the curves represent ±2σ, which statistically covers 95% of inputs.

## Results and Discussion

In order to accelerate membrane degradation, the baseline AMDT applied combined chemical and mechanical stress by using high voltage, temperature, oxygen concentration, and RH cycling. As a result, the life-time of membranes subjected to the baseline AMDT was reduced by more than an order of magnitude compared to real bus operating conditions. In contrast, the AMDT life-time was approximately twice as long as the average life-time obtained with the more aggressive COCV AST.<sup>34</sup> Since the AMDT conditions were designed to closely resemble actual operating conditions, it successfully generated failure modes similar to those found under bus conditions. As expected there was a correlation between AMDT conditions and the length of the membrane life-time. RH cycling significantly reduced membrane life-time compared to constant RH conditions. A lower constant RH level also resulted in reduced membrane life-time compared to fully humidified conditions. PITM was found to visibly prolong membrane life-time under baseline AMDT conditions. A

summary of the obtained membrane life-times at baseline conditions vs. complementary AMDT conditions is shown in Table 1.

The baseline AMDT failed at 298 h due to coupled chemical-mechanical stress. In the absence of humidity cycling, the 90% and 100% constant RH AMDTs degraded the membrane in a purely chemical manner, resulting in longer membrane life-times than the baseline, 497 h and 643 h, respectively. This demonstrates that combined chemical and mechanical stress indeed enhances membrane degradation, not only by adding mechanical stress, but also due to the short periods of increased chemical degradation at low RH during the dry cycle. The difference in membrane life-time between the two tests at constant RH is evidence of a higher rate of chemical membrane degradation at lower RH due to increased rates of gas crossover and hydrogen peroxide formation,<sup>38,57–59</sup> and thereby increased radical formation via Fenton's reaction. Although it is known that the membrane gas permeability decreases at lower RH,<sup>10</sup> there is a counteracting effect whereby the oxygen concentration increases due to the reduced water vapor pressure at a fixed absolute pressure. In the present case, the water vapor pressure at 85°C is 0.58 bar at 100% RH and 0.52 bar at 90% RH. With a 45% oxygen concentration in the dry gas, the oxygen partial pressures at 100% and 90% RH are 0.25 and 0.27 bar, respectively, which represents an 11% increase at 90% RH. Membrane permeability depends on the gas diffusion coefficient, which changes with humidity. By lowering the RH from 100% to 90%, the oxygen diffusion coefficient decreases by around 7%.<sup>60</sup> Therefore, the effect of increased oxygen partial pressure dominates over the effect of reduced permeability by roughly 4%, which actually leads to increased oxygen crossover to the anode. Mechanical stress during RH cycling appears to have gradually exacerbated the effect of chemical degradation,<sup>30</sup> causing chemically weak areas of the membrane to become more vulnerable to tearing and cracking. The presence of a Pt band in the membrane showed significant life enhancing effects on membrane durability by vastly outperforming the baseline AMDT by lasting 405 h and 662 h with the two PITM application methods, offering evidence that Pt in the membrane is capable of mitigating membrane degradation.

**Hydrogen leaks and voltage decay.**— Membrane holes were allowed to grow until the stack leak rate reached or exceeded 100 sccm in all AMDTs, except for the initiation AMDT, which was stopped at 131 h, when the first indicators of membrane damage occurred. Indicators of membrane damage include increased voltage fluctuations and voltage decay. The morphological changes present in the membrane prior to hole growth, which is mainly a thermal process, were studied in order to better understand the initial degradation process.

Each test displayed different membrane leak rate development characteristics over time, as shown in Figure 1. The baseline showed

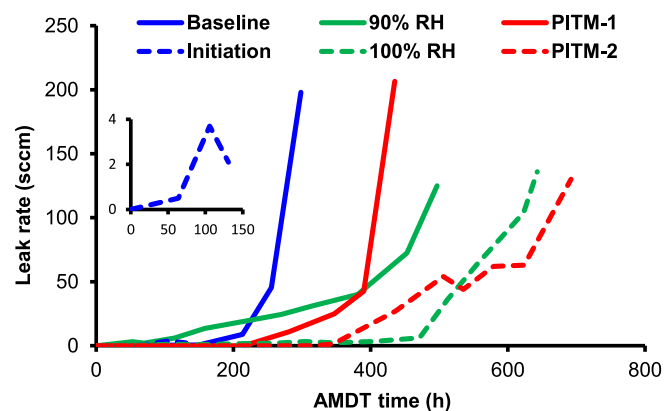


**Figure 1.** Hydrogen leak rate development during AMDT operation, showing slower leak growth at constant RH (green) and with PITM (red), compared to baseline (blue full). The initiation test (blue dashed) was stopped after leak initiation, in order to investigate the early stage of degradation.

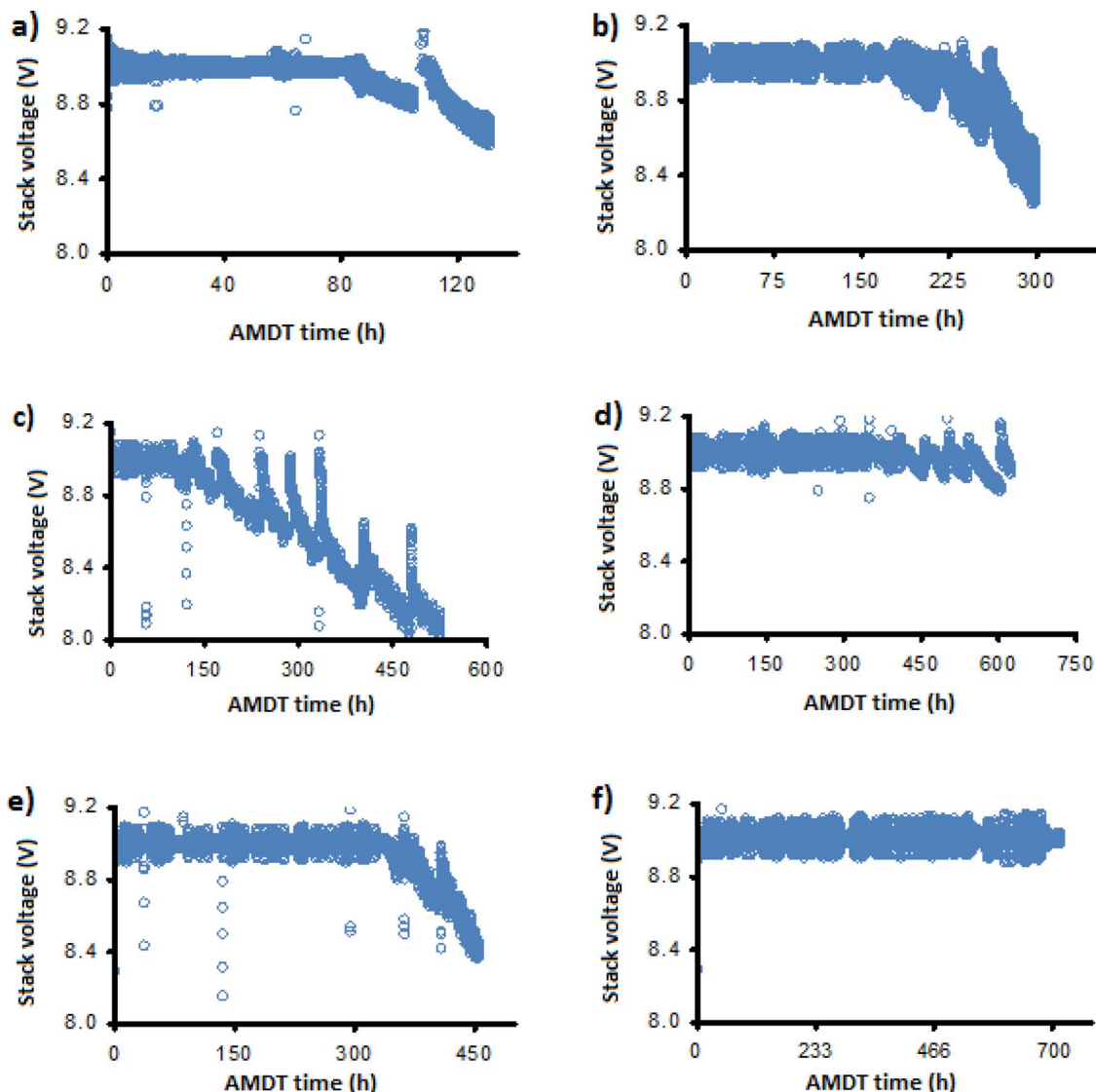


**Figure 2.** Voltage fluctuations and voltage decay of the various AMDT runs: a) initiation; b) baseline; c) 90% RH; d) 100% RH; e) PITM-1; and f) PITM-2.

short initiation and leak growth times. Chemically degrading conditions at 90% constant RH may have resulted in a shorter initiation time, but allowed for a relatively long leak growth time, eventually exceeding the baseline life-time. The 100% constant RH test had the mildest conditions, and as expected, displayed longer initiation and leak growth periods compared to the baseline and 90% RH runs. This pattern suggests the action of mechanical stress due to RH cycling as an accelerator for membrane rupture and leak growth. The initiation and leak growth periods of the tests with PITM resemble those of the constant RH tests, despite being exposed to baseline AMDT conditions, including RH cycling. The longer leak growth times at constant RH and with PITM confirm that MEAs are able to operate for a relatively long time despite the presence of small leaks, when the conditions are favorable;<sup>59</sup> i.e., low mechanical stress in the case of constant RH and low chemical stress in the case of PITM.

The initiation AMDT was stopped at 131 h (Figure 1, insert) when the stack first started to exhibit increased voltage fluctuations and voltage decay, as shown in Figure 2. The initial voltage fluctuations in the beginning of the test may be due to different permeation rates of hydrogen through the healthy membranes during RH cycling. However, after the formation of leaks, the convective hydrogen flux to the cathode results in mixed potentials at the cathode, causing an increase in the amplitude of fluctuations, and the onset of voltage decay.

The formation and growth of new transfers over time resulted in further voltage drops, which can be correlated to the measured leak rate development seen in Figure 1. The baseline, for instance, exhibits a major voltage drop around 200 h in Figure 2b, which can be seen as the final largest increase in leak rate in Figure 1. The initiation, baseline, and PITM-1 voltages dropped significantly from 9.0 V to around 8.6, 8.3, and 8.4 V, respectively. The 90% RH had the most severe final voltage drop, reaching 8.0 V. On the other hand, the 100% RH voltage and PITM-2 stayed mostly above 8.8 and 8.9 V, pointing to a very small amount of MEAs with holes, which was later confirmed.

Similarly, open circuit voltage (OCV) decay is related to hydrogen leaks caused by membrane degradation and is therefore a good indicator of membrane health. The OCV can also drop due to increased hydrogen crossover rates through local regions of thinned membrane. The measured OCV results are provided in Figure 3 for the various AMDT runs.

The OCV decay curve can be separated into two parts. The first part represents the initiation time with a lower decay rate and the second part represents the leak growth phase with a much faster decay rate. As expected, the initiation and baseline AMDTs showed the fastest OCV decay, due to rapid leak formation and growth, causing all 10 cells to develop fairly large leaks in both cases. Interestingly, the 90% RH test showed an equally rapid decay rate as the first part

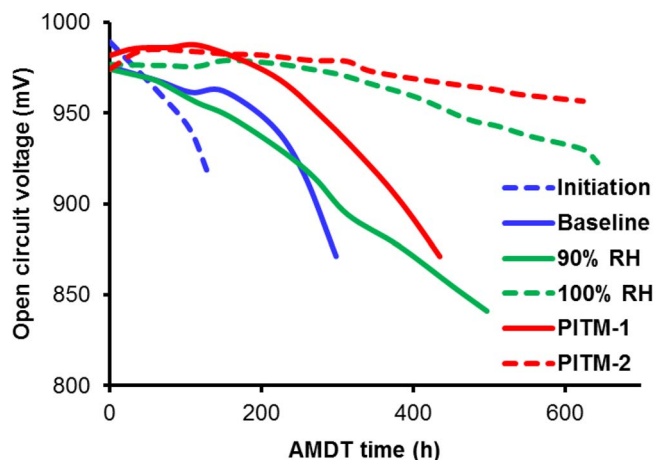


**Figure 3.** Open circuit cell voltage decay during AMDT operation, which is primarily a consequence of hydrogen leaks across the membranes.

of the baseline, indicating a similar level of membrane degradation to the baseline, suggesting that the initial phase of the baseline is dominated by chemical degradation. In later stages however, the effect of RH cycling gradually increased the degradation rate toward early

failure for the baseline, while the 90% RH degradation rate remained constant during the entire testing period. At a later point in time the 90% RH OCV drop exceeded the OCV drop of the baseline, and similarly, all 10 cells were found to have developed leaks. The 100% RH test showed no signs of OCV decay in the first phase, in good agreement with its long initiation time, but once 3 out of 10 membranes developed leaks, the OCV decay rate mildly increased. The PITM tests experienced the lowest level of OCV decay rates and OCV drops, corresponding to long initiation times and few damaged cells. PITM-1 had 6 leaky membranes out of 10, while PITM-2 had only 2 leaky membranes despite having the longest test duration. This is a powerful indicator of the ability of the PITM to mitigate and reduce chemical degradation and thereby substantially extend the membrane stability and life-time.<sup>52</sup>

*Performance loss.*— The performance of the AMDT stacks was periodically monitored by measuring polarization curves. Beginning of Life (BOL), Middle of Life (MOL), and End of Life (EOL) polarization curves are shown in Figure 4. The OCV decay observed here is consistent with the previous findings. The decay of the fuel cell performance is correlated to membrane degradation and observed consistently across all current densities. This decay can be attributed to increasing activation losses at MOL and EOL due to convective hydrogen crossover flux through the membrane.<sup>34</sup> The voltage losses at non-zero current densities were however lower than at OCV; for

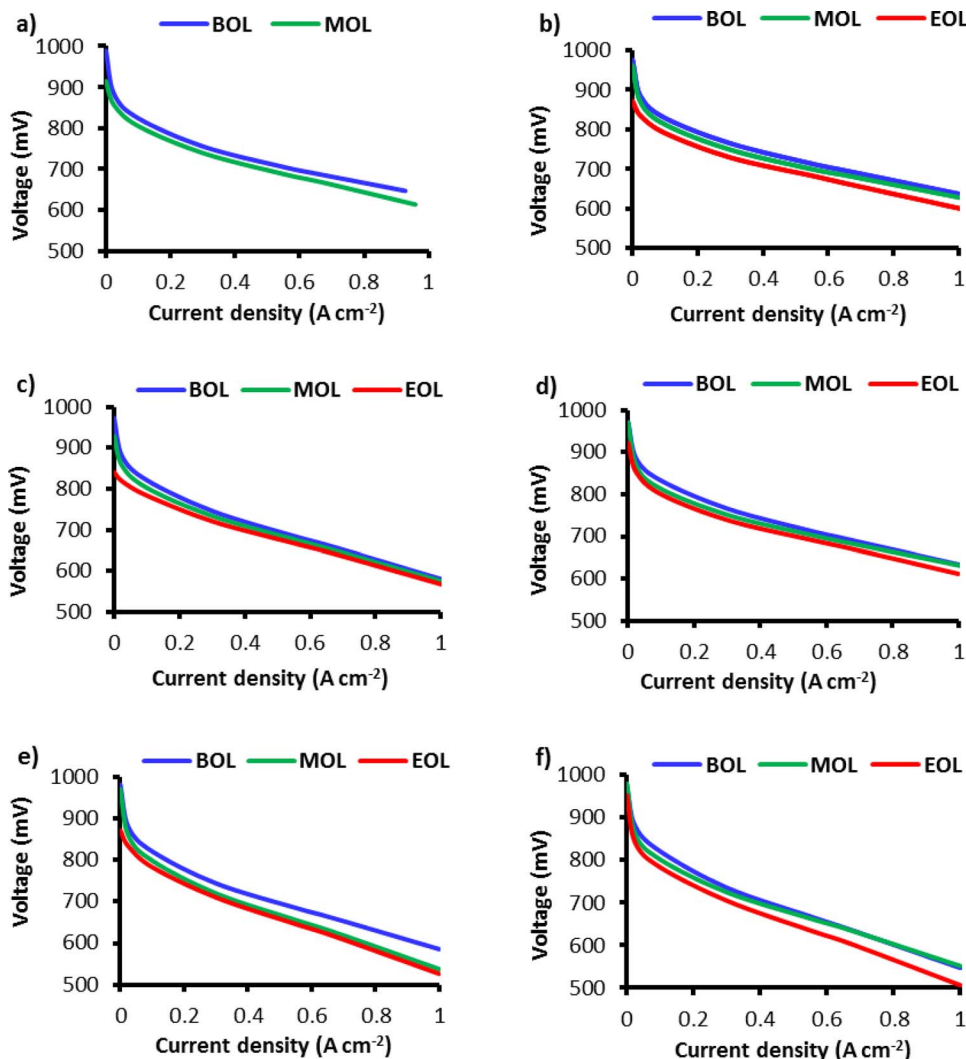


**Figure 4.** Polarization curve decay of the various AMDT runs: a) initiation; b) baseline; c) 90% RH; d) 100% RH; e) PITM-1; and f) PITM-2.

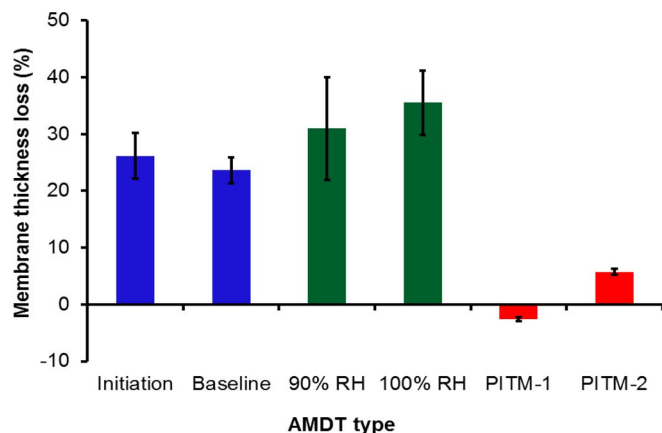


**Figure 5.** Membrane thinning (thickness loss, in % of original thickness) measured by SEM at the end of life of the various AMDT runs.

instance, the baseline had a performance loss of about 30 mV compared to an OCV loss of 100 mV.

**Membrane thinning and fluoride loss.**— Membrane thinning was prevalent in the AMDT degraded samples. Figure 5 shows the average membrane thickness loss in the different AMDT samples compared to the BOL membrane. It can be seen from Figure 5 that the baseline and constant RH samples experienced significant membrane thinning, while the membrane thickness in the PITM samples remained mostly unchanged. Membrane thinning is considered evidence of chemical degradation, which was effectively mitigated in the PITM samples. Although the constant RH samples exhibited more membrane thinning than the baseline, it should be mentioned that constant RH samples were exposed to AMDT stressors for a longer time before failure compared to the baseline samples; hence they experienced more chemical degradation, leading to general membrane thinning in all locations. The thinning level of the initiation sample was however similar to that of the baseline despite its shorter AMDT duration. Hence, the majority of the global chemical degradation is expected to occur during the initiation phase. The baseline membranes exhibited the most severe membrane thinning at the outlets, while membrane thinning was observed at both the inlets and outlets of the initiation membranes. The baseline AMDT thinning levels are roughly half of the COCV AST, which had a 48% membrane thickness loss in only half of the testing time.<sup>34</sup> This is due to much milder AMDT conditions compared to AST conditions.

Fluoride release is another important indicator of chemical membrane degradation which was monitored periodically during the experiments. The cumulative fluoride release data in Figure 6 show that the AMDT fluoride loss was generally in good agreement with the thickness loss, which confirms the findings reported above. The relative rates of chemical membrane degradation can be assessed by comparing the slopes of the curves; the baseline had the highest rate followed by the 90% RH, 100% RH, PITM-1, and PITM-2 conditions, which is consistent with the relative severity of the chemical stressors in each case. The baseline thinning rate was approximately equal to its fluoride release. However, the constant RH runs showed higher thinning than fluoride release combined with a relatively large variability. The suppressed rate of fluoride removal from the degraded membranes in this case may be due to the absence of liquid water dynamics otherwise induced by RH cycling. The PITM runs showed very low fluoride release which is consistent with the thinning results. The effluent water of the initiation AMDT was not collected; hence there is no fluoride loss data available for this run.

**Failure analysis.**— Membrane holes and fracture sites are indicative of the regions exposed to the most aggressive levels of degrada-

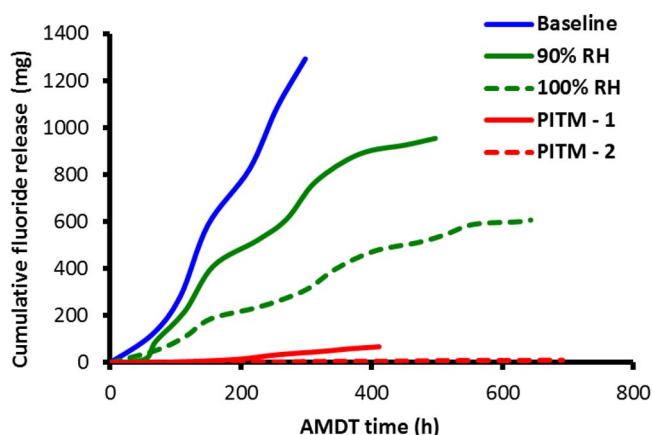


**Figure 6.** Cumulative fluoride release during AMDT operation, obtained from conductivity measurements on the effluent water from the stacks.

tion. Figure 7 shows representative SEM images of the different failure modes observed in the AMDTs.

The baseline AMDT generated membrane holes of 50–300  $\mu\text{m}$  diameter with a hole count density of 2.9 holes per  $\text{cm}^2$ . The mechanical stress during RH cycling of the baseline AMDT is assumed to be responsible for the rough character of transfers seen as cracks and tears around the holes, shown in the SEM micrograph in Figure 7a. The initiation leaks had an average diameter of 200  $\mu\text{m}$  with 1.3 holes per  $\text{cm}^2$ . The initiation MEAs exhibited divot and crack formation from both the anode and cathode sides (Figure 7b). The membranes also showed holes with rough edges similar to the baseline, as a result of combined chemical and mechanical degradation. Delamination between the membrane and catalyst layers was also commonly observed for both tests, presumably due to membrane degradation at the interfaces. Only one 40  $\mu\text{m}$  hole was found in the 90% RH membranes (0.04 holes per  $\text{cm}^2$ ). The 100% RH membrane had an average hole diameter of 40  $\mu\text{m}$  with 1.2 holes per  $\text{cm}^2$ . The surfaces around the holes were smooth in both AMDTs at constant RH, with areas of chemically eroded membrane, seen in Figure 7c. Due to the absence of mechanical degradation there were almost no cracks or fractures and all damage appeared to be chemical in nature. Only one divot was found in PITM-1, and 0.68 holes per  $\text{cm}^2$  were identified. Only two cells failed due to large leaks in PITM-2 while the remaining eight cells were still in good condition. One divot and 0.33 holes per  $\text{cm}^2$  were found. The character of holes in PITM-1 and PITM-2 was of combined chemical and mechanical stress, where the surrounding areas were irregular with rips and tears, similar to the baseline and initiation tests. Divots appeared in local regions without a platinum band, indicating lower chemical degradation mitigation capabilities in these areas, such as those observed in Figure 7d. It is anticipated that divots formed in these areas would eventually grow to holes such as those observed in Figure 7a due to combined chemical and mechanical degradation. This suggests that while the Pt band is effective in mitigation of chemical degradation, a complete coverage is essential in order to avoid local degradation and damage.

**Pt band location and concentration.**— The Pt concentration in the Pt band from inlet to outlet of the PITM membranes is shown in Figure 8. The membranes had the highest Pt concentration at the outlet and a lower concentration at the middle and inlet positions, in good agreement with the primary location of holes at the inlet. PITM-1 membranes displayed a wide Pt band located at a distance of 33% of the membrane thickness from the cathode interface, with Pt concentrations between 2,000 and 18,000 ppm in the band. In PITM-2, a Pt band was observed at a distance of 40% from the cathode, with Pt concentrations between 11,000 to 43,000 ppm. It is believed that the higher PITM concentration of PITM-2 was responsible for the life-time extension compared to PITM-1, in particular due to a better

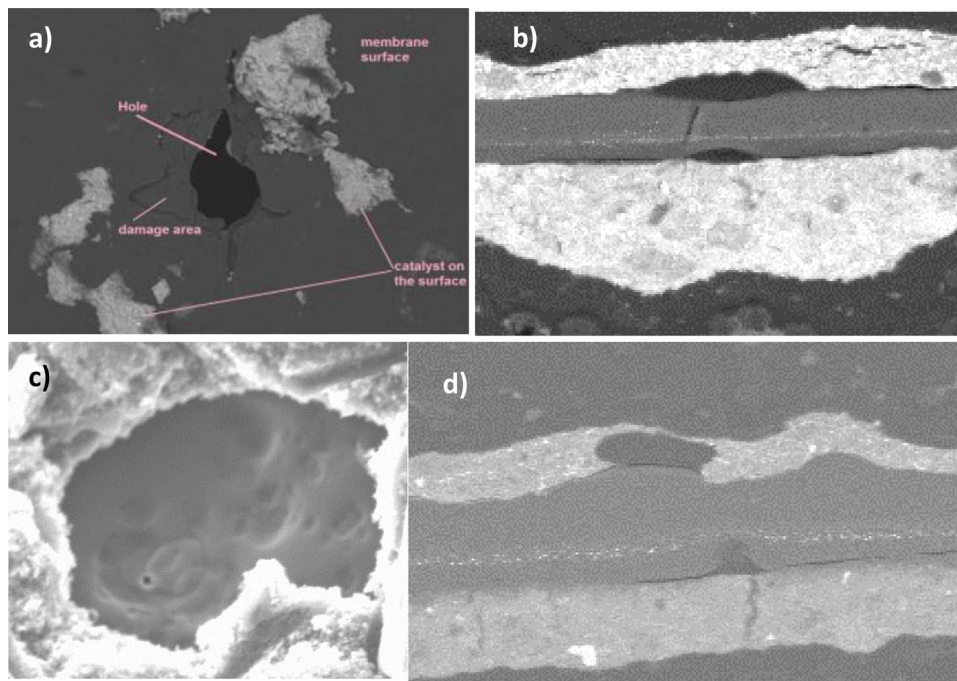


**Figure 7.** Representative SEM images of the membrane damage induced by AMDT operation: a) baseline; b) initiation; c) constant RH; and d) PITM AMDT runs.

coverage at the inlet region where gaps in the Pt band were found to allow local chemical degradation. The Pt concentration in the band also appeared to decrease in regions adjacent to large catalyst layer delamination sites, in good agreement with the locations of transfers.

*Mechanical properties.*— Tensile tests were conducted for AMDT degraded (EOL) catalyst coated membranes (CCMs) as well as fresh (BOL) CCMs in order to evaluate the effect of different AMDT stressors on the mechanical properties. Figure 9 illustrates the representative stress–strain curves of different AMDT samples at room and fuel cell conditions. The first curve represents the BOL and the rest are AMDT degraded samples. At room conditions (Figure 9a), BOL samples stretched well until the maximum traveling length of the DMA (~160% strain). Among all AMDT samples, only the PITM samples resembled the ductile behavior of the BOL sample, while the baseline AMDT and constant RH samples fractured quickly, right after passing

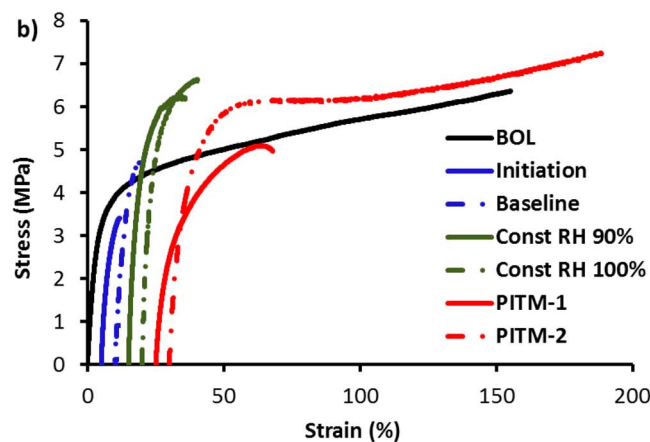
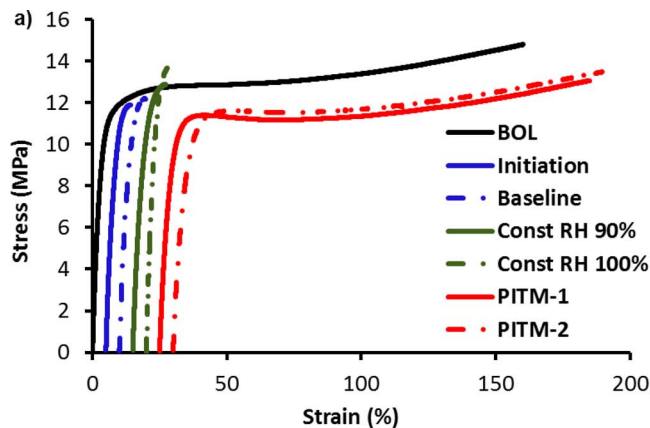


**Figure 9.** Tensile stress–strain curves of BOL and AMDT degraded catalyst coated membranes at (a) room conditions and (b) fuel cell conditions. The origin of the curves is shifted from zero strain to higher values for clarity.

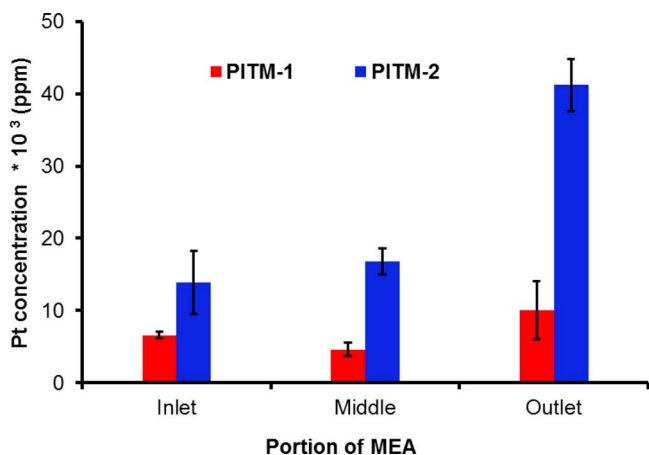


**Figure 8.** Pt concentration at the Pt band location in the membrane from inlet to outlet (at end of life) for the two AMDT runs with PITM.

their yield stress. It is suggested that polymer chain degradation and decrease in molecular weight resulting from chemical degradation reduces the chain entanglement and allows for easier chain detachment<sup>21</sup> leading to a much lower fracture strain in the baseline and constant RH AMDTs.

At fuel cell conditions (Figure 9b), analogous to room conditions, BOL samples reached the DMA traveling length limit. On the other hand, the baseline AMDT and constant RH samples fractured at low strains after passing the elastic region. However, only the PITM-2 sample was able to endure the tensile test while the PITM-1 sample fractured at around 40% strain.

By comparing the plots in Figure 9, it can be summarized that chemical degradation had the strongest effect on the ductility of the EOL membranes since no brittleness was observed in the PITM samples, where chemical degradation was mitigated by introducing platinum into the membrane. Chemical degradation causes polymer chain disentanglement and membrane thinning in early stages of the AMDT which is accompanied by the formation of pinholes and divots prior to failure.

The two baseline AMDT samples exhibited similar tensile properties although the initiation AMDT was extracted from the stack well before failure. These results are evidence that chemical degradation in the first stages of the AMDT appears as polymer chain degradation and has the most crucial effect on membrane embrittlement during AMDT. This also indicates that the mechanical properties may primarily decay during the initiation phase, and that after hole formation, the hydrogen leaks generated may result in less severe conditions for chemical degradation and therefore limited further decay in mechanical properties. Another important observation is that once holes were formed, the mechanical properties remained the same, regardless of the size of the holes.

On the other hand, removal of mechanical degradation in constant RH AMDTs did not improve membrane ductility when compared to the ductility of the baseline AMDTs. The material's ability to absorb energy before rupture is defined as material toughness and is determined by calculating the area below the stress – strain curve. Based on this definition, BOL and PITM EOL samples showed higher toughness and required much more energy to fracture compared to the baseline and constant RH EOL samples subjected to severe chemical degradation.

Figure 10a presents the final strain of the AMDT samples in mechanical tests at both room and fuel cell conditions. The main discrepancy between the room and fuel cell condition results was observed in the PITM-1 sample where testing at high temperature and water content led to much lower elongation. This may be due to the lower ability of the membrane in PITM-1 to absorb water compared to PITM-2, indicating a higher level of destruction of the water channels in the membrane due to chemical degradation. On the other hand the water channel structure appeared to be highly preserved in the PITM-2 membrane. PITM-2 was found to have a much higher platinum concentration in the membrane, which suggests that increased PITM levels may result in a higher level of preservation of the membrane water channels and therefore mechanical properties.

The elastic modulus is an indication of the material's resistance against elastic deformation and is another important mechanical property evaluated in this study, as depicted in Figure 10b. In agreement with the literature, the elastic modulus is a function of test conditions and was significantly reduced by increasing the temperature and relative humidity.<sup>23,30</sup> The PITM samples exhibited a lower elastic modulus and less resistance against deformation, i.e. less stiffness, compared to the baseline and constant RH samples. High elastic modulus and the lack of ductility observed in the baseline and constant RH cases can more easily lead to crack initiation in highly degraded areas, where the membrane experiences high stresses due to local degradation. In contrast, high elastic modulus and stiffness can reduce membrane swelling and contraction and control hygrothermal cyclic stress induced during humidity cycles. In the baseline and constant RH samples, severe chemical degradation may lead to reduced water uptake in the membrane, as indicated by the minor stiffening

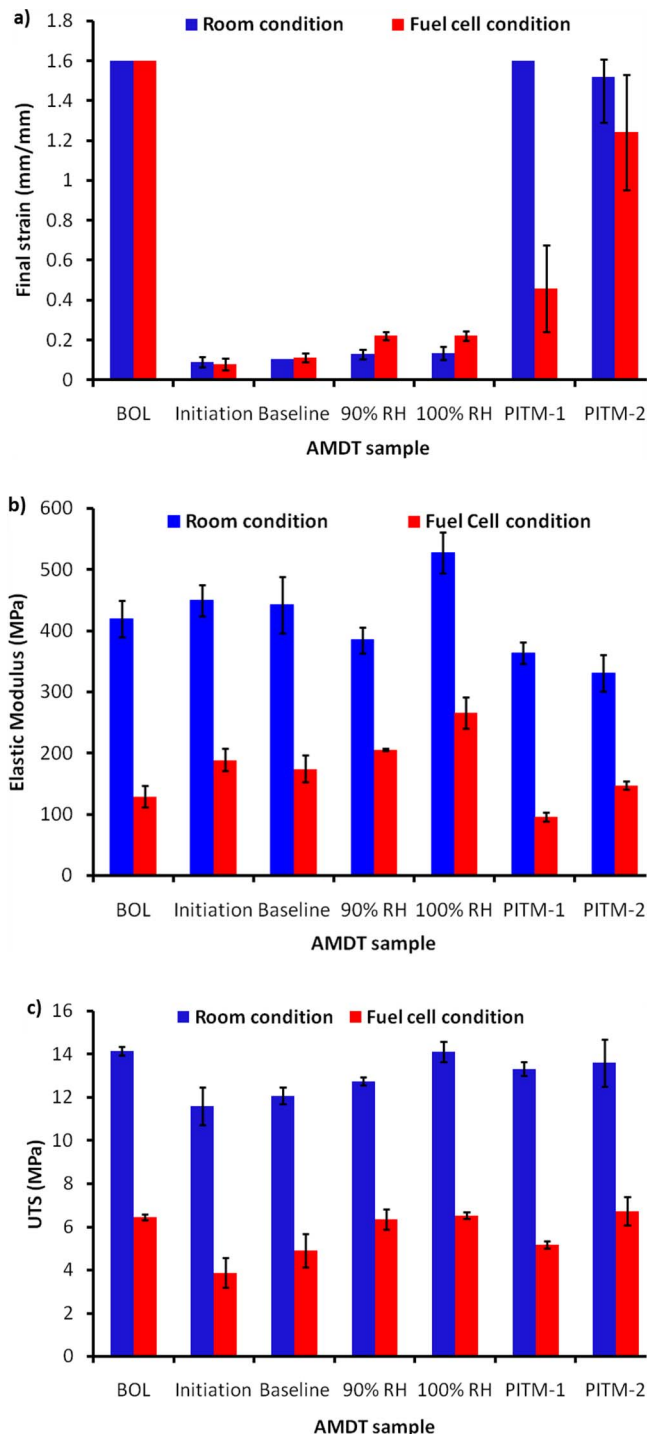


**Figure 10.** Tensile properties of BOL and AMDT degraded catalyst coated membranes at room (23°C, 50% RH) and fuel cell (70°C, 90% RH) conditions: (a) final strain; (b) elastic modulus; and (c) UTS.

effect (increased elastic modulus) observed at fuel cell conditions but not at room conditions.

The maximum stress tolerated by the CCMs during the tensile test, i.e., the ultimate tensile strength (UTS), is presented in Figure 10c. The UTS remained unchanged in the constant RH and PITM samples, which were mainly affected by chemical degradation and mechanical degradation, respectively. However, in the baseline AMDTs, the UTS decreased at room and fuel cell conditions. Polymer main chain degradation and membrane global thinning caused by chemical degradation

accompanied with microcracks and mechanical defects resulted from mechanical degradation may have led to a compounded reduction in membrane tolerance against mechanical loading. However, more intermediate samples would be required to elucidate conclusive trends in UTS.

As a summary of the mechanical properties represented in Figures 9 and 10 it was determined that the decay in mechanical properties was largely dominated by chemical degradation where the membrane (in a CCM) was transformed from a ductile to a fragile material in the baseline and constant RH samples. In contrast, in the PITM samples where chemical degradation mechanisms were controlled to some extent, the ductility and toughness of the membrane were maintained. However, it is also evident that that mechanical damage generated during RH cycling may accelerate the decay in mechanical properties through nucleation of mechanical microcracks at chemically degraded sites.

### Conclusions

A baseline accelerated membrane durability test (AMDT) protocol was established for heavy duty fuel cell applications along with complementary experimental investigations to elucidate the respective roles of chemical and mechanical stressors in the overall membrane degradation mechanism and their impact on membrane life-time. The proposed baseline AMDT successfully accelerated membrane degradation using combined chemical-mechanical stress and significantly reduced the time to failure compared to regular duty cycle operation, achieving membrane failure in less than 300 hours. The failure modes obtained with the AMDT were similar to those observed during field operation, comprising holes and cracks in the membrane accompanied by local thinning, which demonstrates the effectiveness of the test protocol. It was found that under baseline AMDT conditions, the majority of the chemical membrane degradation occurred during the leak initiation period, followed by a rapid growth of the leak rate caused primarily by mechanical degradation.

The effects of RH cycling and Pt in the membrane were evaluated in complementary AMDT runs. The effect of RH cycling was visible when the tests at constant RH lasted significantly longer than the baseline, confirming that RH cycling indeed accelerates membrane degradation. RH cycling was found to gradually decrease the strength of the membrane due to the imposed mechanical stress, which was also found to exacerbate the effect of chemical degradation. The AMDTs at constant RH exhibited slower leak growth than the baseline, allowing for longer operation of membranes with leaks. The membrane life-time at 90% RH was shorter than at 100% RH, proving that the level of chemical membrane degradation increases with reduced humidity. The largest hole sizes and densities were found in the RH cycled samples, which also exhibited rougher damage structure indicative of mechanical degradation.

Platinum band formation extended the membrane life-time and prevented decay in thickness and elongation which suggests mitigation of chemical degradation. As a result the AMDTs with PITM displayed up to a doubling of the effective life-time. The test with high PITM concentration resulted in the longest life-time, while the test with low PITM concentration was found to have areas with gaps in the Pt band that were prone to local chemical degradation and earlier failures. Tensile tests on AMDT degraded samples determined the deterioration of CCM toughness in samples subjected to chemical degradation, while in PITM samples where chemical degradation was controlled, the mechanical strength of the membrane was preserved.

From these results, it can be concluded that PITM and constant RH operation result in enhanced membrane life-time under heavy duty fuel cell conditions. The baseline AMDT protocol developed and demonstrated in this work is recommended for rapid and reliable testing of membrane durability for heavy duty fuel cell applications.

### Acknowledgments

Funding for this research provided by Automotive Partnership Canada (APC), Natural Sciences and Engineering Research Coun-

cil of Canada (NSERC), and Ballard Power Systems is gratefully acknowledged. Ballard Power Systems is also acknowledged for providing access to experimental facilities and technical support. The authors thank Ramin Khorasany, Jeetinder Ghataurah, Mark Cruickshank, Freda Feng, Trevor Engh, and Curtis Allen for assisting with experimentation and characterization.

### References

- World Health Organization, *7 million premature deaths annually linked to air pollution*, (2014) <http://www.who.int/mediacentre/news/releases/2014/air-pollution/en/>.
- U.S. DOE National Renewable Energy Laboratory, (2012) [http://www.energy.gov/sites/prod/files/2014/03/f12/fceb\\_status\\_2012.pdf](http://www.energy.gov/sites/prod/files/2014/03/f12/fceb_status_2012.pdf).
- K. H. Wong and E. Kjeang, *J. Electrochem. Soc.*, **161**, F823 (2014).
- M. Danilczuk, F. D. Coms, and S. Schlick, *J. Phys. Chem. B*, **113**, 8031 (2009).
- L. Gubler, S. M. Dockheer, and W. H. Koppenol, *J. Electrochem. Soc.*, **158**, B755 (2011).
- A. Bosnjakovic and S. Schlick, *J. Phys. Chem. B*, **108**, 4332 (2004).
- L. Ghassemzadeh, K. D. Kreuer, J. Maier, and K. Muller, *J. Power Sources*, **196**, 2490 (2011).
- T. Ishimoto, R. Nagumo, T. Ogura, T. Ishihara, B. Kim, A. Miyamoto, and M. Koyama, *J. Electrochem. Soc.*, **157**, B1305 (2010).
- A. Pozio, R. F. Silva, M. De Francesco, and L. Giorgi, *Electrochim. Acta*, **48**, 1543 (2003).
- E. Endoh, S. Terazono, H. Widjaja, and Y. Takimoto, *Electrochem. Solid-State Lett.*, **7**, A209 (2004).
- V. O. Mittal, H. Russell Kunz, and J. M. Fenton, *Electrochem. Solid-State Lett.*, **9**, A299 (2006).
- V. O. Mittal, H. R. Kunz, and J. M. Fenton, *J. Electrochem. Soc.*, **154**, B652 (2007).
- L. Ghassemzadeh and S. Holdcroft, *J. Am. Chem. Soc.*, **135**, 8181 (2013).
- Lida Ghassemzadeh, T. J. Peckham, T. Weissbach, X. Luo, and S. Holdcroft, *J. Am. Chem. Soc.*, **135**, 15923 (2013).
- X.-Z. Yuan, S. Zhang, H. Wang, J. Wu, J. C. Sun, R. Hiesgen, K. A. Friedrich, M. Schulze, and A. Haug, *J. Power Sources*, **195**, 7594 (2010).
- S. D. Knights, K. M. Colbow, J. St-Pierre, and D. P. Wilkinson, *J. Power Sources*, **127**, 127 (2004).
- M. V. Williams, H. R. Kunz, and J. M. Fenton, *J. Power Sources*, **135**, 122 (2004).
- U.S. Department of Energy Hydrogen Program, *Enabling Commercial PEM Fuel Cells with Breakthrough Lifetime Improvements*, (2004) [http://www.hydrogen.energy.gov/pdfs/progress05/vii\\_b\\_3\\_escobedo.pdf](http://www.hydrogen.energy.gov/pdfs/progress05/vii_b_3_escobedo.pdf).
- B. P. Pearman, in *2012 Fuel Cell Seminar & Exposition*, (2012).
- L. Gubler and W. H. Koppenol, *J. Electrochem. Soc.*, **159**, B211 (2012).
- Y. P. Patil, W. L. Jarrett, and K. A. Mauritz, *J. Memb. Sci.*, **356**, 7 (2010).
- R. M. H. Khorasany, M.-A. Goulet, A. S. Alavijeh, E. Kjeang, G. G. Wang, and R. K. N. D. Rajapakse, *J. Power Sources*, **252**, 176 (2014).
- H. Tang, S. Peikang, S. P. Jiang, F. Wang, and M. Pan, *J. Power Sources*, **170**, 85 (2007).
- M.-A. Goulet, R. M. H. Khorasany, C. De Torres, M. Lauritzen, E. Kjeang, G. G. Wang, and N. Rajapakse, *J. Power Sources*, **234**, 38 (2013).
- G. De Moor, C. Bas, F. Lesage, A. S. Danérol, E. Claude, E. Rossinot, M. Paris, L. Flandin, and N. D. Albérola, *J. Appl. Polym. Sci.*, **120**, 3501 (2011).
- G. De Moor, C. Bas, N. Charvin, E. Moukheiber, F. Niepceon, N. Breilly, J. André, E. Rossinot, E. Claude, N. D. Albérola, and L. Flandin, *Fuel Cells*, **12**, 356 (2012).
- M.-A. Goulet, S. Arbour, M. Lauritzen, and E. Kjeang, *J. Power Sources*, **274**, 94 (2015).
- R. M. H. Khorasany, A. S. Alavijeh, E. Kjeang, G. G. Wang, and R. K. N. D. Rajapakse, *J. Power Sources*, **274**, 1208 (2015).
- S. Subianto, M. Pica, M. Casciola, P. Cojocar, L. Merlo, G. Hards, and D. J. Jones, *J. Power Sources*, **233**, 216 (2013).
- X. Huang, R. Solasi, Y. Zou, M. Feshler, K. Reifsnider, D. Condit, S. Burlatsky, and T. Madden, *J. Polym. Sci. Part B Polym. Phys.*, **44**, 2346 (2006).
- K. Panha, M. Fowler, X.-Z. Yuan, and H. Wang, *Appl. Energy*, **93**, 90 (2012).
- S. Vengatesan, M. W. Fowler, X.-Z. Yuan, and H. Wang, *J. Power Sources*, **196**, 5045 (2011).
- F. Barbir, B. Wahdame, D. Candusso, X. François, F. Harel, M.-C. Péra, D. Hissel, and J.-M. Kauffmann, *Int. J. Hydrogen Energy*, **32**, 4523 (2007).
- C. Lim, L. Ghassemzadeh, F. Van Hove, M. Lauritzen, J. Kolodziej, G. G. Wang, S. Holdcroft, and E. Kjeang, *J. Power Sources*, **257**, 102 (2014).
- A. Sadeghi Alavijeh, M. A. Goulet, R. M. H. Khorasany, J. Ghataurah, C. Lim, M. Lauritzen, E. Kjeang, G. G. Wang, and R. K. N. D. Rajapakse, *Fuel Cells* (2014) Under review.
- W. Gu, R. N. Carter, P. T. Yu, and H. Gasteiger, *ECS Trans.*, **11**, 963 (2007).
- K. Sasaki, M. Shao, and R. Adzic, in *Polymer Electrolyte Fuel Cell Durability*, F. N. Büchi, M. Inaba, and T. J. Schmidt, Editors, p. 10–27, Springer (2009).
- L. Dubau, J. Durst, F. Maillard, M. Chatenet, J. André, and E. Rossinot, *Fuel Cells*, **12**, 188 (2012).
- S. F. Burlatsky, M. Gummalla, V. V. Atrazhev, D. V. Dmitriev, N. Y. Kuzminykh, and N. S. Erikhman, *J. Electrochem. Soc.*, **158**, B322 (2011).
- H. Schulenburg, B. Schwanitz, J. Krbanjevic, N. Linse, G. G. Scherer, and A. Wokaun, *Electrochem. Commun.*, **13**, 921 (2011).
- H. Hagihara, H. Uchida, and M. Watanabe, *Electrochim. Acta*, **51**, 3979 (2006).
- J. Zhang, B. Litterer, W. Gu, H. Liu, and H. Gasteiger, *J. Electrochem. Soc.*, **154**, B1006 (2007).

43. D. Zhao, B. L. Yi, H. M. Zhang, and M. Liu, *J. Power Sources*, **195**, 4606 (2010).
44. Z. Liu, Y. Yang, W. Lü, C. Wang, M. Chen, and Z. Mao, *Int. J. Hydrogen Energy*, **37**, 956 (2012).
45. M. P. Rodgers, L. J. Bonville, and D. K. Slattery, *ECS Trans.*, **41**, 1461 (2011).
46. M. P. Rodgers, D. A. Cullen, J. Leonard, D. K. Slattery, and J. M. Fenton, in *Carisma 2012 – 3rd Carisma International Conference*, p. 1–19 (2012).
47. N. E. Cipollini, *ECS Trans.*, **11**, 1071 (2007).
48. S. Helmly, B. Ohnmacht, R. Hiesgen, E. Gülzow, and K. A. Friedrich, *ECS Trans.*, **58**, 969 (2013).
49. S. Helmly, B. Ohnmacht, P. Gazdzicki, R. Hiesgen, E. Gulzow, and K. A. Friedrich, *J. Electrochem. Soc.*, **161**, F1416 (2014) <http://jes.ecsdl.org/content/161/14/F1416.full>.
50. E. Guilminot, A. Corcella, M. Chatenet, F. Maillard, F. Charlot, G. Berthomé, C. Iojoiu, J.-Y. Sanchez, E. Rossinot, and E. Claude, *J. Electrochem. Soc.*, **154**, B1106 (2007).
51. C. Iojoiu, E. Guilminot, F. Maillard, M. Chatenet, J.-Y. Sanchez, E. Claude, and E. Rossinot, *J. Electrochem. Soc.*, **154**, B1115 (2007).
52. N. Macauley, L. Ghassemzadeh, C. Lim, M. Watson, J. Kolodziej, M. Lauritzen, S. Holdcroft, and E. Kjeang, *ECS Electrochem. Lett.*, **2**, F33 (2013).
53. A. P. Young, J. Stumper, S. Knights, and E. Gyenge, *J. Electrochem. Soc.*, **157**, B425 (2010).
54. J. Fimrite, B. Carnes, H. Struchtrup, and N. Djilali, *J. Electrochem. Soc.*, **152**, A1815 (2005).
55. T. E. Springer, T. A. Zawodzinski, and S. Gottesfeld, *J. Electrochem. Soc.*, **138**, 2334 (1991).
56. U.S. Department of Energy, *DOE CELL COMPONENT ACCELERATED STRESS TEST*, (2010) [http://www1.eere.energy.gov/hydrogenandfuelcells/pdfs/component\\_durability\\_may\\_2010.pdf](http://www1.eere.energy.gov/hydrogenandfuelcells/pdfs/component_durability_may_2010.pdf).
57. V. A. Sethuraman, J. W. Weidner, A. T. Haug, S. Motupally, and L. V. Protsailo, *J. Electrochem. Soc.*, **155**, B50 (2008).
58. S. Vengatesan, K. Panha, M. W. Fowler, X. Z. Yuan, and H. Wang, *J. Power Sources*, **207**, 101 (2012).
59. L. Dubau, L. Castanheira, F. Maillard, M. Chatenet, O. Lottin, G. Maranzana, J. Dillet, A. Lamibrac, J.-C. Perrin, E. Moukheiber, A. Elkaddouri, G. De Moor, C. Bas, L. Flandin, and N. Caqué, *Wires energy Environ.*, **3**, 540 (2014).
60. M. Ohishi, Y. Ono, and K. Fushinobu, *Nanoscale Microscale Thermophys. Eng.*, **17**, 69 (2013).

# **Appendix C**

## **Effect of Platinum in the Membrane on Fuel Cell Membrane Durability**

# **Favorable Effect of In-Situ Generated Platinum in the Membrane on Fuel Cell Membrane Durability**

Natalia Macauley<sup>a</sup>, Ka Hung Wong<sup>a</sup>, Mark Watson<sup>b</sup>, and Erik Kjeang<sup>a\*</sup>

<sup>a</sup> School of Mechatronic Systems Engineering, Simon Fraser University, 250-13450 102 Avenue,  
Surrey, BC V3T0A3 Canada

<sup>b</sup> Ballard Power Systems, 9000 Glenlyon Parkway, Burnaby, BC V5J5J8 Canada

\*ekjeang@sfu.ca

## **Abstract**

The overall lifetime of polymer electrolyte fuel cells is often determined by the membrane durability. Platinum, which may dissolve from the catalyst layers during fuel cell operation and deposit in the membrane, has been shown to have both positive and negative effects on membrane stability. In the present work, we analyze what specific conditions are required in order to reach a favorable, membrane stabilizing effect with the controlled use of platinum in the membrane. Using accelerated membrane durability testing, field operated membrane samples, and electron microscopy, we demonstrate that a high platinum concentration with specific particle shapes and sizes is essential for enhanced membrane stability. Specifically, star shaped and dendritic particles with high particle density and high surface area are shown to be preferable. These particles contain high levels of Pt(111) and are expected to have high catalytic activity toward peroxide quenching and crossover gas consumption, thereby mitigating chemical membrane degradation. On the other hand, small, dispersed cubic particles are found to have no effect or the opposite, negative effect on membrane stability.

**Keywords:** fuel cell; durability; membrane; platinum; transmission electron microscopy

## 1. Introduction

Polymer electrolyte fuel cells are promising for application in transportation, but automotive driving generates conditions that exacerbate both membrane and catalyst degradation. Heavy and light duty durability targets of 18,000 and 5,000 h, respectively [1,2], are yet to be demonstrated in field operation, which makes the development of highly durable fuel cell components a priority. Fuel cell membranes degrade chemically and mechanically during vehicle operation leading to membrane thinning and pinhole and crack formation over time. Chemical membrane degradation occurs primarily due to radical attack of the ionomer, where radicals are mainly produced from hydrogen peroxide in the presence of Fenton's reagents [3–5]. Chemical degradation is most severe at open circuit voltage [6,7] due to a recently proposed iron ion redox cycle that controls the  $\text{Fe}^{2+}$  concentration in the membrane through reaction-transport phenomena of mobile and redox active iron ions [8]. Mechanical membrane degradation is a result of membrane swelling and shrinking as a response to changes in membrane humidity, eventually leading to membrane fatigue and creep over time [9–12]. Mechanical weakening of membrane properties has also been shown to exacerbate the effect of chemical degradation [12,13]. Mitigation strategies for chemical membrane degradation include chemical stabilization of end groups [14], the use of  $\text{H}_2\text{O}_2$  decomposition agents such as manganese [15] and zirconia [16], and radical scavengers such as cerium oxide [15,17–19]. Some of the methods used to mitigate mechanical membrane degradation are cross-linking, physical reinforcement with a porous polymer matrix, fibers, or inorganic reinforcement, and ensuring adequate bonding of internal layers [17–19].

Fuel cell catalyst layer degradation is caused by Pt dissolution and corrosion of carbon support during fuel cell operation. Pt dissolution occurs during load cycling, when the platinum

oxide film that initially forms on the catalyst surface above 0.85 V [23,24] is removed from the catalyst surface once the voltage is swept below 0.6 V [25]. Instability between the Pt-Pt bonds in the first two atomic layers of the catalyst cause Pt ion dissolution and subsequent migration into the membrane [23]. Carbon corrosion is caused by the reverse-current mechanism, which occurs when air is present at the anode and cathode during introduction of hydrogen into the anode upon startup. This results in a high interfacial potential difference in the region where hydrogen is absent. If the potential exceeds 1.1 V, the carbon support in the cathode is electrochemically oxidized into CO<sub>2</sub> [26,27]. Outlets have the highest carbon corrosion levels because incoming hydrogen takes longer to reach them [28]. Carbon corrosion can also occur during localized hydrogen starvation, whereby higher temperatures promote more carbon corrosion [29]. Carbon free supports such as SnO<sub>2</sub> and Ti<sub>4</sub>O<sub>7</sub> avoid the issue of carbon corrosion [30].

The chemical reduction of dissolved Pt ions by H<sub>2</sub> permeating through the membrane from the anode side leads to Pt particle deposition in the membrane, and ultimately the formation of a densely packed band at a specific distance from the cathode [31]. The relative local fluxes of H<sub>2</sub> and O<sub>2</sub> within the membrane and the H<sub>2</sub>/O<sub>2</sub> partial pressures determine the location of the Pt band [25,32–35], and the incoming crossover gases can be consumed at the Pt band to form water [36]. The potential distribution in the membrane is stepped from 0 V to 0.8 – 1 V between the anode and cathode, based on H<sub>2</sub> and O<sub>2</sub> permeation in the membrane, respectively [34]. The potential in the vicinity of a Pt particle decreases with increasing particle size in the anodic region and increases in the cathodic region, governing the dominant reaction at each particle surface [37]. In general, Pt particles can take a wide variety of shapes and sizes, and the most common shapes include truncated nanooctahedrons, nanocubes, and nanooctapods [38]. About

80% of the total surface area of Pt nanoparticles is composed of face centered cubic (fcc) (111) faces [39]. Pt nanocrystals exhibit shape- and size-dependent catalytic properties [39]. Tetrahedral nanoparticles have the highest fraction of surface atoms located on corners and edges [40] and consist of mostly Pt(111), which has the most stable close-packed surfaces and the lowest activation energy [38]. Thereby, the catalytic activity of Pt surfaces identified in tetrahedral, spherical, and cubic particles follows the order of Pt(111) > Pt(411) > Pt(100), respectively [38].

In regards to the chemical stability of the membrane, both positive and negative effects of platinum in the membrane (PITM) have been reported. The preparation method of membranes with Pt seems to influence the membrane response. For instance, ion-exchange with platinum-complex ions in  $[\text{Pt}(\text{NH}_3)_4]\text{Cl}_2$  solution followed by reduction in 1-pentanol resulted in a reduced fluoride emission in durability tests [41]. On the other hand, co-casting of PFSA membranes with Pt particles led to poor mechanical integrity, where the presence of Pt in the membrane was reported to increase membrane degradation due to increased radical formation [42–49]. Higher levels of OH radical formation at Pt particles in the membrane were detected at the anode side [50]. Helmly et al. examined chemically degraded membranes by atomic force microscopy and found the formation of electronic short-circuits due to the accumulation of Pt particles in the membrane, which led to enhanced degradation via formation of peroxide radicals and significant heat generation [45]. Rodgers et al. also attributed membrane degradation to Pt band formation in the membrane [46], but later concluded that high densities of PITM may deactivate generated radicals before they can attack the ionomer [43,44]. Helmly et al. did not identify degradation in membranes with Pt formed in-situ, which however was seen in membranes with ex-situ impregnated Pt [47]. Meanwhile, hydrogen peroxide and hydroxyl radical scavenging abilities of

Pt nanoparticles have been shown ex-situ [51–56] and the mitigating effect of the Pt band toward chemical degradation was demonstrated in-situ in our previous work [57,58]. 2,800 h field operated samples showed enhanced durability under accelerated stress test conditions [56] due to the presence of the Pt band in the membrane. Further investigations were conducted by subjecting membranes with artificially deposited PITM to an accelerated membrane durability test (AMDT) [57], in which they displayed visible lifetime extensions. In sharp contrast to regular membranes, membranes with PITM showed no membrane thinning, low fluoride emission rates, and highly preserved mechanical strength [58], meaning that the PITM must have substantially reduced the chemical degradation, presumably by decomposing  $H_2O_2$  to non-radical products [59,60] and/or converting crossover gases to water. However, the opposing results in the literature make the study of Pt particles in membranes with both enhanced and reduced durability important in order to understand the underlying mechanisms.

The objective of the present work is to identify the main differences between Pt particles in the membrane responsible for increased membrane stability and those that increase membrane degradation. Therefore, the effect of various PITM concentrations on membrane durability is first evaluated under AMDT conditions. The distribution and structure of the Pt particles in the laboratory generated PITM are then compared to the corresponding Pt particles observed in field operated membranes using transmission electron microscopy. Finally, the Pt particle size, shape, and density in the various membranes are correlated to membrane stability, with the intention of elucidating the underlying mechanism of enhanced stability by the Pt band [57,58].

## **2. Experimental**

Membranes with laboratory generated Pt band were degraded under accelerated membrane durability test (AMDT) conditions. Membrane electrode assemblies (MEAs) used for the AMDT

were made of catalyzed gas diffusion electrodes (GDEs). The GDEs were fabricated by coating a micro-porous layer made of polytetrafluoroethylene (PTFE) and carbon black on a non-woven carbon paper gas diffusion layer substrate [61] followed by coating of a catalyst layer that consisted of carbon-supported platinum catalyst and perfluorosulfonic acid (PFSA) ionomer [61]. MEAs were prepared by hot-pressing a standard non-reinforced PFSA ionomer membrane with anode and cathode GDEs [61].

The MEAs were tested in-situ using a 10-cell stack subjected to the recently developed AMDT protocol for heavy duty fuel cells with combined chemical and mechanical degradation [58]. The baseline AMDT was designed to estimate membrane durability by simulating the most stressful conditions for the membrane during bus driving, which includes idling at high voltages and hygrothermal variations due to the dynamic power demand from the vehicle. Therefore, a voltage hold at 9 V was applied to induce chemical degradation combined with mechanical stress from relative humidity (RH) cycling [58]. To further accelerate membrane degradation, the temperature and oxygen partial pressure were elevated to 85°C and 45%, respectively. An in-house technique was used to dissolve Pt from the cathode catalyst layer, allowing it to migrate into the membrane. Four variants of this technique were used to apply PITM either before or during AMDT operation. In the first case, 1,000 PITM generating cycles were applied prior to exposing the membrane to baseline AMDT conditions, denoted as LAB1. In the second case, one PITM generating cycle was integrated into the AMDT protocol after every 6<sup>th</sup> RH cycle, denoted as LAB2. LAB3 integrated a PITM generating cycle after every 12<sup>th</sup> RH cycle of the AMDT protocol, in this case using air conditions (21% O<sub>2</sub> concentration). Finally, LAB4 integrated a PITM generating cycle after every 24<sup>th</sup> RH cycle. All stacks with applied PITM were operated until failure as defined by the threshold hydrogen leak rate across the membrane of 100 sccm.

Effluent water was collected from the stack for fluoride emission rate (FER) determination before regular leak tests, after which a polarization curve was measured.

At the end of the test, an infrared (IR) camera was used to find the distribution of membrane leaks. Membrane thickness was measured using cross-sectional scanning electron microscopy (SEM; JEOL JSM-6360). The Pt concentration in the Pt band was measured by energy-dispersive X-ray spectroscopy (EDS) elemental analysis on the SEM. Transmission electron microscopy (TEM) was used to analyze the distribution and structure of the Pt particles in the membranes. TEM sample preparation was done on MEAs dried at ambient conditions for two hours prior to cutting out 1 cm<sup>2</sup> sections from the MEA inlet, middle, and outlet regions. The sections were further cut diagonally into identical triangles to create a tip. GDLs were carefully peeled off and the remaining catalyst coated membranes (CCMs) were embedded in Araldite 502 epoxy and cured at 70°C for 12 hours. A LEICA ultra-microtome was used to cut the embedded CCMs into 80-100 nm thin slices, always using a freshly prepared glass knife. Slices were placed on formvar coated 200-mesh copper grids, model FF200-Cu. Two transmission electron microscopes, STEM Hitachi-8100 and STEM FEI Tecnai Osiris, were used for nano-imaging of the Pt particles in the membrane at 200 kV. Image processing was done in ImageJ.

Field operated membrane samples were cut from partially aged MEAs extracted from the Whistler, British Columbia fuel cell bus fleet after 2,800, 4,400 and 8,200 hours of field operation. The real-world duty cycle experienced by these MEAs was similar albeit milder in nature to the conditions of the AMDT, featuring both chemical and mechanical membrane degradation. Additionally, as a result of catalyst layer degradation, these MEAs developed a Pt band in the membrane during regular bus operation. Field operated membranes were also leak tested to detect leaks and IR imaging was used to locate the position of leaks. Membrane

thickness was identified by SEM and EDS was used to measure the Pt concentration of the Pt band. Finally, TEM was used to analyze the Pt particle structure and distribution in the membranes.

### **3. Results and discussion**

To simulate the stabilizing effect of the Pt band seen in field operated membranes, membranes with laboratory generated platinum bands were produced in-situ and the effect of PITM on membrane stability was investigated under baseline AMDT conditions. As a reference, freshly manufactured membranes without PITM were exposed to baseline AMDT conditions at 21% and 45% O<sub>2</sub>. Four different variations of laboratory generated PITM were introduced by changing the frequency of the PITM generating cycles and their combination with the AMDT protocol. Firstly, a Pt band was generated prior to exposure to AMDT conditions in LAB1 to support the assumption that at mild operating conditions, membrane degradation may be negligible prior to Pt band formation in the field. On the other hand, integrating PITM generating cycles into the AMDT in LAB2, LAB3, and LAB4 after every 6<sup>th</sup>, 12<sup>th</sup>, and 24<sup>th</sup> RH cycle, respectively, may better simulate the real condition. In this case, the assumption is that Pt band generation in the field is gradual, and the membrane is exposed to degrading conditions prior to and during Pt band formation. To determine which mechanism is more plausible, the structure and distribution of laboratory generated Pt nanoparticles in the membrane was compared with PITM generated under field operating conditions. The findings were correlated to mitigation of chemical membrane degradation.

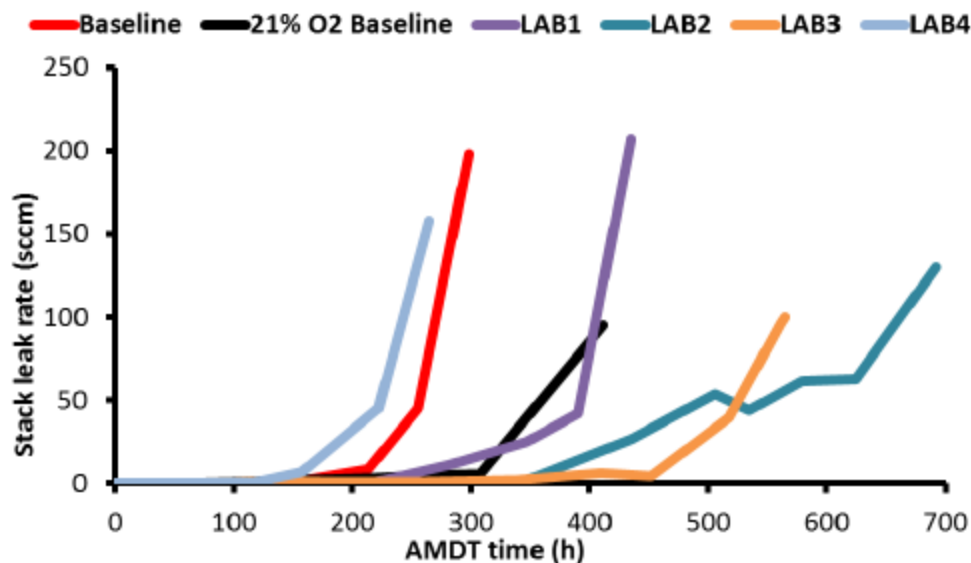


Figure 1. AMDT stack leak rate development with reference (regular AMDT baseline and 21% O<sub>2</sub> baseline) and Pt containing (LAB1, LAB2, LAB3, and LAB4) membranes.

The membrane leak rate development was monitored during the AMDT as an indicator of membrane health, as shown in Figure 1. The stack failure threshold was a leak rate of 100 sccm (10 sccm per cell). The lifetime of membranes with laboratory generated PITM was compared to the lifetime of reference membranes. The reference membrane lifetime was 298 h, and all ten cells failed with leak rates above 10 sccm [58]. LAB1 membranes displayed extended lifetime compared to the reference membranes, and lasted 435 h, with half of the cells in the stack still healthy. The Pt particles in LAB1, which were generated in the membrane prior to degradation, thereby successfully extended the membrane lifetime by approximately 50%. In LAB2, PITM was gradually deposited in the membrane by integrating a single PITM generating cycle after every 6<sup>th</sup> RH cycle of the baseline AMDT. LAB2 membranes displayed ~130% lifetime extension compared to reference membranes, by lasting 692 h. In addition, only two out of ten membranes actually failed with a leak rate above 10 sccm, which is supported by the slow leak

rate growth indicating local rather than global failure. A lower PITM concentration was generated in LAB3 by using a PITM generating cycle after every 12<sup>th</sup> RH cycle in a modified AMDT using air as oxidant, i.e., less frequently compared to LAB2. Despite the lower PITM loading, LAB3 still surpassed the lifetime of reference membranes at air conditions (412 h; seven failed membranes) with a lifetime of 564 h and only two failed membranes. This is evidence that LAB3 still contained sufficient PITM to preserve a higher number of membranes in the stack for a longer time, with a ~40% stack lifetime extension compared to the reference. Lastly, LAB4 was designed to have the lowest amount of PITM by using a PITM generating cycle after every 24<sup>th</sup> RH cycle of the baseline AMDT (at 45% O<sub>2</sub>). In this case, the lifetime of the membranes in LAB4 was shorter than the baseline, lasting only 243 h, with eight failed membranes. The low lifetime (~20% *below* the reference) and high number of failed membranes in LAB4 indicates a much less effective Pt band compared to the previous membranes with PITM. As a result of PITM, LAB1, LAB2, and LAB3 lasted 50%, 130%, and 40% longer than the reference stacks, respectively. LAB4 on the other hand had a lower lifetime than the reference, presumably due to the low PITM concentration.

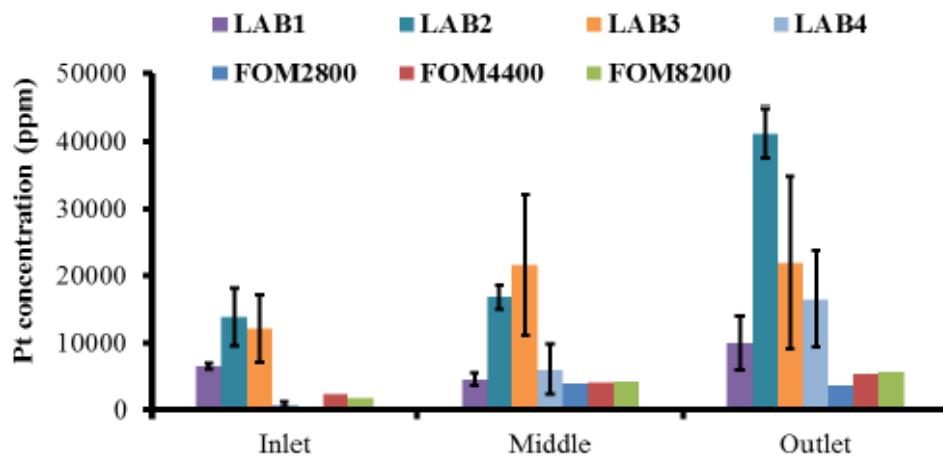


Figure 2. Pt concentration at the Pt band location of the AMDT (LAB1-4) and field operated (FOM) membranes measured at three regions from MEA inlet to outlet.

Figure 2 compares the Pt concentration at the Pt band location of the AMDT operated membranes (LAB1-4) to those of the field operated membranes (FOMs) obtained from the Whistler, British Columbia fuel cell bus fleet. As a result of the 21% O<sub>2</sub> partial pressure in air, the Pt band was identified 20% away from the cathode interface in FOMs and LAB3 membranes. Similarly, the Pt band in the LAB1, LAB2, and LAB4 membranes was located 33% - 40% away from the cathode due to the elevated 45% O<sub>2</sub> partial pressure. The Pt concentration was observed to increase from MEA inlet to outlet in all cases for both AMDT and field operated membranes. During extended field operation the outlet Pt concentration of the FOMs gradually increased from 3,700 to 5,700 ppm between 2,800 and 8,200 h of operation. The higher operating temperature of the AMDT operated membranes resulted in increased catalyst dissolution, especially in regions near the MEA outlets, where Pt concentrations reached 10,000 – 40,000 ppm. The Pt band concentration in the LAB1 membranes was relatively close to that of the FOMs, indicating a realistic amount of PITM. The integrated PITM generating protocol used in LAB2-4 is however believed to better represent the situation in the field, since Pt gradually migrates from the cathode into the membrane during field operation (unlike LAB1). LAB2 membranes accumulated significantly more PITM than LAB1, which was reflected in a much longer AMDT lifetime. LAB3 and LAB4 were used to generate PITM concentrations closer to the FOMs by reducing the frequency of the PITM generating cycles during the AMDT operation. However, the LAB3 membranes still contained substantially more Pt than the FOMs, while the LAB4 membranes contained less Pt at the inlet and more Pt at the outlet compared to the FOMs. As mentioned previously, there was a positive effect on membrane stability in LAB3, while LAB4 had a negative effect. Consequently, although the Pt band was generally favorable for membrane stability, there was no direct correlation between PITM concentration and membrane

lifetime. Furthermore, it is noteworthy that LAB1 had a lower PITM concentration than LAB4 but still achieved a 40% increase in lifetime, presumably due to the pre-AMDT application of the Pt band.

### **3.1. Pt particle shapes**

The Pt particle structure may also contribute to the membrane stability effects associated with PITM. For this reason, the Pt particle shapes across the thickness of the membrane were analyzed by TEM, focusing on the membrane region close to the MEA outlet which had the highest Pt concentration. Figure 3 shows typical images of Pt particles identified in the FOMs from the areas close to the anode, middle, and near the cathode where the Pt band was located. The 2,800 h FOMs (Figure 3a-c) contained a mix of spherical, cubic, and triangular particles with smooth surfaces throughout the membrane. In addition, curly dendritic particles were present close to the cathode, at the location of the Pt band. Smooth tetrahedral and cubic particles populated the middle of the 4,400 h FOMs along with tripod and star shaped particles (Figure 3e). The curly dendritic particles close to the cathode grew in size over time, likely due to agglomeration of smaller particles, while small cubic particles occupied the narrow space between the cathode and the Pt band (Figure 3f). A distinct transition to star shaped particles was observed in the middle of the 8,200 h FOMs (Figure 3h). Close to the cathode (Figure 3i), growth of curly dendritic particles was observed across the entire space, with no sign of cubic particles. The area near the anode was sparsely populated with seed particles, i.e., smooth tiny spherical or cubic particles, with no significant changes over time.

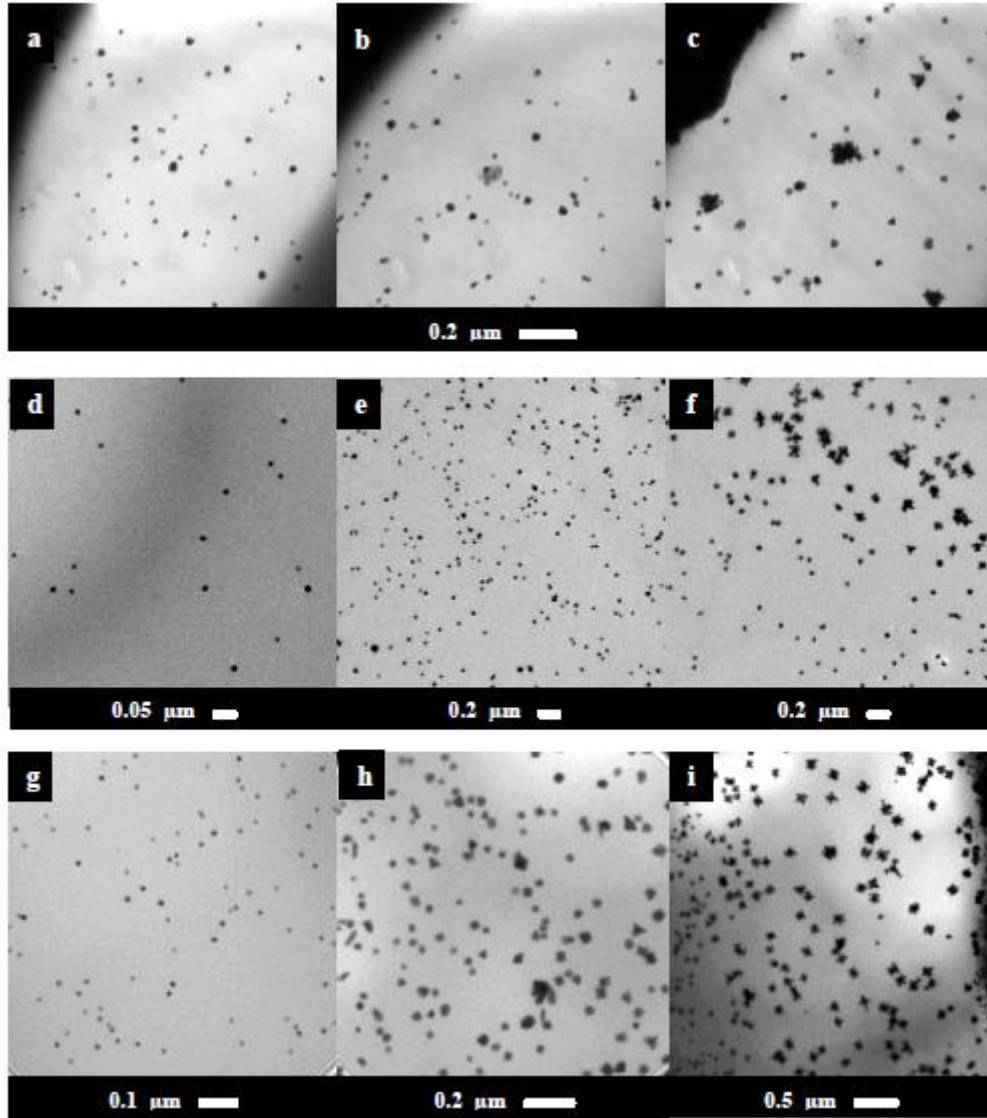


Figure 3. PITM from anode (left) to cathode (right) in field operated membranes at a-c) 2,800 h, d-f) 4,400 h, and g-i) 8,200 h.

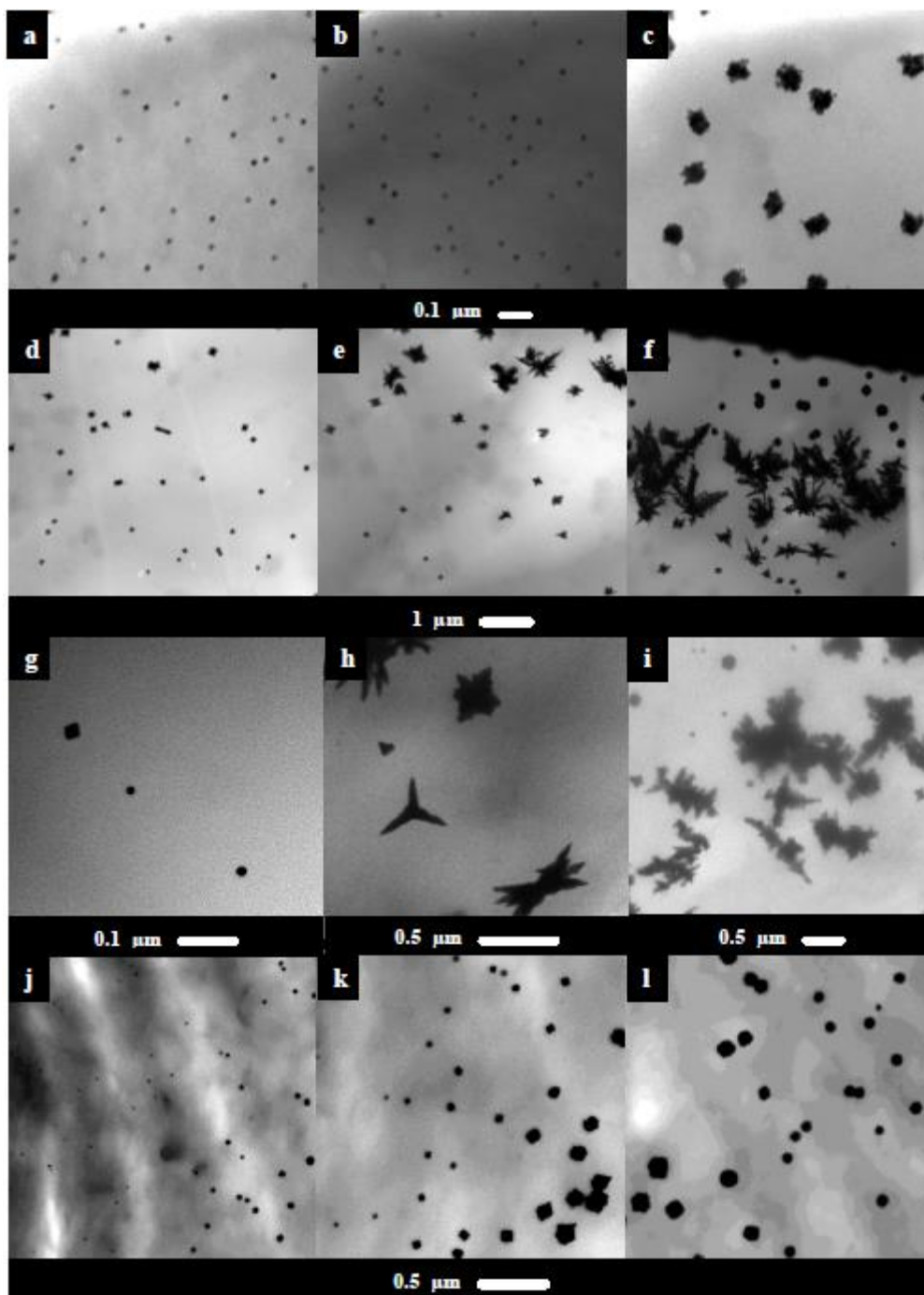


Figure 4. PITM from anode (left) to cathode (right) in AMDT operated membranes with laboratory generated PITM: a-c) LAB1; d-f) LAB2; g-i) LAB3; and j-l) LAB4.

Figure 4 shows the Pt particle distribution in the AMDT operated membranes (LAB1-4) with laboratory generated PITM. Similar to the FOMs, the anode region contained unremarkable small spherical or cubic particles in all cases. A combination of smooth cubic, tetrahedral, star, and diamond shaped particles appeared in the middle of the LAB1 membranes (Figure 4b), while curly dendritic particles were observed close to the cathode (Figure 4c), similar to those identified in the FOMs. These particles are a confirmation of successful laboratory replication of the field generated PITM distribution and particle shapes, in particular at the critical location of the Pt band. Due to the high amount of PITM, the particles in LAB2 formed more complex shapes at the Pt band (Figure 4f) compared to LAB1. Star shaped particles in the middle (Figure 4e) gradually transformed into large highly branched interconnected multi-armed particles with very sharp surfaces at the Pt band (Figure 4f), which may have been responsible for the longer lifetime of LAB2 compared to LAB1. Additionally, large smooth cubic particles occupied the space between the Pt band and the cathode. The middle of the LAB3 membranes contained tripod and star shaped particles (Figure 4h), and the Pt band was formed by interconnected dendritic particles with sharp surfaces (Figure 4i), similar to those in LAB2 albeit less complex, along with occasional smooth cubic particles. In stark contrast, LAB4 membranes (Figure 4j-l) were dominated by a single particle shape: cubic particles, gradually increasing in size from the middle to the cathode. LAB4 had somewhat lower AMDT lifetime than the baseline without PITM, suggesting that the cubic particles had no effect, or possibly a slightly negative effect, on the membrane lifetime. Some cubic particles close to the cathode were in initial stages of expansion, with tiny spikes forming in the corners. This indicates that the more complex particles observed in LAB2 and LAB3 were also initially cubic. In general, particle shape complexity increased from anode to cathode, and the Pt band region near the cathode featured a variety of

smooth, curly, and spiky dendritic particles in all cases except for LAB4. Furthermore, all membranes had spherical and cubic particles in common. The surface area of Pt nanoparticles is known to influence catalytic activity [62], i.e., rough surfaces have higher catalytic activity due to higher surface area and a higher number of kinks and edges exposed to reactions, which could be favorable for membrane stability. The roughest particle surfaces were observed on particles within the Pt band and close to the cathode.

### **3.2. Pt particle size distribution**

Since the Pt particles had various shapes, the average particle diameter was selected as the primary particle size metric. As shown in Figure 5, the average Pt particle size as well as the particle size variability gradually increased from anode to cathode, with a peak at the Pt band region. Most particles were below 200 nm in diameter except for the large dendritic particles observed at the band. The largest particles detected in the FOMs grew over time from ~90 nm at 2,800 h to ~180 nm at 4,400 h followed by a marginal growth to ~190 nm at 8,200 h. The particle sizes in the AMDT operated membranes were generally larger than those in the FOMs. However, the particle sizes of the LAB1 membranes were very similar to those of the FOMs, in agreement with the similar Pt concentration, particle shapes, and distribution previously noted, again confirming the realistic PITM features of LAB1. The high PITM concentration in LAB2 allowed for the formation of up to ~2  $\mu\text{m}$  interconnected multi-armed particles and ~350 nm cubic particles near the cathode. The highly branched particles in the Pt band of the LAB3 membranes exceeded 1  $\mu\text{m}$ , and the cubic particles typical to LAB4 membranes were up to ~350 nm in size. Small particles are known to have a high surface area and therefore high catalytic activity, while large dendritic particles may also attain high surface area due to their high surface roughness. In contrast, the large cubic particles of LAB4 would have relatively low surface area

per unit Pt.

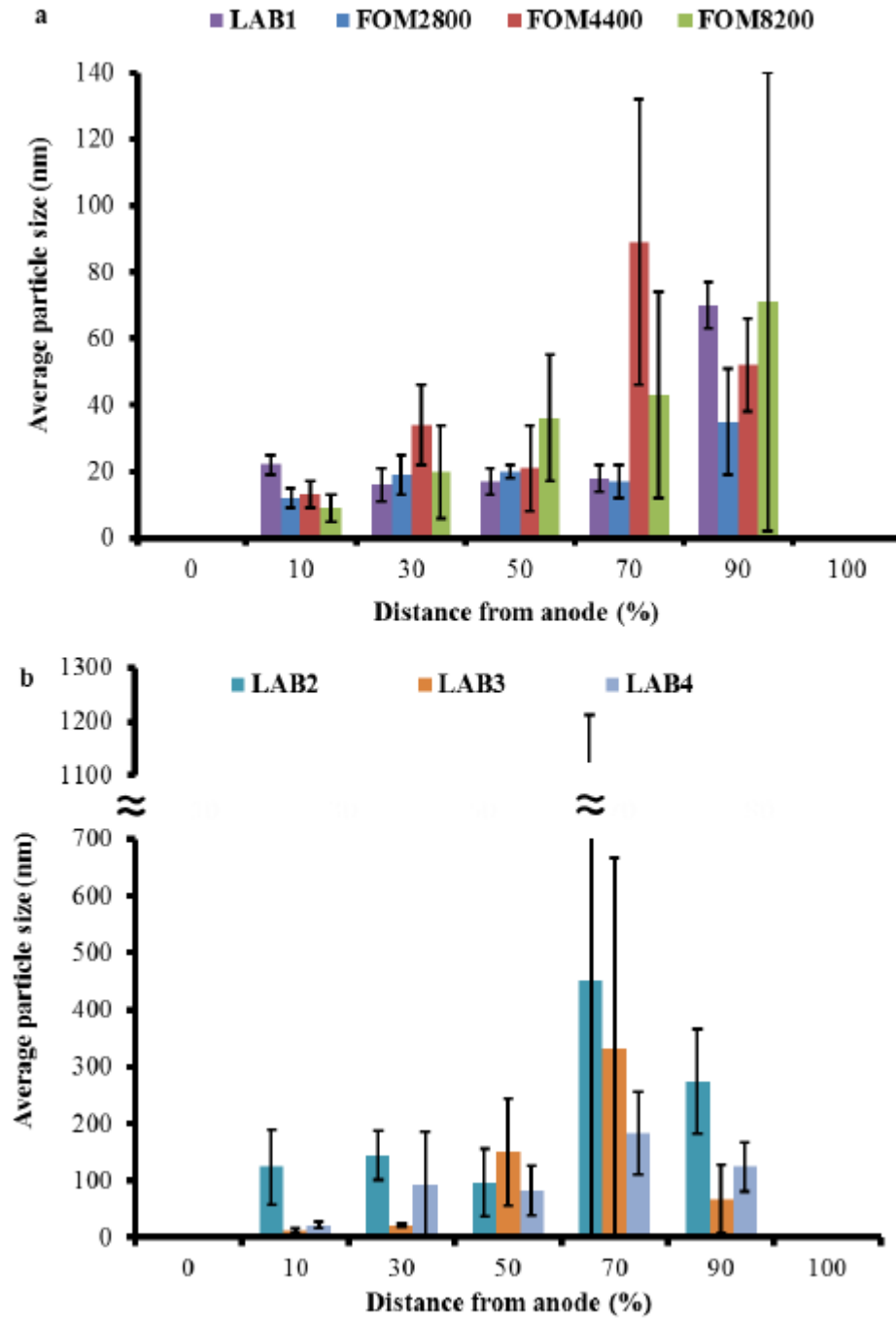


Figure 5. Pt particle size distribution across the membrane from anode to cathode in: a) LAB1, FOM2800, FOM4400, and FOM8200; and b) LAB2, LAB3, and LAB4.

### **3.3. Pt particle volumetric density and average inter-particle distance**

Figure 6 presents the Pt particle volumetric density at selected regions across the membrane from anode to cathode. The particle volumetric density is given as the number of Pt particles detected per  $\mu\text{m}^3$  of membrane volume; considering a membrane depth equal to the thickness of the ultra-microtomed membrane sections. In addition, the average inter-particle distance in the 2D view of the TEM images is shown in Figure 7. The seed particle density was generally higher in the anode and middle regions than in the cathode region of the membranes. Due to the appearance of large dendritic particles toward the cathode, the particle density tended to drop while the inter-particle distance increased, coinciding with the Pt band. The particle density decreased over time in the cathodic region of the FOMs due to a gradual change in particle population from a high number of small particles to a low number of large particles. Considering that the overall Pt concentration was relatively constant, this suggests that Pt particles were agglomerating over time. Moreover, a significant increase in particle density was observed in the anodic region after 8,200 h of field operation, indicating that Pt migrated deeper into the membrane over time. These particles were the closest packed group observed in this work.

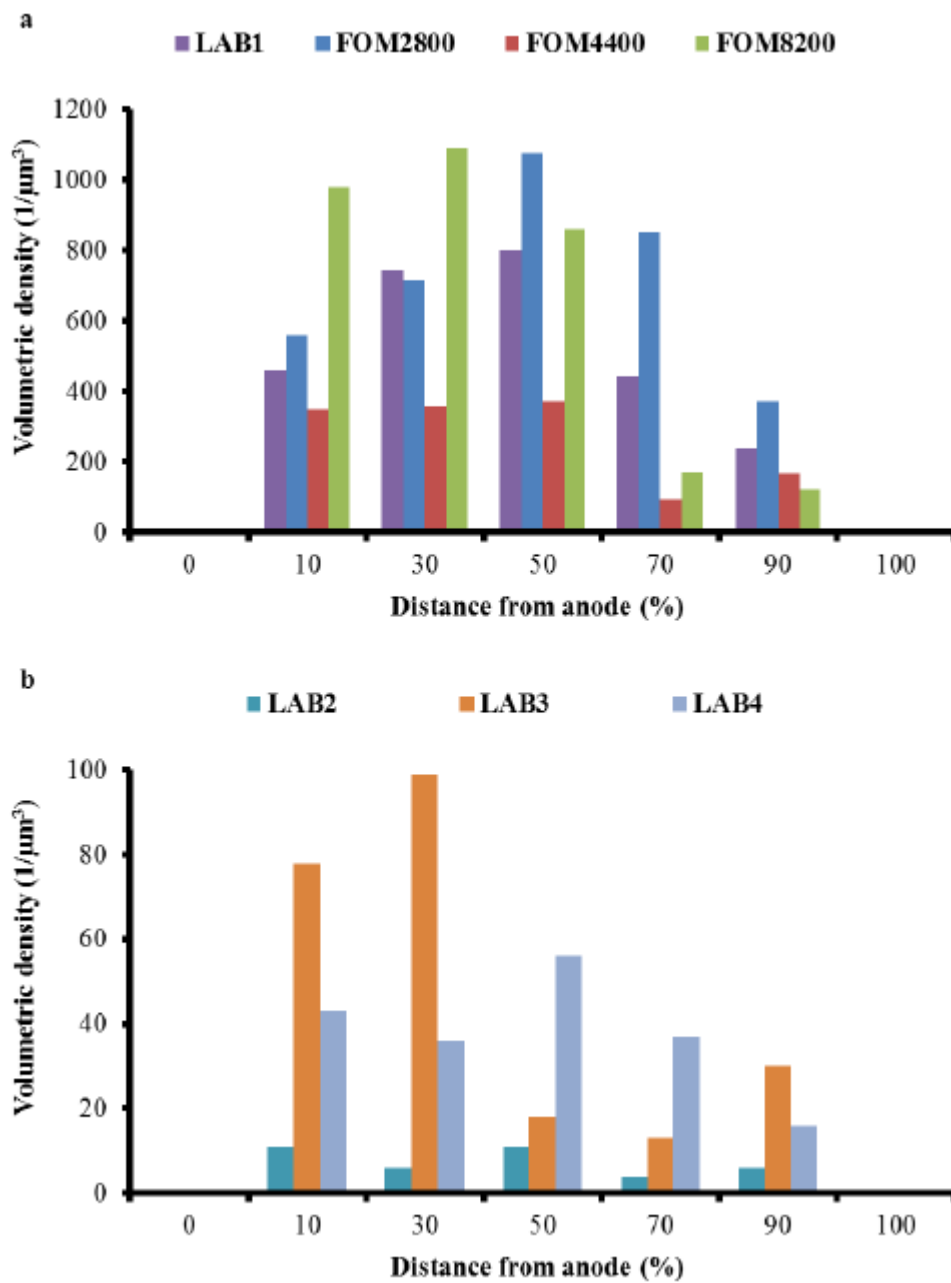


Figure 6. Volumetric density of Pt particles across the membrane from anode to cathode in: a) LAB1, FOM2800, FOM4400, and FOM8200; and b) LAB2, LAB3, and LAB4.

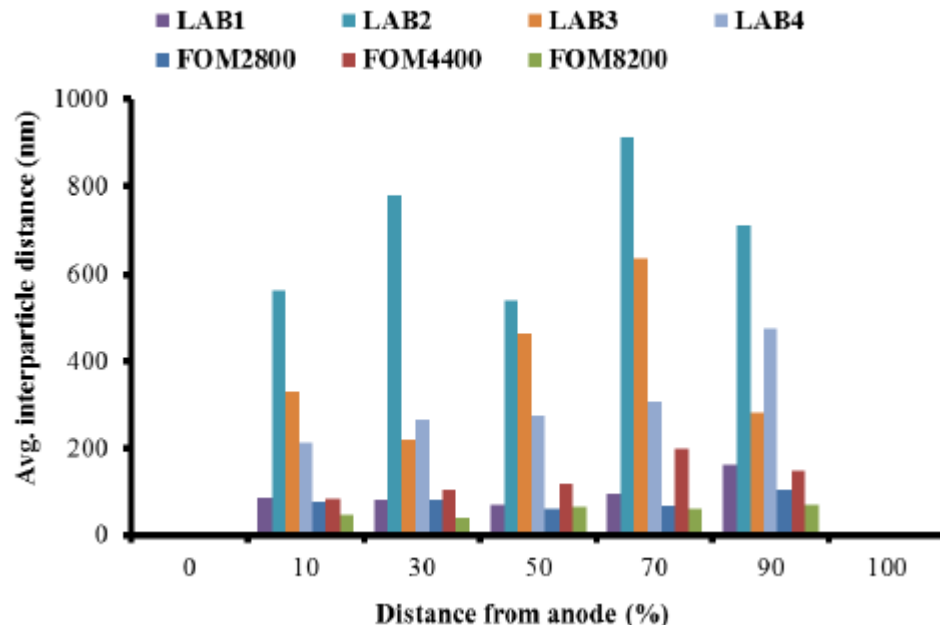


Figure 7. Average inter-particle distance in the AMDT (LAB1-4) and field operated membranes (FOM2800-8200).

The highest density of Pt particles in the AMDT operated membranes was generally found in the middle while the highest inter-particle distance was near the cathode. LAB1 had very similar volumetric density and inter-particle spacing to the FOMs, in agreement with the previously observed metrics. LAB2 exhibited the lowest volumetric density and highest inter-particle distance, which correlates to the high Pt concentration and large particle size compared to the other membranes. LAB3 and LAB4 also had much lower particle densities than LAB1 and the FOMs with higher inter-particle distances.

### 3.4. Lattice fringe analysis

The facets on the surface of the Pt particles can provide additional information about the affinity toward reactions that either mitigate or promote membrane degradation. In order to identify the crystal structure of the Pt particles in the membranes, the distance between certain

crystal planes, i.e.,  $d$ -spacings, was measured from fast Fourier transform (FFT) images obtained with high resolution TEM (HRTEM). Dendritic Pt particles, such as those observed in the FOMs and LAB1-3 membranes, are known to contain highly catalytically active (111) facets with typical  $d$ -spacings of 0.23 nm [63], which are therefore expected to facilitate reactive sites inside the membrane. Due to their abundance in the membranes, lattice fringes of star shaped and cubic particles were further analyzed. Figure 8a shows a 50 nm star shaped particle from the middle of the 4,400 h FOMs. Lattice fringes from the edge of the star are observed in Figure 8b. The FFT image from HRTEM shown in Figure 8c confirms single crystal nature. The FFT image was used to identify 0.2 nm and 0.25 nm  $d$ -spacings in two adjacent directions, which can be assigned to (200) and (110) facets, respectively. Similarly, lattice fringes in a 4 nm cubic particle (Figure 8d) located close to the anode in the 8,200 h FOMs were analyzed. A single crystal structure was also identified in this case based on the FFT image (Figure 8e) and the resulting  $d$ -spacings of 0.219 nm and 0.266 nm were assigned to (111) and (110) facets, respectively.

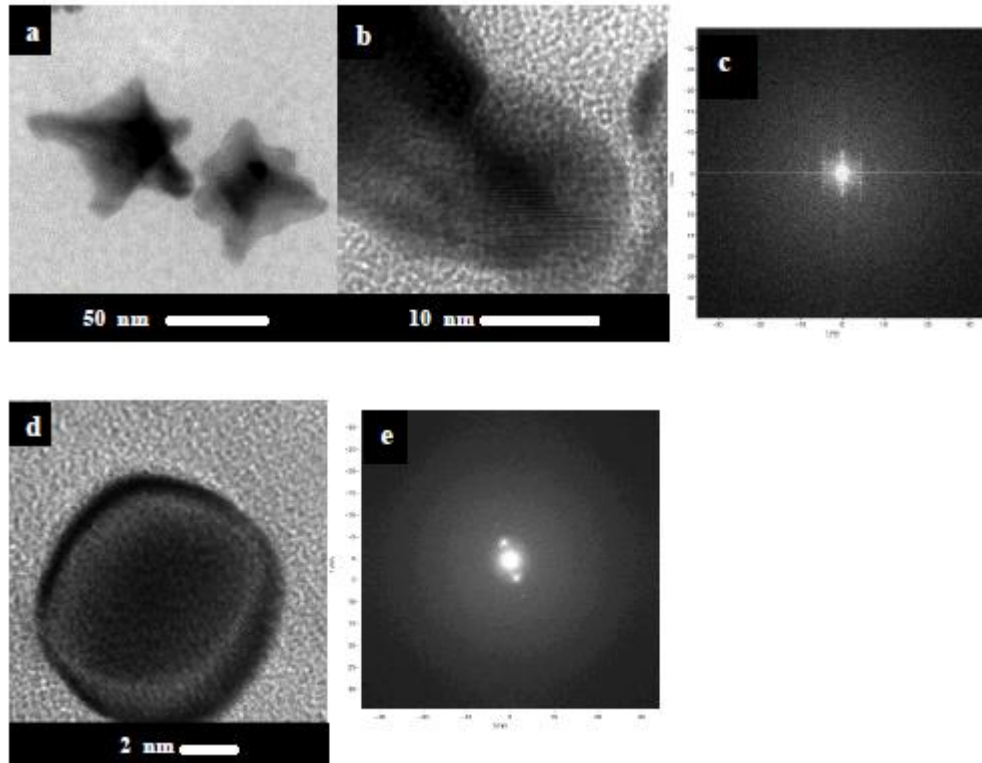


Figure 8. Lattice fringes on the edges of a-c) star shaped and d-e) cubic particles in the field operated membranes at 4,400 and 8,200 h, respectively.

### 3.5. Discussion

The hypothesis that PITM has a positive effect on membrane durability was first established when 2,800 h FOMs displayed enhanced membrane durability under highly aggressive accelerated stress test conditions due to the presence of a Pt band in the membrane [57]. For further investigation, membranes with four different PITM formulations (LAB1-4) were subjected to less aggressive AMDT conditions, which are more representative of field conditions [58]. LAB1, LAB2, and LAB3 surpassed the regular membrane durability, while LAB4, which had the lowest frequency of PITM generating cycles, did not. This led to the initial presumption that high PITM concentration leads to higher membrane durability under AMDT conditions.

However, the PITM concentrations of LAB1 and LAB4 were roughly the same despite a significant difference in AMDT lifetime, which indicates that other features of PITM may also be important. Most notably, all membranes in LAB1-3 contained large dendritic Pt particles at the critical location of the Pt band, while the membranes in LAB4 merely exhibited cubic particles.

The Pt particle shape is controlled by minimization of surface energy and interfacial kinetics of Pt reduction and subsequent Pt atomic incorporation onto different Pt surfaces. The equilibrium shape of a Pt crystal at zero temperature is a truncated octahedron consisting predominantly of (111) and (100) facets, which transforms into a truncated square cuboid shape in the presence of H<sub>2</sub> [64]. The formation of different faceted shapes is a result of the difference in partial pressure of H<sub>2</sub> adjacent to the Pt nuclei, which varies throughout the depth of the membrane. The smallest particles observed here were faceted spheres, triangles, cubes, and diamond-shaped structures. The transition from faceted to dendritic growth of Pt nanocrystals depends on the interfacial kinetics for reduction of Pt ions as well as the local concentrations of Pt ions and H<sub>2</sub> [65]. More complex star-shaped particles were generated in the region between the middle of the membrane and the Pt band. Multiarmed nanostars with single-crystal nanostructure are known to grow along (111) facets from tetrahedral particles [66] and exhibit improved electro-catalytic activity and stability due to favorable surface exposure for catalytic reactions [67]. The presence of Pt(111) was confirmed in a seed particle from the 8,200 h FOMs. Pt(110) was identified in both the star-shaped and cubic particles in the middle and close to the anode, respectively. Pt(110) has been reported to produce the lowest amount of peroxide and have the highest activity toward the oxygen reduction reaction (ORR) [68]. These are both positive findings for membrane stability, since the anodic region is otherwise favorable for hydrogen

peroxide formation. Furthermore, such particles can contribute to water production inside the membrane, leading to improved membrane hydration. The curly dendritic particles observed at the Pt band of all membranes except LAB4 have been reported to contain Pt(111) facets with high catalytic activity [63], which could provide effective sites for quenching of H<sub>2</sub>O<sub>2</sub> and crossover gases. Hence, due to the presence of curly dendritic Pt particles, the FOMs are expected to be more stable than LAB4 despite the lower PITM concentration. Such particles are expected to have higher surface area than the cubic particles in LAB4, which were ineffective in membrane lifetime extension. Cubic particles are likely an initial stage of the more mature tree-like structures, and are known to contain mainly Pt(100) facets with lower catalytic activity than Pt(111) [69]. Pt particles grown in regions with high Pt ion availability formed complex tree-like structures such as those in LAB2 and LAB3 membranes. Their rough surfaces, indicative of a high surface area, were effective in extending membrane life, presumably due to favorable kinetics for hydrogen peroxide quenching and gas crossover elimination.

In order to verify this theory, the rate of H<sub>2</sub>O<sub>2</sub> quenching into water and oxygen in the presence of PITM was estimated by numerical simulations. The average concentration of H<sub>2</sub>O<sub>2</sub> in the membrane under AMDT conditions was calculated using the method described in Wong et al. [70,71]. H<sub>2</sub>O<sub>2</sub> formation from crossover oxygen at the anode and from the ORR at the cathode was taken into account and the average H<sub>2</sub>O<sub>2</sub> concentration in the membrane was estimated to be 0.15 mol m<sup>-3</sup>. For simplicity, a Gaussian distribution was applied to the Pt particles in the membrane, where the Pt band thickness was used as the peak width. The variation in Pt band thickness from MEA inlet to outlet was measured by SEM and is shown in Table 1. The kinetics of H<sub>2</sub>O<sub>2</sub> quenching by Pt nanoparticles were estimated to be 0.0257 m<sup>3</sup> mol<sup>-1</sup> s<sup>-1</sup>, based on information provided by Shiraishi et al. [60]. The average quenching rate of the Pt particles in

LAB1 and LAB2 was then calculated based on the Pt concentration and the initial membrane H<sub>2</sub>O<sub>2</sub> concentration of 0.15 mol m<sup>-3</sup>. The source term used to calculate the H<sub>2</sub>O<sub>2</sub> quenching rate was:

$$r_{H_2O_2 \text{ quench}} = k c_{Pt} c_{H_2O_2} \quad (1)$$

where  $k$  represents the kinetics,  $c_{Pt}$  is the Pt concentration in the band, and  $c_{H_2O_2}$  is the hydrogen peroxide concentration. It is important to note that the quenching rate depends on both Pt band concentration and thickness. The average amount of residual H<sub>2</sub>O<sub>2</sub> is shown in Table 2, whereby it is estimated that 74 – 85% and 93 – 97% of H<sub>2</sub>O<sub>2</sub> can potentially be quenched in LAB1 and LAB2, respectively, which is in good agreement with the corresponding durability enhancements. Due to the similarities of the Pt particles between LAB1 and the FOMs, similar results can be expected during field operation. The amount of radicals formed on the Pt particles was however not considered in this calculation, but it is assumed that for all membranes with enhanced durability (LAB1-3 and FOMs), peroxide quenching is more prevalent than radical formation on the PITM. Reduction of the H<sub>2</sub>O<sub>2</sub> formation rate at the anode could also be achieved by reducing oxygen crossover to water at Pt particles in the membrane [72], and given the location of the Pt band at the intersection of the H<sub>2</sub> and O<sub>2</sub> fluxes, the large interconnected particles in the Pt band are likely to form a considerable barrier for crossover gases compared to the more dispersed, small cubic particles. Quenching of hydrogen peroxide and the reduction of crossover gases are therefore the principal mechanisms attributed to enhanced membrane stability. In conclusion, not only the PITM concentration, but the presence of PITM with the right shape and facet, i.e. large Pt(111) faceted dendritic particles at the Pt band location, is relevant to enhancement of membrane stability. The AMDT results for LAB1 indicate that a ~50% lifetime improvement is possible based on the PITM levels observed in field operated membranes.

#### **4. Conclusions**

Pt particle shapes, sizes, and distribution in the membrane was analyzed in field and laboratory operated membranes and the findings were correlated to membrane lifetime. Since the total PITM concentration in the field operated membranes was relatively constant over time, smaller particles were observed to gradually agglomerate to form larger particles. The Pt particle structure observed in these membranes was successfully reproduced in the laboratory, and enhanced durability of membranes with curly dendritic particles at the Pt band location was confirmed under AMDT conditions. Laboratory operated membranes with large interconnected tree-like structures, curly dendritic, and star-shaped particles also displayed enhanced durability due to high Pt (111) content and high surface area, leading to high catalytic activity toward peroxide quenching and crossover gas consumption. On the other hand, small cubic particles had no apparent durability enhancing effect. In the former case, it was estimated that 74 – 97% of H<sub>2</sub>O<sub>2</sub> can potentially be quenched in the presence of PITM. Such significant H<sub>2</sub>O<sub>2</sub> removal and the anticipated conversion of crossover gases into water are expected to result in mitigation of chemical membrane degradation during fuel cell operation. Thus, catalyst dissolution during field operation can have a positive impact on membrane durability due to the PITM formed.

#### **Acknowledgments**

Funding for this research was provided by Automotive Partnership Canada (APC) and the Natural Sciences and Engineering Research Council of Canada (NSERC). Materials and testing facilities were provided by Ballard Power Systems. The Holdcroft Group at SFU is acknowledged for the use of the ultra-microtome. We thank Mark Cruickshank, Curtis Allen, and Joanna Kolodziej for their contributions to testing and failure analysis. We also acknowledge 4D LABS for TEM usage and prompt technical support.

## References

- [1] U.S. DRIVE Partnership, Fuel Cell Technical Team Roadmap, 2013, [http://energy.gov/sites/prod/files/2014/02/f8/fctt\\_roadmap\\_june2013.pdf](http://energy.gov/sites/prod/files/2014/02/f8/fctt_roadmap_june2013.pdf).
- [2] U.S. DOE National Renewable Energy Laboratory, Fuel Cell Buses in U.S. Transit Fleets: Current Status 2012, [http://www.energy.gov/sites/prod/files/2014/03/f12/fceb\\_status\\_2012.pdf](http://www.energy.gov/sites/prod/files/2014/03/f12/fceb_status_2012.pdf).
- [3] L. Ghassemzadeh, K. Kreuer, *J. Phys. Chem. C* (2010) 14635–14645.
- [4] L. Ghassemzadeh, T.J. Peckham, T. Weissbach, X. Luo, S. Holdcroft, *J. Am. Chem. Soc.* 135 (2013) 15923–15932.
- [5] L. Ghassemzadeh, S. Holdcroft, *J. Am. Chem. Soc.* 135 (2013) 8181–8184.
- [6] A. Ohma, S. Yamamoto, K. Shinohara, *J. Power Sources* 182 (2008) 39–47.
- [7] A. Ohma, S. Suga, S. Yamamoto, K. Shinohara, *J. Electrochem. Soc.* 154 (2007) B757.
- [8] K.H. Wong, E. Kjeang, *ChemSusChem* 8 (2015) 1072–82.
- [9] R.M.H. Khorasany, E. Kjeang, G.G. Wang, R.K.N.D. Rajapakse, *J. Power Sources* 279 (2015) 55–63.
- [10] R.M.H. Khorasany, A. Sadeghi Alavijeh, E. Kjeang, G.G. Wang, R.K.N.D. Rajapakse, *J. Power Sources* 274 (2015) 1208–1216.
- [11] M.B. Satterfield, J.B. Benziger, *J. Polym. Sci. Part B Polym. Phys.* (2008) 11–24.
- [12] A. Sadeghi Alavijeh, M.-A. Goulet, R.M.H. Khorasany, J. Ghataurah, C. Lim, M. Lauritzen, E. Kjeang, G.G. Wang, R.K.N.D. Rajapakse, *Fuel Cells* 15 (2015) 204–213.
- [13] C. Lim, L. Ghassemzadeh, F. Van Hove, M. Lauritzen, J. Kolodziej, G.G. Wang, S. Holdcroft, E. Kjeang, *J. Power Sources* 257 (2014) 102–110.
- [14] U.S. Department of Energy Hydrogen Program, Enabling Commercial PEM Fuel Cells with Breakthrough Lifetime Improvements, 2004.
- [15] L. Gubler, W.H. Koppenol, *J. Electrochem. Soc.* 159 (2012) B211.
- [16] S. Xiao, H. Zhang, C. Bi, Y. Zhang, Y. Ma, X. Li, H. Zhong, Y. Zhang, *J. Power Sources* 195 (2010) 8000–8005.

- [17] C. Lim, A. Sadeghi Alavijeh, M. Lauritzen, J. Kolodziej, S. Knights, E. Kjeang, *ECS Electrochem. Lett.* 4 (2015) F29–F31.
- [18] M. Zaton, D. Jones, J. Roziere, *ECS Trans.* 61 (2014) 15–23.
- [19] J. Wu, X.Z. Yuan, J.J. Martin, H. Wang, J. Zhang, J. Shen, S. Wu, W. Merida, *J. Power Sources* 184 (2008) 104–119.
- [20] S. Subianto, M. Pica, M. Casciola, P. Cojocaru, L. Merlo, G. Hards, D.J. Jones, *J. Power Sources* 233 (2013) 216–230.
- [21] M.-A. Goulet, R.M.H. Khorasany, C. De Torres, M. Lauritzen, E. Kjeang, G.G. Wang, N. Rajapakse, *J. Power Sources* 234 (2013) 38–47.
- [22] M.-A. Goulet, S. Arbour, M. Lauritzen, E. Kjeang, *J. Power Sources* 274 (2015) 94–100.
- [23] K. Sasaki, M. Shao, R. Adzic, *Polymer Electrolyte Fuel Cell Durability*, Springer New York, New York, NY, 2009.
- [24] R.M. Darling, J.P. Meyers, *J. Electrochem. Soc.* 150 (2003) A1523.
- [25] K. Asano, Y. Mugikura, T. Watanabe, *ECS Trans.* 16 (2008) 779–785.
- [26] C.A. Reiser, L. Bregoli, T.W. Patterson, J.S. Yi, J.D. Yang, M.L. Perry, T.D. Jarvi, *Electrochem. Solid-State Lett.* 8 (2005) A273.
- [27] W. Gu, R.N. Carter, P.T. Yu, H. Gasteiger, *ECS Trans.* 11 (2007) 963–973.
- [28] S. Kreitmeier, A. Wokaun, F.N. Buchi, *J. Electrochem. Soc.* 159 (2012) F787–F793.
- [29] W. Bi, T.F. Fuller, *J. Electrochem. Soc.* 155 (2008) B215.
- [30] K. Sasaki, F. Takasaki, Z. Noda, S. Hayashi, Y. Shirator, K. Ito, *ECS Trans.* 33 (2010) 473–482.
- [31] J. Zhang, B. Litteer, W. Gu, H. Liu, H. Gasteiger, *J. Electrochem. Soc.* 154 (2007) B1006.
- [32] V. Atrazhev, S.F. Burlatsky, N.E. Cipollini, D.A. Condit, N. Erihman, *ECS Trans.* 1 (2006) 239–246.
- [33] S.F. Burlatsky, M. Gummalla, V. V. Atrazhev, D. V. Dmitriev, N.Y. Kuzminyh, N.S. Erihman, *J. Electrochem. Soc.* 158 (2011) B322.
- [34] S. Takaichi, H. Uchida, M. Watanabe, *Electrochem. Commun.* 9 (2007) 1975–1979.
- [35] L. Kim, C.G. Chung, Y.W. Sung, J.S. Chung, *ECS Trans.* 16 (2008) 945–953.

- [36] H. Hagihara, H. Uchida, M. Watanabe, *Electrochim. Acta* 51 (2006) 3979–3985.
- [37] M.J. Eslamibidgoli, P.-É.A. Melchy, M.H. Eikerling, *Phys. Chem. Chem. Phys.* (2015).
- [38] B. Zhang, D. Wang, Y. Hou, S. Yang, X.H. Yang, J.H. Zhong, J. Liu, H.F. Wang, P. Hu, H.J. Zhao, H.G. Yang, *Sci. Rep.* 3 (2013) 1836.
- [39] Z.Z. Lin, X. Chen, C. Yin, H. Tang, Y.C. Hu, X.J. Ning, *EPL (Europhysics Lett.* 96 (2011) 66005.
- [40] T.S. Ahmadi, Z.L. Wang, T.C. Green, A. Henglein, M.A. El-Sayed, *Science* (80-. ). 272 (1996) 1924–1926.
- [41] M. Aoki, H. Uchida, M. Watanabe, *Electrochem. Commun.* 8 (2006) 1509–1513.
- [42] Z. Liu, Y. Yang, W. Lü, C. Wang, M. Chen, Z. Mao, *Int. J. Hydrogen Energy* 37 (2012) 956–960.
- [43] M.P. Rodgers, B.P. Pearman, L.J. Bonville, D. Cullen, N. Mohajeri, D.K. Slattery, *J. Electrochem. Soc.* 160 (2013) F1123–F1128.
- [44] M.P. Rodgers, D.A. Cullen, J. Leonard, D.K. Slattery, J.M. Fenton, in: *Carisma 2012 – 3rd Carisma Int. Conf.*, 2012, pp. 1–19.
- [45] S. Helmly, R. Hiesgen, T. Morawietz, X.-Z. Yuan, H. Wang, K. Andreas Friedrich, *J. Electrochem. Soc.* 160 (2013) F687–F697.
- [46] M.P. Rodgers, L.J. Bonville, D.K. Slattery, *ECS Trans.* 41 (2011) 1461–1469.
- [47] S. Helmly, B. Ohnmacht, R. Hiesgen, E. Gülzow, K.A. Friedrich, *ECS Trans.* 58 (2013) 969–990.
- [48] M. Gummalla, V. V. Atrazhev, D. Condit, N. Cipollini, T. Madden, N.Y. Kuzminyh, D. Weiss, S.F. Burlatsky, *J. Electrochem. Soc.* 157 (2010) B1542.
- [49] D. Zhao, B.L. Yi, H.M. Zhang, M. Liu, *J. Power Sources* 195 (2010) 4606–4612.
- [50] N. Ohguri, A.Y. Nosaka, Y. Nosaka, *J. Power Sources* 195 (2010) 4647–4652.
- [51] A. Clark, A. Zhu, K. Sun, H.R. Petty, *J. Nanopart. Res.* 13 (2011) 5547–5555.
- [52] T. Hamasaki, T. Kashiwagi, T. Imada, N. Nakamichi, S. Aramaki, K. Toh, S. Morisawa, H. Shimakoshi, Y. Hisaeda, S. Shirahata, *Langmuir* 24 (2008) 7354–7364.
- [53] H. Nakanishi, T. Hamasaki, T. Kinjo, K. Teruya, S. Kabayama, S. Shirahata, *BMC Proc.* 7 (2013) P41.

- [54] H. Okamoto, K. Horii, A. Fujisawa, Y. Yamamoto, *Exp. Dermatol.* 21 (2012) 5–7.
- [55] K. Hirakawa, S. Sano, *Bull. Chem. Soc. Jpn.* 82 (2009) 1299–1303.
- [56] S. Onizawa, K. Aoshiba, M. Kajita, Y. Miyamoto, A. Nagai, *Pulm. Pharmacol. Ther.* 22 (2009) 340–9.
- [57] N. Macauley, L. Ghassemzadeh, C. Lim, M. Watson, J. Kolodziej, M. Lauritzen, S. Holdcroft, E. Kjeang, *ECS Electrochem. Lett.* 2 (2013) F33–F35.
- [58] N. Macauley, A. Sadeghi Alavijeh, M. Watson, J. Kolodziej, S. Knights, G.G Wang, E. Kjeang, *J. Electrochem. Soc.* 162 (2015) F98–F107.
- [59] S. Onizawa, K. Aoshiba, M. Kajita, Y. Miyamoto, A. Nagai, *Pulm. Pharmacol. Ther.* 22 (2009) 340–349.
- [60] Y. Shiraishi, M. Hashimura, M. Nakao, T. Ishizu, M. Kazita, Y. Miyamoto, N. Toshima, *Supramol. Chem.* 23 (2011) 195–198.
- [61] A.P. Young, J. Stumper, S. Knights, E. Gyenge, *J. Electrochem. Soc.* 157 (2010) B425.
- [62] M. Nesselberger, S. Ashton, J.C. Meier, I. Katsounaros, K.J.J. Mayrhofer, M. Arenz, *J. Am. Chem. Soc.* 133 (2011) 17428–33.
- [63] L. Wang, Y. Yusuke, *J. Am. Chem. Soc.* 131 (2009) 9152–9153.
- [64] P.J. Ferreira, Y. Shao-Horn, *Electrochem. Solid-State Lett.* 10 (2007) B60.
- [65] E. Ben-Jacob, R. Godbey, N.D. Goldenfeld, J. Koplik, H. Levine, T. Mueller, L.M. Sander, *Phys. Rev. Lett.* 55 (1985) 1315–1318.
- [66] M.A. Mahmoud, C.E. Tabor, M.A. El-Sayed, Y. Ding, Z.L. Wang, *J. Am. Chem. Soc.* 130 (2008) 4590–4591.
- [67] D.-H. Kwak, Y.-W. Lee, K.-H. Lee, A.-R. Park, J.-S. Moon, K.-W. Park, *Int. J. Electrochem. Sci.* 8 (2013) 5102–5107.
- [68] N.M. Markovic, H.A. Gasteiger, P.N. Ross, *J. Phys. Chem.* 99 (1995) 3411–3415.
- [69] C.-Y. Chiu, Y. Li, L. Ruan, X. Ye, C.B. Murray, Y. Huang, *Nat. Chem.* 3 (2011) 393–9.
- [70] K.H. Wong, E. Kjeang, *J. Electrochem. Soc.* 161 (2014) F823–F832.
- [71] K.H. Wong, E. Kjeang, *ChemSusChem* In press (2015).

[72] H. Uchida, Y. Ueno, H. Hagihara, M. Watanabe, *J. Electrochem. Soc.* 150 (2003) A57–A62.

# Appendix D

## ANOVA Analysis

### *ANOVA Analysis of voltage, oxygen concentration, RH and temperature*

The effects of voltage, oxygen concentration, RH and temperature were evaluated with ANOVA analysis. Based on the p – value voltage has the most significant effect, followed by temperature, and oxygen concentration. The effect of RH was not significant. The summary of the analysis is shown in Table 1.

**Table 1. ANOVA analysis of voltage, oxygen concentration, RH and temperature**

<i>Regression Statistics</i>								
Multiple R	0.874261							
R Square	0.764333							
Adjusted R Square	0.685777							
Standard Error	179.3985							
Observations	17							
ANOVA								
	<i>df</i>	<i>SS</i>	<i>MS</i>	<i>F</i>	<i>Significance F</i>			
Regression	4	1252572	313143.1	9.729832	0.000957			
Residual	12	386205.8	32183.81					
Total	16	1638778						
	<i>Coefficients</i>	<i>Standard Error</i>	<i>t Stat</i>	<i>P-value</i>	<i>Lower 95%</i>	<i>Upper 95%</i>	<i>Lower 95.0%</i>	<i>Upper 95.0%</i>
Intercept	6609.192	1033.806	6.393065	<b>3.44E-05</b>	4356.721	8861.662	4356.721	8861.662
V	-3424.82	880.9702	-3.88756	<b>0.002158</b>	-5344.29	-1505.35	-5344.29	-1505.35
Oxygen	-7.69196	4.289834	-1.79307	<b>0.098185</b>	-17.0387	1.65479	-17.0387	1.65479
RH	3.661712	2.177391	1.681697	<b>0.118446</b>	-1.08241	8.405839	-1.08241	8.405839
T	-35.3987	11.15956	-3.17205	<b>0.008039</b>	-59.7133	-11.0841	-59.7133	-11.0841

The effects of voltage, oxygen concentration were evaluated once more without RH, yielding the same results for their significance, shown in Table 2.

**Table 2. ANOVA analysis of voltage and oxygen concentration.**

<i>Regression Statistics</i>								
Multiple R	0.841898							
R Square	0.708792							
Adjusted R Square	0.64159							
Standard Error	191.5975							
Observations	17							
ANOVA								
	<i>df</i>	<i>SS</i>	<i>MS</i>	<i>F</i>	<i>Significance F</i>			
Regression	3	1161553	387184.4	10.54722	0.000865			
Residual	13	477225	36709.62					
Total	16	1638778						
	<i>Coefficients</i>	<i>Standard Error</i>	<i>t Stat</i>	<i>P-value</i>	<i>Lower 95%</i>	<i>Upper 95%</i>	<i>Lower 95.0%</i>	<i>Upper 95.0%</i>
Intercept	6506.847	1102.19	5.90356	5.21E-05	4125.71	8887.984	4125.71	8887.984
V	-3253.63	934.5734	-3.4814	0.004056	-5272.65	-1234.6	-5272.65	-1234.6
Oxygen	-8.31793	4.564262	-1.82241	0.091469	-18.1784	1.542554	-18.1784	1.542554
T	-34.4212	11.90223	-2.89199	0.0126	-60.1344	-8.70798	-60.1344	-8.70798

***Voltage – Temperature interaction (evaluated at 45% O<sub>2</sub> & RH cycling)***

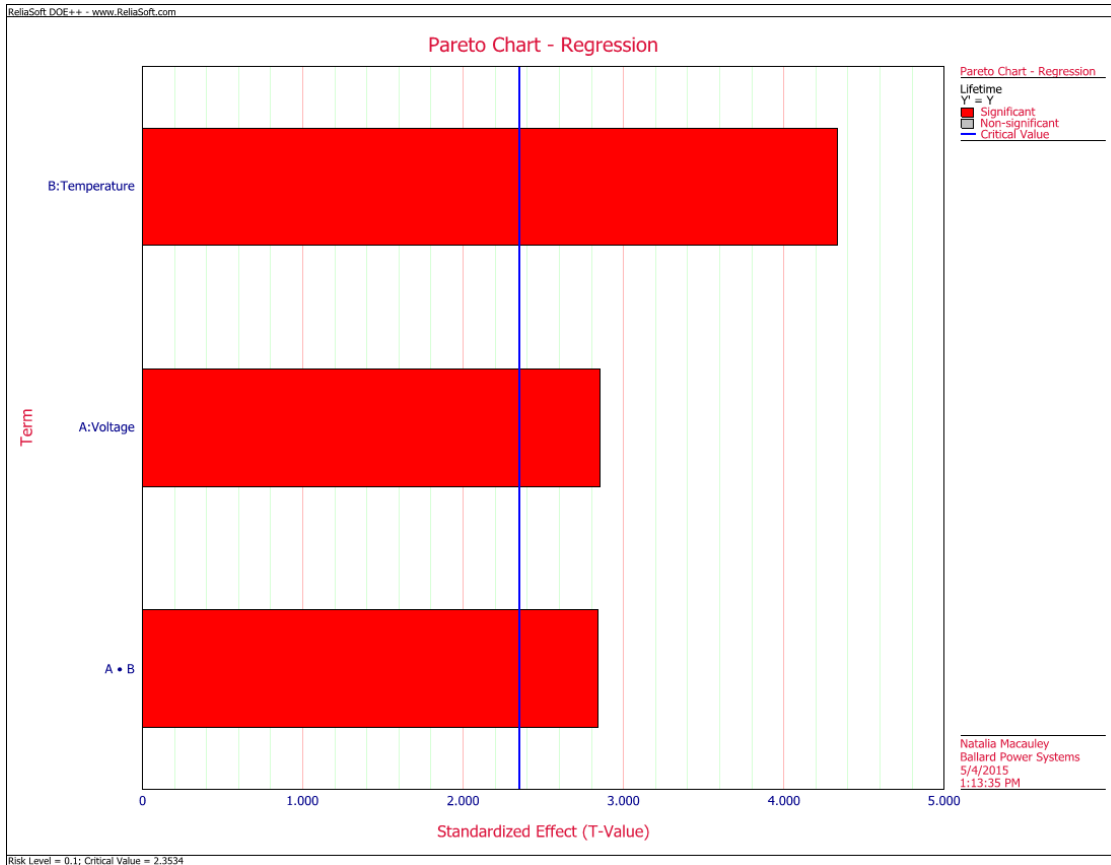
A full factorial Design of Experiment (DOE) was used to evaluate the effect of voltage and temperature at 3 levels. Missing tests were replaced with an asterisk. The ANOVA analysis and Pareto chart of residual show significance of both effects, and their interaction. The ANOVA analysis shows that temperature has a more significant effect on lifetime than voltage. The p-values are under 0.05 in the case of the two factors and their interaction.

**Table 3. Anova analysis of voltage and temperature.**

ANOVA Table					
Source of Variation	Degrees of Freedom	Sum of Squares [Partial]	Mean Squares [Partial]	F Ratio	P Value
Model	3	1.13E+06	3.77E+05	14.0656	0.0284
Main Effects	2	1.03E+06	5.13E+05	19.14	0.0196
2-Way Interactions	1	2.16E+05	2.16E+05	8.071	0.0656
Residual	3	8.04E+04	2.68E+04		
Lack of Fit	3	8.04E+04	2.68E+04		
Total	6	1.21E+06			

Regression Table						
Term	Coefficient	Standard Error	Low Confidence		T Value	P Value
			High Confidence	Low Confidence		
Intercept	500.1492	67.6346	340.9805	659.318	7.3949	0.0051
A:Voltage	-223.572	78.3591	-407.9795	-39.1645	-2.8532	0.0649
B:Temperature	-382.2446	88.1883	-589.7837	-174.7054	-4.3344	0.0227
A • B	284.8149	100.2534	48.8822	520.7477	2.8409	0.0656



**Figure 1. Pareto chart of T-V.**

*Temperature – Oxygen concentration interaction (evaluated at 0.9 V & RH cycling)*

Temperature and O<sub>2</sub>, and the T-O<sub>2</sub> interaction are significant factors. The effect of temperature is more significant than O<sub>2</sub>.

**Table 4. DOE of T – O<sub>2</sub>.**

Temperature (°C)	O <sub>2</sub> (%)	Lifetime (h)
85	45	277
90	45	175
75	45	478
90	21	341
75	21	*
85	21	410

**Table 5. Anova analysis of temperature and oxygen concentration.**

ANOVA Table						
Source of Variation	Degrees of Freedom	Sum of Squares [Partial]	Mean Squares [Partial]	F Ratio	P Value	
Model	3	5.51E+04	1.84E+04	2.86E+04	0.0044	
Main Effects	2	1.40E+04	7018.723	1.09E+04	0.0068	
2-Way Interactions	1	460.3894	460.3894	716.1613	0.0238	
Residual	1	0.6429	0.6429			
Lack of Fit	1	0.6429	0.6429			
Total	4	5.51E+04				
Regression Information						
Term	Coefficient	Standard Error	Low Confidence	High Confidence	T Value	P Value
Intercept	385.6607	0.6755	381.3957	389.9257	570.9178	0.0011
T:Factor 2	-127.446	0.8948	-133.096	-121.797	-142.427	0.0045
O <sub>2</sub> :Factor 3	58.8393	0.6755	54.5743	63.1043	87.1035	0.0073
T • O <sub>2</sub>	23.9464	0.8948	18.2968	29.5961	26.7612	0.0238

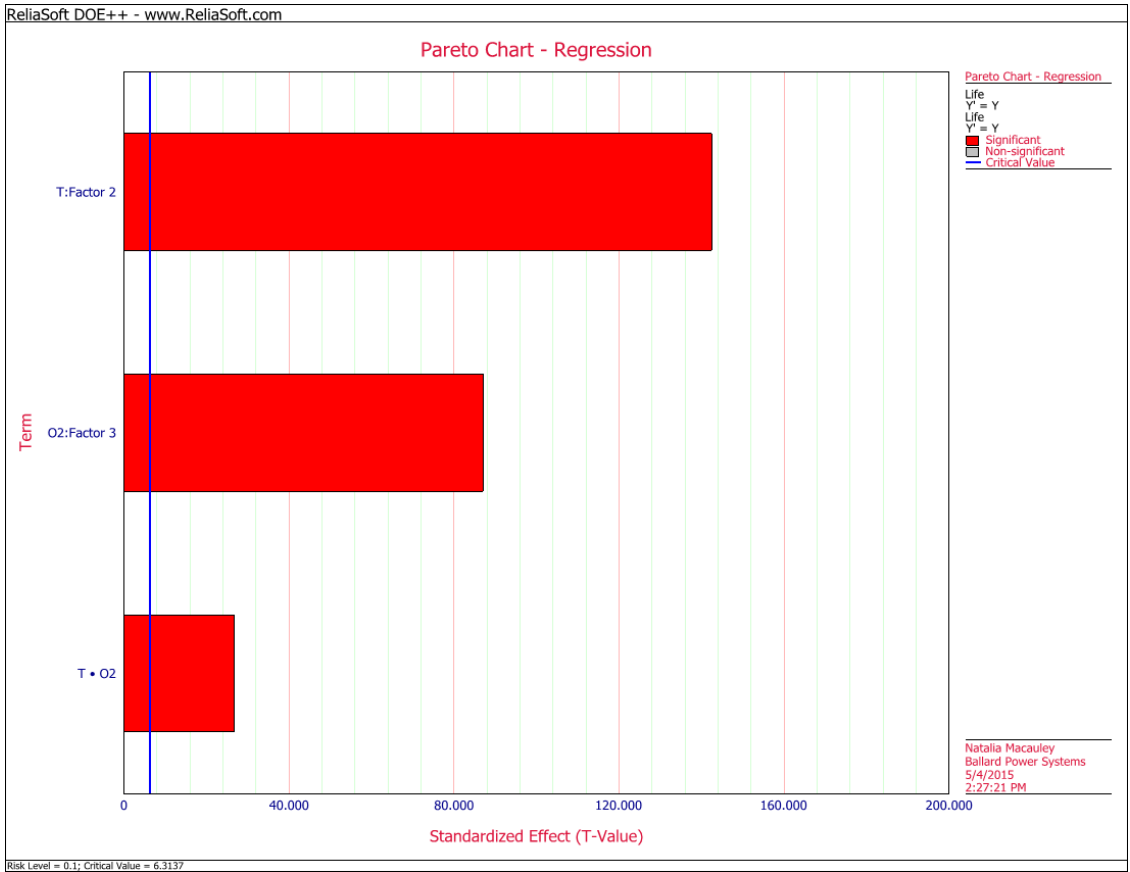


Figure 2. Pareto chart of T-O<sub>2</sub>.

*Voltage - Oxygen concentration @ 85 °C & RH cycling*

There is not sufficient data to evaluate the exact interaction effects of V-O<sub>2</sub>, but their main effects are compared in Figure 3.

Table 6. DOE of V - O<sub>2</sub>.

V (V)	O <sub>2</sub> (%)	Lifetime (h)
0.75	21	*
0.75	45	525
0.9	21	410
0.9	45	277

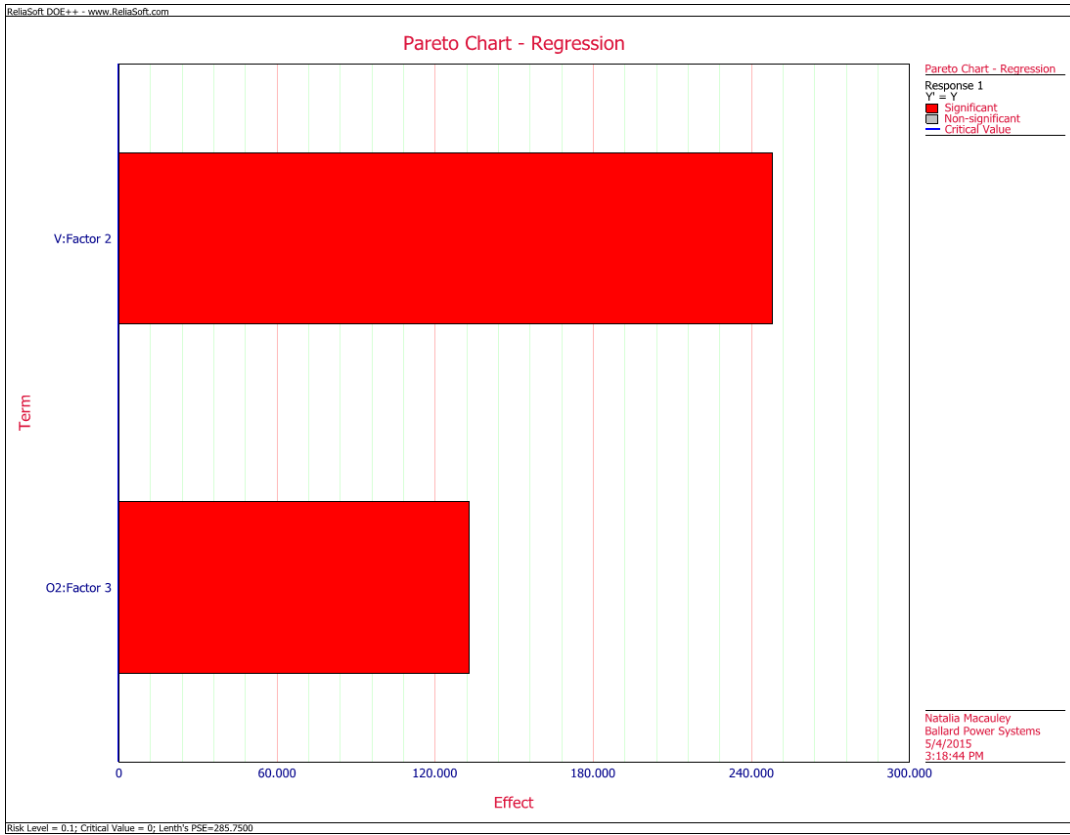


**Figure 3. Pareto chart of V-O.**